Distributed Control and Advanced Modulation of Cascaded Photovoltaic-Battery Converter Systems

Pan, Yiwei

DOI (link to publication from Publisher):
10.54337/aau470863170

Publication date:
2022

Document Version
Publisher's PDF, also known as Version of record

DISTRIBUTED CONTROL AND ADVANCED MODULATION OF CASCADED PHOTOVOLTAIC-BATTERY CONVERTER SYSTEM

BY
YIWEI PAN

DISSERTATION SUBMITTED 2022

AALBORG UNIVERSITY
DENMARK

Distributed Control and Advanced Modulation of Cascaded Photovoltaic-Battery Converter Systems

Ph.D. Dissertation

Yiwei Pan

AALBORG UNIVERSITY
DENMARK

Dissertation submitted March, 2022

Dissertation submitted: March 2022

PhD supervisor: Prof. Frede Blaabjerg,
Aalborg University, Denmark

Assistant PhD supervisors: Prof. Yongheng Yang,
Zhejiang University, China

Assistant Prof. Ariya Sangwongwanich,
Aalborg University, Denmark

PhD committee: Associate Professor Szymon Michal Beczkowski
Aalborg University, Denmark

Associate Professor Sergio Vazquez
University of Sevilla, Spain

Prof. Juan Carlos Balda,
University of Arkansas, USA

PhD Series: Faculty of Engineering and Science, Aalborg University

Department: AAU Energy

ISSN (online): 2446-1636
ISBN (online): 978-87-7573-935-6

Published by:
Aalborg University Press
Kroghstræde 3
DK – 9220 Aalborg Ø
Phone: +45 99407140
aauf@forlag.aau.dk
forlag.aau.dk

Printed in Denmark by Rosendahls, 2022

Abstract

With the still growing installation of photovoltaic (PV) systems, energy storage (ES) elements such as batteries are increasingly integrated with PV panels to meet the grid requirements. To simplify the system structure, reduce cost, and improve efficiency, single-stage series configurations like cascaded H-bridge (CHB) converters are attractive for integrating distributed PV and battery units. However, issues related to the pulse-width modulation (PWM), distributed power control, and coordination among individual units remain in series configurations, limiting their application in PV-battery systems. This Ph.D. project was proposed to properly address these issues.

Firstly, in order to suppress high-frequency (HF) harmonics, the PWM carriers of series converters should be synchronized and properly phase-shifted according to the output voltages of individual converters. However, as conventional variable-angle phase-shifting (VAPS) PWM methods are based on mathematical searching algorithms, the optimal carrier phase-shifting (PS) angles cannot be timely updated due to a high computational burden, which requires hundreds of milliseconds to obtain the results. During the period when the optimal angles are not calculated, the total harmonic distortion (THD) of the total voltage may grow significantly, leading to a higher risk of electric magnetic interference (EMI) issues.

Secondly, if the individual converters are not properly coordinated, challenging issues may appear in series-PV-battery systems, e.g., by degrading power quality, stability, and grid-interaction performances (e.g., overloading the grid during the peak power generation of PV systems). For instance, as a power quality issue, interharmonics can be significantly amplified when PV converters are connected in series, which is due to the in-phase maximum power point tracking (MPPT) perturbation of individual converters. On the other hand, to achieve a schedulable power flow, the total power of the series system should be flexibly controlled according to grid commands. In this case, if individual converters are not properly coordinatively controlled, 1) certain converters may be overloaded or overmodulated, and 2) the total power scheduling constraints cannot be maintained in certain conditions. Both can result in performance degradation, or even system instability.

Moreover, conventional distributed/decentralized control methods for series-converter systems are either highly dependent on real-time communication or only applicable for systems with limited operating conditions, e.g., when the power factors (PFs) of individual converters are identical. In other words, prior-art solutions are neither cost-effective nor suitable for series-PV-battery systems, where individual converters can operate at any PFs with low communication requirements.

Accordingly, solutions have been developed in this project for series systems in terms of modulation, interharmonic mitigation, distributed control, and flexible active power control (FAPC). In order to improve the response of the VAPS PWM method, a hardware approach for the VAPS PWM method has been developed, where the

optimization is accelerated by the parallel computing using field programmable gate arrays (FPGAs). With this approach, the optimization speed of the mathematical searching algorithm can be accelerated significantly.

To address the interharmonic issue, a phase-shifting MPPT (PS-MPPT) method has been proposed, which shifts the phase-angle of the DC voltage oscillations caused by the MPPT in a way to counteract with each other. By doing so, interharmonics from the series converters can be suppressed to a large extent. A random sampling-rate MPPT method for CHB PV converters has also been studied. Subsequently, a hybrid PS-MPPT combing PS-MPPT and the random sampling-rate MPPT, and a hardware-based method called "interharmonic filter", have been developed in this project. The hybrid PS-MPPT method can improve the interharmonic mitigation performance, while the "interharmonic filter" is an additional series converter with only capacitors in its DC side, to cancel the total DC voltage oscillations of all PV converters, and thereby interharmonics.

A distributed control scheme for series-PV-battery systems has also been proposed in this project, which includes the active and reactive power (*PQ*) decoupling control of individual converters, droop control for a battery converter, reactive power distribution strategies, and anti-over-modulation (AOM) control for all converters. With the proposed control, each converter can be self-synchronized with the entire system regardless of its operating PF, while the difference between the PV power generation and the load demand can be compensated by the battery converter, enabling the participation of the entire system in grid frequency and voltage regulation. The total reactive power is distributed among all converters in a way to balance their loading condition, and the AOM control is achieved by the coordinated power curtailment control of PV converters, reducing the overloading and overmodulation risks for each converter.

Based on the distributed control, flexible active power control strategies including the power ramp-rate control (PRRC), power limiting control (PLC), and power reserve control (PRC) strategies have been developed for grid-connected series-PV-battery systems. With the active power control strategies, all converters are coordinated considering 1) the battery power and state of charge (SoC) limits, 2) the available power of each PV converter, 3) the total power ramp-rate/limiting/reserve constraints, and 4) the available power estimation command for each PV converter. By doing so, the total power of series-PV-battery systems can be maintained following the ramp-rate/limiting/reserve constraints from the grid scheduling control, while the curtailed/reserved power is properly distributed among all converters to ensure the stable operation, PV power yield, load balancing of individual converters, and the available power estimation of individual PV converters for the PRC.

To summarize, in this Ph.D. project, efforts have been made to improve the THD performance, mitigate interharmonics, reduce the communication dependency, and achieve FAPC functions for series-PV-battery systems. Correspondingly, a computation-efficient VAPS PWM method, modified MPPT methods, a distributed power control scheme with low communication requirement, and flexible power control strategies have been proposed, providing solutions to integrate PV panels and

batteries into distribution systems using series configurations with improved output voltage / current performance, reduced cost, and enhanced power control flexibilities. The documented thesis is “Distributed Control and Advanced Modulation of Cascaded Photovoltaic-Battery Converter Systems”.

Dansk Resumé

Med den stadig voksende installation af fotovoltaiske (PV) systemer bliver energilagringselementer (ES) såsom batterier i stigende grad integreret med PV-paneler for at opfylde netkravene. For at forenkle systemstrukturen, reducere omkostningerne og forbedre effektiviteten er enkelt-trins seriekonfigurationer som cascaded H-bridge (CHB)-konvertere attraktive til at integrere distribuerede PV- og batterienheder. Imidlertid forbliver der problemer relateret til pulsbreddemodulation, distribueret effektstyring og koordinering mellem individuelle enheder i seriekonfigurationer, hvilket begrænser deres anvendelse i PV-batterisystemer. Dette ph.d. projekt vil addressere disse problemer.

For det første, for at undertrykke højfrekvente (HF) harmoniske, bør pulsbreddemodulationsbærerne (PWM) for seriekonverterne synkroniseres og korrekt fase-forskydes i henhold til udgangsspændingerne fra de individuelle omformere. Men da konventionelle PWM-metoder med variabel vinkel faseforskydning (VAPS) er baseret på matematiske søgealgoritmer, kan de optimale bærebølgefaseforskydningsvinkler (PS) ikke opdateres rettidigt på grund af dens høje beregningsbyrde, som kræver hundredvis millisekunder for at opnå resultaterne. I den periode, hvor de optimale vinkler ikke beregnes, kan den totale harmoniske forvrængning (THD) af den samlede spænding vokse betydeligt, hvilket fører til en højere risiko for problemer med elektrisk magnetisk interferens (EMI).

For det andet, hvis individuelle konvertere ikke er korrekt koordinerede, kan der opstå udfordrende problemer i serie-PV-batterisystemer, forringende strømkvalitet, stabilitet og net-interaktionsydelser (f.eks. overbelastning af nettet under spidsstrøm-produktionen af PV-systemer). For eksempel, kan et problem med strømkvaliteten, forstærke interharmoniske frekvenser betydeligt, når PV-omformere er serieforbundet, hvilket skyldes den i-fase maksimale effektpunktsporing (MPPT) forstyrrelse af individuelle konvertere. Derimod bør seriesystemets samlede effekt styres fleksibelt i henhold til netkommandoer for at opnå et skemalagt strømflow. I dette tilfælde, hvis individuelle konvertere ikke er korrekt koordineret styret, 1) kan visse konvertere blive overbelastet eller overmoduleret, og 2) de samlede effektplanlægningsbegrænsninger kan ikke opretholdes under visse forhold. Begge kan resultere i ydeevneforringelse eller endda systemustabilitet.

Desuden er konventionelle distribuerede/decentraliserede styringsmetoder til seriekonverterede systemer enten stærkt afhængige af realtidskommunikation eller kun anvendelige for systemer med begrænsede driftsbetingelser, f.eks. når effektfaktorerne (PF'er) for individuelle konvertere er identiske. Med andre ord er de kendte løsninger hverken omkostningseffektive eller egnede til serie-PV-batterisystemer, hvor individuelle omformere kan fungere på alle PF'er med lave kommunikationskrav.

Derfor er der i dette projekt udviklet løsninger til seriesystemer i form af modulering, interharmonisk reduktion, distribueret kontrol og fleksibel aktiv effektstyring (FAPC). For at forbedre responsen af VAPS PWM-metoden er der udviklet en hardwaretilgang til VAPS PWM-metoden, hvor optimeringen accelereres af den parallelle beregning ved hjælp af feltprogrammerbare gate-arrays (FPGA'er). Med denne tilgang kan optimeringshastigheden af den matematiske søgealgoritme accelereres betydeligt.

For at løse det interharmoniske problem er der blevet foreslået en PS-MPPT-metode, som forskyder fasevinklen af DC-spændingsoscillationerne forårsaget af MPPT'en på en måde, der modvirker hinanden. Ved at gøre det kan de interharmoniske fra seriekonverterne i vid udstrækning undertrykkes. En tilfældig prøvetagningshastighed MPPT-metode for CHB PV-konvertere er også blevet undersøgt. Efterfølgende er der i dette projekt udviklet en hybrid PS-MPPT, der kombinerer PS-MPPT og den tilfældige sampling-rate MPPT, og en hardwarebaseret metode kaldet "interharmonisk filter". Hybrid PS-MPPT-metoden kan forbedre den interharmoniske dæmpningsydeevne, mens det "interharmoniske filter" er en ekstra seriekonverter kun bestående af kondensatorer på DC-siden, for at annullere de samlede DC-spændingsoscillationer for alle PV-konvertere og dermed også de interharmoniske.

En distribueret kontrolordning for serie-PV-batterisystemer er blevet foreslået i dette projekt, som inkluderer aktiv og reaktiv effekt (PQ) afkoblingskontrol af individuelle omformere, droop kontrol for en batterikonverter, reaktiv effektfordelingsstrategier, og anti-over-modulation (AOM) kontrol for alle konvertere. Med den foreslåede styring kan hver konverter selvsynkroniseres med hele systemet uanset dets drifts-PF, mens forskellen mellem PV-strømproduktionen og belastningsbehovet kan kompenseres af batterikonverteren, hvilket muliggør deltagelse af hele systemet i netfrekvens- og spændingsregulering. Den samlede reaktive effekt er fordelt mellem alle omformere på en måde, der balancerer deres belastningstilstand, og AOM-kontrollen opnås ved den koordinerede effektbegrænsningskontrol af PV-konvertere, hvilket reducerer overbelastnings- og overmodulationsrisikoen for hver omformer.

Baseret på den distribuerede styring er der udviklet fleksible aktiv effektstyringsstrategier, herunder kontrol af effektrampehastighed (PRRC), effektbegrænsende kontrol (PLC) og strømreserve kontrol (PRC) strategier til nettilsluttede serie-PV-batterisystemer. Med de aktive strømstyringsstrategier er alle omformere koordineret under hensyntagen til 1) batteristrøm og ladningstilstand (SoC) grænser, 2) den tilgængelige effekt for hver PV-konverter, 3) den samlede effektrampehastighed/begrænsning/reserve-begrænsninger, og 4) den tilgængelige effektestimerings kommando for hver PV-konverter. Ved at gøre det kan den samlede effekt af serie-PV-batterisystemer opretholdes ved at følge rampehastighed/begrænsning/reserve-begrænsningerne fra netplanlægningskontrollen, mens den begrænsede/reserverede effekt er korrekt fordelt mellem alle omformere for at sikre stabil drift, PV-effektudbytte, belastningsbalancering af individuelle konvertere og den tilgængelige effektestimering af individuelle PV-omformere for PRC.

For at opsummere, i denne ph.d. projekt, er der blevet gjort en indsats for at forbedre THD-ydeevnen, afbøde interharmoni, reducere kommunikationsafhængigheden og

opnå FAPC-funktioner for serie-PV-batterisystemer. Tilsvarende er der foreslået en beregningseffektiv VAPS PWM-metode, modificerede MPPT-metoder, et distribueret effektstyringssystem med lavt kommunikationskrav og fleksible strømstyringsstrategier, der giver løsninger til at integrere PV-paneler og batterier i distributionssystemer ved hjælp af seriekonfigurationer med forbedret output spændings-/strømydelse, reducerede omkostninger og forbedret strømstyringsfleksibilitet. Denne dokumenteret afhandling er "Distribueret kontrol og avanceret modulering af kaskadede fotovoltaiske batterikonvertersystemer".

Table of Contents

Thesis Details

Thesis Title: Distributed Control and Advanced Modulation of Cascaded Photovoltaic-Battery Converter Systems

Ph.D. Student: Yiwei Pan

Supervisors: Prof. Frede Blaabjerg, Aalborg University, Denmark
Prof. Yongheng Yang, Zhejiang University, China
Assist. Prof. Ariya Sangwongwanich, Aalborg University, Denmark

The main body of this thesis consists of the following papers:

Publications in Refereed Journals

J1. **Y. Pan**, A. Sangwongwanich, T. Pereira, Y. Yang, M. Liserre, and F. Blaabjerg, "Computation-efficient variable angle phase-shifting PWM method for cascaded H-bridge converters," *IEEE Trans. Power Electron*., 2022. Status: to be Submitted.

J2. **Y. Pan**, A. Sangwongwanich, Y. Yang, and F. Blaabjerg, "A phase-shifting MPPT to mitigate interharmonics from cascaded H-bridge PV inverters," *IEEE Trans. Ind. Appl*., vol. 57, no. 3, pp. 3052-3063, May-Jun. 2021.

J3. **Y. Pan**, A. Sangwongwanich, Y. Yang, and F. Blaabjerg, "Distributed control of islanded series PV-battery-hybrid systems with low communication burden," *IEEE Trans. Power Electron*., vol. 36, no. 9, pp. 10199-10213, Sept. 2021.

J4. **Y. Pan**, A. Sangwongwanich, Y. Yang, X. Liu, M. Liserre, and F. Blaabjerg, "Flexible active power control of distributed photovoltaic systems with integrated battery using series converter configurations," *IEEE J. Emerg. Sel. Top. Power Electron*., DOI: 10.1109/JESTPE.2021.3134203. Status: Early Access.

Publications in Conference Proceedings

C1. **Y. Pan,** A. Sangwongwanich, Y. Yang and F. Blaabjerg, "A Phase-shifting MPPT method to mitigate interharmonics from cascaded H-bridge PV inverters," in *Proc. IEEE APEC*, 2020, pp. 157-163.

C2. **Y. Pan,** A. Sangwongwanich, Y. Yang, and F. Blaabjerg, "A random sampling-rate MPPT method to mitigate interharmonics from cascaded H-bridge photovoltaic inverters," in *Proc. IEEE IPEMC-ECCE Asia*, 2020, pp. 3252-3257. (Best Paper Award)

C3. Y. Pan, A. Sangwongwanich, Y. Yang, and F. Blaabjerg, "A series interharmonic filter for cascaded H-bridge PV inverters," in *Proc. IEEE ECCE*, 2020, pp. 341-346.

C4. Y. Pan, Y. Yang, and F. Blaabjerg, "Distributed control of islanded series PV-battery-hybrid systems with low communication burden," in *Proc. IEEE PEDG*, 2020, pp. 315-321.

C5. Y. Pan, A. Sangwongwanich, Y. Yang, and F. Blaabjerg, "Optimization of reactive power distribution in series PV-battery-hybrid systems," in *Proc. IEEE ECCE*, 2021, pp. 520-525.

C6. Y. Pan, A. Sangwongwanich, Y. Yang, and F. Blaabjerg, "Flexible power control of distributed grid-connected series-photovoltaic-battery systems," in *Proc. IEEE APEC*, 2021, pp. 68-75. (Best Presentation Award)

This thesis has been submitted to the Faculty of Engineering and Science, Aalborg University for assessment in partial fulfillment of the Ph.D. degree. The thesis is a summary of the outcome from the Ph.D. project, which is documented based on the above publications. Parts of the results are used directly or indirectly in the extended summary of the thesis. The co-author statements have been made available to the assessment committee and are also available at the Faculty of Engineering and Science, Aalborg University.

Preface

This Ph.D. thesis summarizes the outcome from the Ph.D. project "*Control of Cascaded Power Converters for Photovoltaic-Battery Hybrid Systems*". This project is mainly supported by AAU Energy, Aalborg University, Denmark, and the Chinese Scholarship Council. In addition, some works are supported by the research project – Reliable Power Electronic based Power Systems (REPEPS) by THE VELUX FOUNDATIONS under Award Ref. No.: 00016591, and the attendance of some conferences and winter school, as well as the study abroad are in part funded by Otto Mønsteds Fond, Denmark. I would like to express my acknowledgement to the above institutions.

First, I would like to express my sincere gratitude to my supervisor Frede Blaabjerg, for his guidance, encouragement, and valuable suggestions during my Ph.D. period. I would also like to thank my co-supervisors Prof. Yongheng Yang and Assist. Prof. Ariya Sangwongwanich, who have provided me with a lot of professional advice on my studies, paper writing, and experiments. I have benefited a lot from the discussions with all my supervisors, and thank you all for your kindness, patience, and supports.

I would like to express my special gratitude to Prof. Marco Liserre for giving me the opportunity to work with Chair of Power Electronics, Kiel University, where I have broadened my knowledge in many aspects, and collaborated with my colleagues there on experiments and papers. My special gratitude goes to Mr. Thiago Pereira and other colleagues in Kiel University, for their help and hospitality during my stay in Kiel.

I am also grateful to Dr. Mengxing Chen, Mr. Jinkui He, Dr. Zhongting Tang, Mr. Chaochao Song, Mr. Zhengfa Zhang, Mr. Huizhong Sun, Dr. Kamran Ali Khan Niazi, as well as other colleagues at AAU Energy, Aalborg University, and Dr. Zhongyi Quan at Electronic Grid Systems Inc., for their kind help, supports, and discussions.

In the end, I would like to express my sincere gratitude to my parents and my girl-friend Miss Guiying Dong for their encouragement, company, and confidence for me. The world is becoming different, but your love will go on.

Yiwei Pan
Aalborg University, December 20, 2021

List of Symbols

$A_{\text{fund}}(x)$	Amplitude of the DC voltage oscillation obtained in the x^{th} Fourier transform
$C_{\text{bat,k}}$	Power capacity of the k^{th} battery
c_{p}	Local learning factor in the PSO algorithm
c_{g}	Global learning factor in the PSO algorithm
d	Reactive power distribution coefficient
f_0	Fundamental frequency of the output AC voltage
f_{c}	Carrier frequency
f_{fund}	Fundamental frequency of the SDFT algorithm
f_{MPPT}	Frequency of the MPPT control
$f_{\text{MPPT,\#k}}$	Frequency of the MPPT control for the k^{th} PV converter
f_{s}	Converter switching frequency
$f_{\text{s,LPF}}$	Sampling frequency of the digital low-pass filter
F_{v}	Fraction of the PV open-circuit voltage
$G_{\text{LPFk}}(s)$	Equivalent low-pass filter due to the power measurement
$G_{\text{LPF,total}}(s)$	Low-pass filter in the total voltage droop control
h_1	Multiple of the carrier frequency
h_2	Multiple of the fundamental frequency
I_{bat}	DC current of the battery
i_{d}	Grid current on the d-axis
i_{d}^*	Grid current reference on the d-axis
I_{DCk}	DC current of the k^{th} converter
i_{g}	Grid current
i_{g}^*	Grid current reference

$i_{g,fund}$	Fundamental grid current
$i_{Lac,bat}$	Inductor current of the output AC filter of the battery converter
$i^*_{Lac,bat}$	AC current reference of $i_{Lac,bat}$
$i_{Lac,k}$	AC current on the filter inductor of the k^{th} converter
i_{line}	AC line current
$\dot{I}_{line}$	Phasor of i_{line}
I_{MPP}	PV current at the maximum power point
I_{PVk}	DC current of the k^{th} PV panel
I'_{PVk}	Filtered DC current of the k^{th} PV panel
i_q	Grid current on the q-axis
i^*_q	Grid current reference on the q-axis
$k_{D,p}$	Droop coefficient of the active power control
$k_{D,q}$	Droop coefficient of the reactive power control
$k_{i,AOM,bat}$	Integral gain of the anti-overmodulation for the battery converter
$k_{i,AOM,PV}$	Integral gain of the anti-overmodulation for PV converters
$k_{i,p}$	Integral gain of the *P* control loop in the *PQ* decoupling control
$k_{i,p,total}$	Integral gain of the total active power control
$k_{i,q}$	Integral gain of the *Q* control loop in the *PQ* decoupling control
$k_{i,q,total}$	Integral gain of the total reactive power control
$k_{p,AOM,bat}$	Proportional gain of the anti-overmodulation for the battery converter
$k_{p,AOM,PV}$	Proportional gain of the anti-overmodulation for PV converters
$k_{p,p}$	Proportional gain of the *P* control loop in the *PQ* decoupling control
$k_{p,p,total}$	Proportional gain of the total active power control
$k_{p,q}$	Proportional gain of the *Q* control loop in the *PQ* decoupling control
$k_{p,q,total}$	Proportional gain of the total reactive power control
L_f	Inductance of the output AC filter

$m_{bat,k}$	Modulation index for the k^{th} battery converter
$M_{bat,k}$	Amplitude of $m_{bat,k}$
m_{filter}	Modulation index for the series interharmonic filter
m_k	Modulation index for the k^{th} converter
M_k	Amplitude of m_k
$m_{th,H}$	Upper threshold for the anti-overmodulation loop
$m_{th,L}$	Lower threshold for the anti-overmodulation loop
m_{total}	Amplitude of the total modulation index for the CHB
$\vec{M}$	A $1 \times n$ array of M_k, $\vec{M} = [M_1, M_2, \ldots M_n]$
n	Converter number of a series system
n_1	The number of battery converters
n_2	The number of PV converters
N_{SDFT}	Length of the SDFT sampling window
p_1 and p_2	Two weighting factors in the cost function for the optimization of the reactive power distribution
P^*_{bat}	Active power reference of the battery converter
$P^*_{bat,BMS}$	Power command from the battery management system
$P_{bat,k}$	Active power of the k^{th} battery converter
$P_{bat,lwlim}$	Lower power limit in the flexible active power control strategies for the battery converter
$P_{bat,uplim}$	Upper power limit in the flexible active power control strategies for the battery converter
P_{inc}	Power increment in each control period of the active power ramp-rate control
P_k	Active power of the k^{th} converter
P_{MPP}	Maximum power of the PV panel
P_{PVk}	Active power of the k^{th} PV converter
P^*_{PVk}	Active power reference of the k^{th} PV converter
$P_{PVk,avai}$	Available active power of the k^{th} PV converter

$P_{\text{PVk,avg}}$	Average active power of the k^{th} PV converter
$P_{\text{PVk,res}}$	Reserved power for the k^{th} PV converter
$P_{\text{PV,max}}$	Power of the PV converter that has the largest power among all PV converters
$P^*_{\text{PV,PLC}}$	Power limiting threshold for PV converters
$P_{\text{PV,th}}$	Threshold to enable the power curtailment of multiple PV converters
P_{step}	Power increment in each control period of the active power ramp-rate control, $P_{\text{step}} = P^*_{\text{total,PRR}} T_{\text{s}}$
P_{th}	Hysteresis band in the flexible active power control strategies
$P_{\text{th,nrrw}}$	The narrower hysteresis band for P_{th}
$P_{\text{th,wide}}$	The wider hysteresis band for P_{th}
P_{total}	Total active power of the entire system
P^*_{total}	Reference of P_{total}
$P_{\text{total,avai}}$	Total available power of the entire system
$P^*_{\text{total,avai}}$	Reference of $P_{\text{total,avai}}$
$P^*_{\text{total,init}}$	Initial total power reference
$P^*_{\text{total,lim}}$	Total power limiting command
$P^*_{\text{total,PRR}}$	Total power ramp-rate command
$P_{\text{total,res}}$	Total reserved power for the series system
$P^*_{\text{total,res}}$	Total power reserve command
PWM_{k}	PWM signals of the k^{th} converter
$\text{PWM}_{\text{bat,k}}$	PWM signals of the k^{th} battery converter
$Q_{\text{bat,k}}$	Reactive power of the k^{th} battery converter
Q_{k}	Reactive power of the k^{th} converter
Q^*_{k}	Reactive power reference of Q_{k}
Q_{PVk}	Reactive power of the k^{th} PV converter
Q_{total}	Total reactive power of the entire system
Q^*_{total}	Reference of Q_{total}

R_f	Resistance of the output AC filter
$rand([a,b])$	A random number between a and b
$r_{1,\beta}$ and $r_{2,\beta}$	Two random numbers within the range of [0,1] for the β^{th} particle in the PSO algorithm
S_k	Apparent power for the k^{th} converter
$\overline{S}$	Average apparent power of all converters
SoC_{dw}	Lower limit for the battery state-of-charge
SoC_k	State-of-charge of the k^{th} battery
SoC_{up}	Upper limit of the battery state-of-charge
T_d	Dynamic period of the variable angle phase-shifting PWM method
T_{MPO}	Period of the maximum power observation signal in the power reserve control strategy
T_{MPPT}	Period of the MPPT control
$T_{MPPT,\#k}(\alpha)$	MPPT period of the α^{th} MPPT cycle for the k^{th} PV converter
T_{opt}	Optimization period of the variable angle phase-shifting PWM method
T_{P1}	Duration time of Period I in the power reserve control strategy
T_{P2}	Duration time of Period II in the power reserve control strategy
T_s	Control period of the converter
T_{sat}	The period where the power reserve constraint fails to be maintained
U_{DCk}	DC voltage of the k^{th} converter
$\vec{U}_{DC}$	A $1 \times n$ array of U_{DCk}, $\vec{U}_{DC} = [U_{DC1}, U_{DC2}, \ldots U_{DCn}]$
U_f	Fundamental voltage of v_{inv}
U_{hkf}	Voltage amplitude of the harmonic with its frequency being f for the k^{th} converter cell
$U_{h,sum}$	Total harmonics in the output multilevel voltage
$U_{h,sum,new}$	The $U_{h,sum}$ with optimized carrier phase-shifting angles
$U_{h,sum,old}$	The $U_{h,sum}$ with carrier phase-shifting angles same as those in the last round of optimization

$v_{ac,bat}$	Output AC voltage of the battery converter
$v_{ac,k}$	Output AC voltage of the k^{th} converter
$v^{*}_{ac,k}$	Reference of $v_{ac,bat}$
$v_{ac,PVk}$	Output AC voltage of the k^{th} PV converter
$V_{bat,k}$	DC voltage of the k^{th} battery
$v_{c,k}$	Carrier of the k^{th} converter
$V_{DC,filter}$	DC voltage of the series interharmonic filter
$V'_{DC,filter}$	Filtered value of $V_{DC,filter}$
$V^{*}_{DC,total}$	Reference of the equivalent total DC voltage of the CHB
$V'_{DC,total}$	Filtered equivalent total DC voltage of the CHB
v_g	Grid voltage
$\dot{V}_g$	Phasor of v_g
$V_{g,nom}$	Amplitude of the grid nominal voltage
v_{inv}	Output multilevel voltage of the CHB
V_k	Amplitude of the output AC voltage of the k^{th} converter
$\dot{V}_k$	Phasor of $v_{ac,k}$
v^{*}_k	Modulation voltage of the k^{th} converter
$v^{\alpha}_{k,\beta}$	Velocity for the β^{th} particle and the k^{th} converter cell in the α^{th} iteration of the PSO algorithm
$\vec{v}^{\alpha}_{\beta}$	A $1 \times n$ array of $v^{\alpha}_{k,\beta}$, $\vec{v}^{\alpha}_{\beta} = [\, v^{\alpha}_{1,\beta}, v^{\alpha}_{2,\beta}, \ldots\ v^{\alpha}_{n,\beta} \,]$
v_{max}	Pre-defined maximum velocity in the PSO algorithm
V_{MPP}	PV voltage at the maximum power point
V^{*}_{MPPTm}	MPPT reference voltage of the m^{th} PV panel
V_{PVk}	DC voltage of the k^{th} PV panel
V'_{PVk}	Filtered value of $V_{PV,k}$
V^{*}_{PVk}	Reference of $V_{PV,k}$
$V_{PVk,f}$	Fundamental voltage of the DC-side oscillation of the k^{th} PV converter

$V^*_{\mathrm{PVk,f}}$	Fundamental voltage reference of the DC-side oscillation of the k^{th} PV converter
$V_{\mathrm{PV,OC}}$	PV open-circuit voltage
v_{step}	Perturbation step-size of the MPPT control
$v_{\mathrm{step,PLC}}$	Voltage perturbation step-size of the power limiting control
v_{total}	Total output AC voltage of the series system
v^*_{total}	Reference of v_{total}
V^*_{total}	Amplitude of the total AC voltage reference of the series system
Z_{f}	Line impedance
$\Delta M_{\mathrm{filter}}$	Adjustment on the modulation index of the interharmonic filter
ΔM_{k}	Adjustment on the modulation index of the k^{th} converter, which is generated by the corresponding secondary voltage controller
$\Delta M_{\mathrm{p,k}}$	Adjustment on the modulation index of the k^{th} converter, which is generated by the local active power controller
$\Delta M_{\mathrm{q,k}}$	Adjustment on the modulation index of the k^{th} converter, which is generated by the local reactive power controller
ΔP_{comp}	The assumed power for PV power curtailment
ΔP_{k}	Increment on P_{k}
$\Delta P_{\mathrm{total}}$	Increment on P_{total}
$\Delta P^*_{\mathrm{total,PRR}}$	Sum of the adjustment (P_{inc}) in the power ramp-rate control
ΔQ_{k}	Increment on Q_{k}
$\Delta Q_{\mathrm{total}}$	Increment on Q_{total}
ΔV_{k}	Increment on V_{k}
$\Delta V_{\mathrm{k},\theta}$	Increment on V_{k} caused by the phase-angle variation of $\dot{V}_{\mathrm{k}}$
$\Delta V^*_{\mathrm{PVm}}$	Sum of the adjustment of two anti-overmodulation loops, which is added to V^*_{MPPTm}
$\Delta\theta_{\mathrm{k}}$	Increment of the power factor angle of the k^{th} converter
$\Delta\varphi_{\mathrm{PVk}}$	Phase-angle difference between $\varphi_{\mathrm{PVk,ref}}$ and φ_{PVk}
$\Delta\omega_{\mathrm{k}}$	Increment of ω_{k}

ε_k	Active power distribution coefficient for the k^{th} battery converter
θ_f	Phase angle of the line impedance
θ_g	Phase angle of the grid voltage
θ_i	Phase angle of the grid current
θ_k	Power factor angle of the k^{th} converter
θ_{total}	phase angle of the total modulation index m_{total}
θ^*_{total}	Reference of θ_{total}
$\varphi_{0,k}$	Phase angle of the fundamental voltage of the k^{th} converter cell
$\vec{\varphi}_0$	A 1 × n array of $\varphi_{0,k}$, $\vec{\varphi}_0 = [\varphi_{0,1}, \varphi_{0,2}, \dots \varphi_{0,n}]$
$\vec{\varphi}^{best}_{c,g}$	A 1 × n array of $\varphi^{best}_{c,k,g}$, $\vec{\varphi}^{best}_{c,g} = [\varphi^{best}_{c,1,g}, \varphi^{best}_{c,2,g}, \dots \varphi^{best}_{c,n,g}]$
$\varphi_{c,k}$	Carrier phase-shifting angle of the k^{th} converter cell
$\varphi^{best}_{c,k,g}$	Global best carrier phase-shifting angle of the k^{th} converter cell in the PSO algorithm
$\varphi^{best}_{c,k,\beta}$	Local best carrier phase-shifting angle of the k^{th} converter cell for the β^{th} particle in the PSO algorithm
$\vec{\varphi}^{best}_{c,\beta}$	A 1 × n array of $\varphi^{best}_{c,k,\beta}$, $\vec{\varphi}^{best}_{c,\beta} = [\varphi^{best}_{c,1,\beta}, \varphi^{best}_{c,2,\beta}, \dots \varphi^{best}_{c,n,\beta}]$
$\vec{\varphi}^{\alpha}_{c,\beta}$	A 1 × n array of the carrier phase-shifting angles for the β^{th} particle in the α^{th} iteration of the PSO algorithm
$\vec{\varphi}^{*}_{c}$	A 1 × n array of the carrier phase-shifting angle references
φ_{hkf}	Phase-angle of the harmonic with its frequency being f for the k^{th} converter cell
φ_{PVk}	Phase-shifting angle of the DC-side oscillation of the k^{th} PV converter with respect to the 1st PV converter
$\varphi_{PVk,ref}$	Reference of $\varphi_{PV,k}$
ω_k	Angular frequency of the k^{th} converter
ω_{nom}	Nominal grid angular frequency
ω_{PSO}	Coefficient for updating the velocity of each particle in the PSO algorithm
ω^*_{total}	Angular frequency reference of the series system

List of Figures

List of Tables

Part I

Report

Chapter 1.
Introduction

1.1. Background

In past decades, due to the foreseen exhaustion of conventional fossil-based energy and the increasing environmental concern, many efforts have been globally directed towards developing and utilizing more renewable energy sources, like wind and solar photovoltaic (PV) energy [1]. The global PV expansion is still expected to accelerate, with new PV installations reaching 138 GW in the year of 2020, leading to a new annual record of 18% growth [2]. The distributed PV remains a driving force to the growth of the entire PV market, which had achieved an annual addition of 49 GW in 2020 [3].

As the power conditioning component in PV systems, the PV inverter is in charge of converting the DC power from PV panels to the AC power required by load or grid. Among various products, the string inverters and the central inverter are dominating the market of PV inverters (64.4% and 33.7% in 2021, respectively) [4], which connect a single string of PV modules and a PV array consisting of multiple strings to the grid, respectively, as shown in Figs. 1.1(a) and (b). For applications with multiple strings, multi-string inverters can also be employed, as shown in Fig. 1.1(c), where a dedicated DC/DC converter is employed to connect each string with a common DC bus, while performing the string-level maximum power point tracking (MPPT) control. However, as PV strings are directly connected to the DC links, module-level monitoring of PV panels cannot be achieved with the above inverters, which can result in power losses or even damaging of PV modules due to module mismatches (e.g., partial shading) [5]. To address this issue, module-level power electronic (MLPE) converters can be promising solutions, including the microinverter and the DC power optimizer [5], [6]. Although they are only accounting for a small market share, i.e., 1.4% for microinverters and 5.1% for power optimizers in 2020 [4], their market is growing rapidly [7]. In addition, for residential applications, microinverters and power optimizers have already been highly employed in the U.S. residential solar market [3].

The structure of conventional microinverters is shown in Fig. 1.1(d), where a DC/DC converter is firstly connected to PV panels to generate a voltage suitable for inverting and perform module-level MPPT. Then, each DC rail is connected to the grid (e.g., 230 V AC) with a DC/AC converter [5]-[9]. Microinverters offer benefits like independent functioning and monitoring of each PV module, enhanced safety owing to low DC operating voltages, and improved reliability by matching the lifespan of the individual modules [5]. However, as each PV module should be equipped with a DC/DC and a DC/AC converter, the main disadvantage for microconverters is the cost. As an

alternative, power optimizers are firstly installed on individual PV modules to perform module-level MPPT, and then, several power optimizers are series-connected to increase the voltage level, with the DC bus interfaced to the DC rail of a DC/AC inverter (i.e., string inverter) for grid-connection, as shown in Fig. 1.1 (e). Compared with expensive microinverters, the cost of power optimizers can be less [5]. Although both solutions can achieve module-level control and monitoring of PV panels, their efficiencies are still compromised owing to multiple conversion stages. For instance, the efficiency of microinverters varies between 90%-97% [4], and the efficiency of systems using power optimizers is also limited by that of the string inverters, even if power optimizers can achieve high efficiencies up to 99.5% [4].

On the other hand, due to the intermittent power generation of PV systems, certain adverse impacts appear, e.g., fluctuation of the grid frequency and voltage, and overloading of the distribution grid [6]. To avoid these issues and achieve schedulable power flow, energy storage (ES) units like batteries and super-capacitors are increasingly used together with PV panels [10]-[16]. The topologies in Figs. 1.1(c)-(e) are commonly used to integrate batteries with PV systems, with various products available in the market, e.g., the Huawei LUNA2000-5/10/15-S0 smart string ES system, and PV-battery systems based on microinverters and power optimizers [16]. Besides, multi-terminal converters have been studied to integrate PV-battery systems, providing more compact and efficient designs, as exemplified in Fig. 1.1(f) [17]-[19]. Nevertheless, they are not suitable for distributed controlled systems, as the control and modulation of the entire system are usually complex, which are achieved with a central controller [17]-[19]. For distributed systems, the implementation can be challenging, especially when the distributed generation (DG) units are geographically far away from each other.

To integrate distributed DG units in a simple and cost-effective manner, series-connected topologies have been investigated, where low voltage (LV) DG units including PV panels and batteries are directly plugged into the DC rail of each converter, as demonstrated in Fig. 1.1(g) [8], [12]-[15], [20]-[33]. This configuration provides a simple way to directly integrate LV-DC sources to AC grids without additional DC/DC converters, and thereby minimizing the cost, while increasing the efficiency [12]-[15]. Among various series configurations, the cascaded H-bridge (CHB) is one of the most commonly used system architecture, which has already been widely used in motor drive systems, static synchronous compensators (STATCOMs), and battery ES systems [8], [12]-[15]. Their application in PV systems has also been widely studied [20]-[26], but for now, no products are available for PV systems, which may be because of the grounding issue of PV modules. More specifically, PV modules in certain converter cells should withstand a high voltage (as high as the grid voltage) with respect to their frames, which are usually grounded. Thus, non-isolated CHB PV converters are only suitable for LV applications (e.g., connected to 220-V or 380-V AC grids) [20]. Despite this limitation, the series configurations are still attractive due to the removal of DC/DC converters. In addition, if isolated DC/DC converters are employed, distributed DG units can be easily connected to grids with higher voltage (e.g., medium voltage grid) using series configurations, by simply cascading more

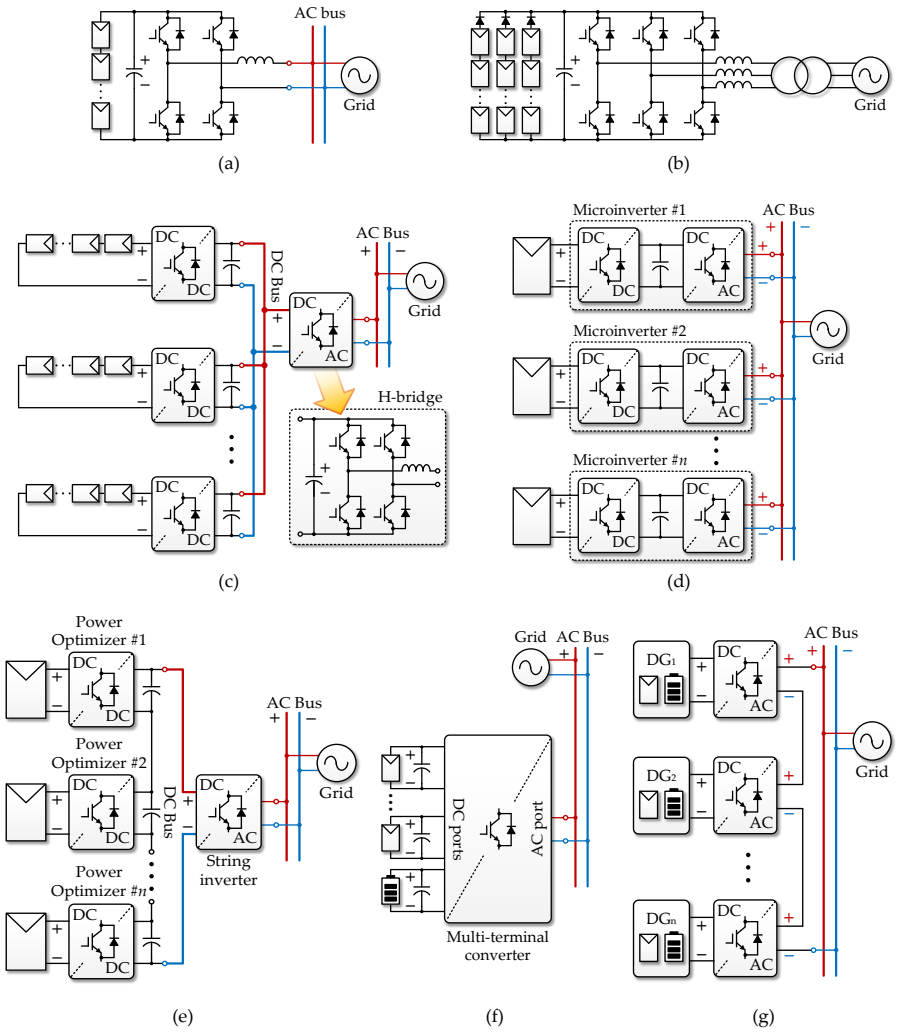

Fig. 1.1: Structures of distributed generation (DC) systems: (a) the H-bridge string inverter, (b) the three-phase central PV inverter with the low frequency transformer, (c) the multi-string inverter, (d) parallel-connected microinverters, (e) the string inverter with power optimizer for each PV module, (f) the multi-terminal converter, and (g) the series configuration. Source: [**J4**].

converter cells [25]. While for other topologies in Fig. 1.1(a)-(e), either components with larger ratings or complex multilevel topologies with a lot of components should be adopted, significantly increasing the cost of the system. Thus, the series configuration is promising for integrating PV panels and batteries in future DG systems.

In prior-art research, many control methods have been developed to enhance the power flow management [21], [22], achieve a distributed control [24], [27]-[30], ensure a stable operation [25], [26], [31]-[33], and improve the reliability of the CHB converters

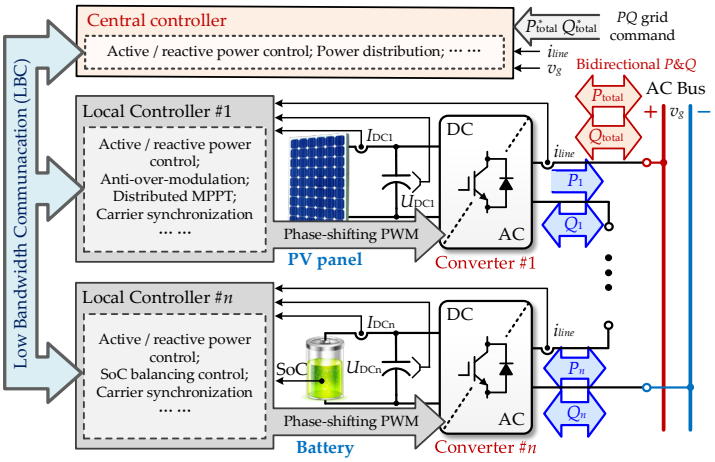

Fig. 1.2: Control diagram of the communication-based distributed series-PV-battery system, where i_{line} is the AC line current, $I_{dc,n}$, $U_{dc,n}$, P_n, Q_n, P_{total} and Q_{total} are the DC current, DC voltage, active and reactive power of converter #*n*, and total active and reactive power for the series system, respectively, and the variables with superscript "*" indicate that they are the reference values [37], [38].

[34], [35]. However, most research has focused on the output power and current response, and more importantly, the same type of DC sources had been plugged into separate DC rails of the series system. When different DC sources are interfaced, e.g., PV and battery systems, the control of the series system has not been fully investigated. In fact, the operating conditions of series-PV-battery systems are more complex than series systems with the same type of DC sources, where all converters should be coordinated controlled considering various requirements, such as MPPT for PV converters, state-of-charge (SoC) balancing for battery converters, power distribution among all converters, power scheduling of the entire system, etc. Nevertheless, these control requirements have not been considered previously. Only in a few studies [36]-[42], the coordinated operation of PV and battery units in series converter systems has been discussed. Among them, a typical distributed control scheme for series-PV-battery systems is developed in [36]-[38] as a hierarchical control, and the control diagram is briefly sketched in Fig. 1.2. With this, the series-PV-battery can achieve multiple control objectives from multiple timescales. They could include modulation, carrier synchronization, harmonic control, active and reactive power (*PQ*) regulation, MPPT control for individual PV converters, SoC balancing control among battery converters, and power scheduling of the system, etc. Nevertheless, certain challenges remain unaddressed (or not fully), which so far have limited the application of series-PV-battery systems, as listed below.

- **Challenge I:** The dynamic of the variable-angle phase-shifting (VAPS) pulse width modulation (PWM) is slow, leading to large harmonics around and above the switching frequency.

- **Challenge II:** Interharmonics can be amplified in series PV converters, which may cause fluctuation of the grid voltage and frequency, flickering of the lighting system and unintentional disconnection of the PV power plant, and have had limiting attention.
- **Challenge III:** Previous distributed control methods for series systems are either highly communication-denpendent, or only suitable for series-PV-battery systems with limited operating conditions (e.g., PFs of individual converters should be consistent), which are compromised in either the system cost or the power utilization of individual converters, respectively.
- **Challenge IV:** Most flexible active power control (FAPC) strategies are only suitable for single-inverter systems. When applying these strategies to series systems, the performance of the system can degrade. Adverse consequences include uneven loading of individual converters, unwanted PV power curtailment, battery over-charging / over-discharging, failure in maintaining the total power scheduling commands, etc.

In the following, the previous research in the above aspects and their limitations will be elaborated.

1.1.1. Modulation Methods for Series Systems

In previous research, a variety of modulation methods have been developed for series topologies. However, most of them were designed for series systems where the DC sources are of the same type. When applying these methods to series-PV-battery systems, they should be improved to accommodate the requirements of series-PV-battery systems. In addition, several modulation methods have been developed to cope with the conditions when different DC sources are adopted. These methods are based on different conventional modulation approaches, i.e., the phase shifting PWM (PSPWM) [43]-[46], the level shifting PWM (LSPWM) [45]-[47], and the space vector PWM (SVPWM) [15], [48]. Compared with the PSPWM, the LSPWM- and SVPWM-based methods have been widely developed for series systems with hybrid DC sources, owing to the possibility to utilize more redundant switching states for improved control flexibilities. For instance, in [15], single-phase SVPWM methods were proposed for series systems with hybrid DC sources, where some converters are interfaced with DC sources, while others only with DC capacitors. In [47], an LSPWM-based modulation strategy with the energy balancing capability was developed. With these approaches, certain converters can absorb the active power from other converters, which is similar to the operating conditions of series-PV-battery systems. Although these modulation methods can potentially be implemented for series-PV-battery systems, high-bandwidth communication (HBC) is required to transmit real-time variables and gating signals.

On the other hand, although the PSPWM has less control flexibilities than the LSPWM and SVPWM, it has been widely adopted due to its simplicity. By shifting the

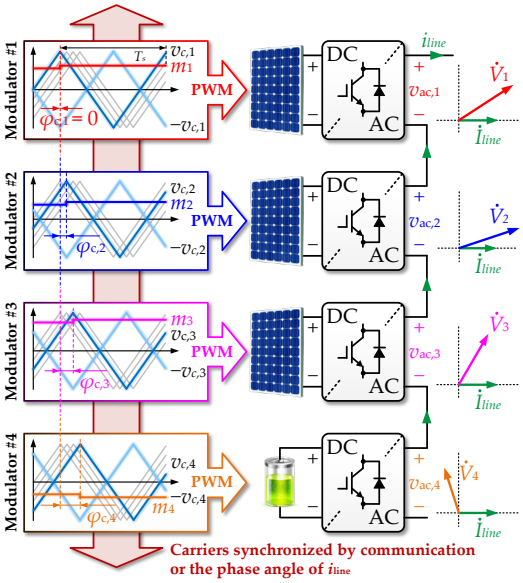

Fig. 1.3: Diagram of the VAPS PWM for a series-PV-battery system with three PV converters and one battery converter, where m_k and v_k are the modulation index and the output AC voltage for the k^{th} converter (k = 1, 2, 3, …), respectively, v_{ck} and $-v_{ck}$ are two opposite carriers for the k^{th} converter, and $\dot{V}_k$ and $\dot{I}_{line}$ are the phasors of $v_{ac,k}$ and i_{line}, respectively. Source: [**J1**].

carrier phase-angle of individual converters, the equivalent switching frequency of the system can be increased to $2nf_s$ (where n is the number of series-connected converters, and f_s is the switching frequency), and the harmonics of lower frequencies can be canceled, thereby reducing the THD of the total multilevel voltage [44]. In practice, the PSPWM can be easily implemented in distributed systems by using either the serial communication or the line current to synchronize the PWM generation of individual controllers [49], [50]. In addition, due to the interleaving effect of the PSPWM, the filter size of individual converters can be reduced, or even lumped as one single filter at the output of the entire series system, which will further reduce the cost [51].

However, when unbalances occur in series cells, i.e., the DC voltages, active and reactive power of individual converters are unequal, the conventional PSPWM will lose its harmonic cancellation property. This will lead to a significant increase in the THD of the total multilevel voltage [52]-[56]. To address this issue, several variable angle PSPWM methods have been proposed for CHB converters [52]-[56]. In these methods, the carrier phase shifting (PS) angles are adjusted to reduce the harmonic distortion of the total multilevel voltage. The diagram of the variable angle phase-shifting (VAPS) PWM method is illustrated in Fig. 1.3. According to [52] and [54], the optimal carrier PS angles can be analytically obtained for CHB converters to mitigate harmonics around $2f_s$. However, these approaches are mathematically unfeasible when the PFs of individual cells are different. Therefore, optimization algorithms have been developed [56]. Nevertheless, it still requires a large number of evolutionary

computations, which might use hundreds of milliseconds (dozens of fundamental cycles) to obtain the results with a common digital signal processor (DSP) [57]. When the outputs of individual converters change, the THD of the total output voltage may significantly grow, as the optimal carrier PS angles cannot be timely updated. Therefore, efforts should be made to improve the dynamics of the optimal VAPS PWM methods, as computation-efficient modulation strategies.

1.1.2. Interharmonics from PV Converters

Recently, interharmonics have become a concern in PV systems [58]-[61]. According to the laboratory tests [58], [59] and field measurements [60], [61], PV inverters can potentially generate interharmonics, which may cause fluctuations of the grid voltage and frequency, flickering of the lighting system, and unintentional disconnection of PV power plants [58]. As recommended by the IEEE Standard 1547-2018 and the International Electrotechnical Commission Technical Specifications (IEC TS) 63102 [62], [63], interharmonics should be assessed for grid-connected PV systems. In previous studies, it has been revealed that interharmonics can be generated by the MPPT perturbation of PV inverters [58]-[61]. More specifically, the PV voltage oscillation due to the MPPT will interact with the grid fundamental frequency through the control, contributing to the generation of interharmonics [58].

Many efforts have been made for mitigating interharmonics from single-phase full-bridge PV inverters. According to [64], lowering the MPPT sampling rate is a simple solution. However, this method slows down the dynamics of the MPPT, and may eventually affect the PV energy yield. In [65], an adaptive gain method, as well as a rate limiter method have been proposed to suppress interharmonics by avoiding the abrupt change on the AC current reference. Nevertheless, only interharmonics at a certain range of frequencies can be reduced (e.g., relatively high order). In [64], a random sampling-rate MPPT method was proposed, where PV voltage reference is perturbed with random frequencies. Although dominant interharmonics can be effectively mitigated with this approach, interharmonics cannot be completely suppressed, as the perturbation of MPPT remains. In addition, all above studies about the interharmonic mitigation were mainly focused on single-inverter systems. When PV converters are connected in series through the CHB topology, the oscillation on the total DC voltage (which is the sum of voltages of all series converters) will be magnified if the PV voltages of individual converters are oscillating in phase, as it is illustrated in Fig. 1.4 [**C1**]-[**C3**], [**J2**]. Consequently, the interharmonics from the series-topology-based PV inverter will become much larger than one single unit.

According to the experimental results of series-PV-battery systems, the power oscillations from PV converters can be effectively compensated by the battery, as well as interharmonics [37]-[40]. However, as the interharmonic issue is common for PV converters, it is not cost-effective to employ battery converters just to suppress interharmonics. Considering that the independent DC-side of the series system provides more control flexibility, more possibilities are expected to mitigate

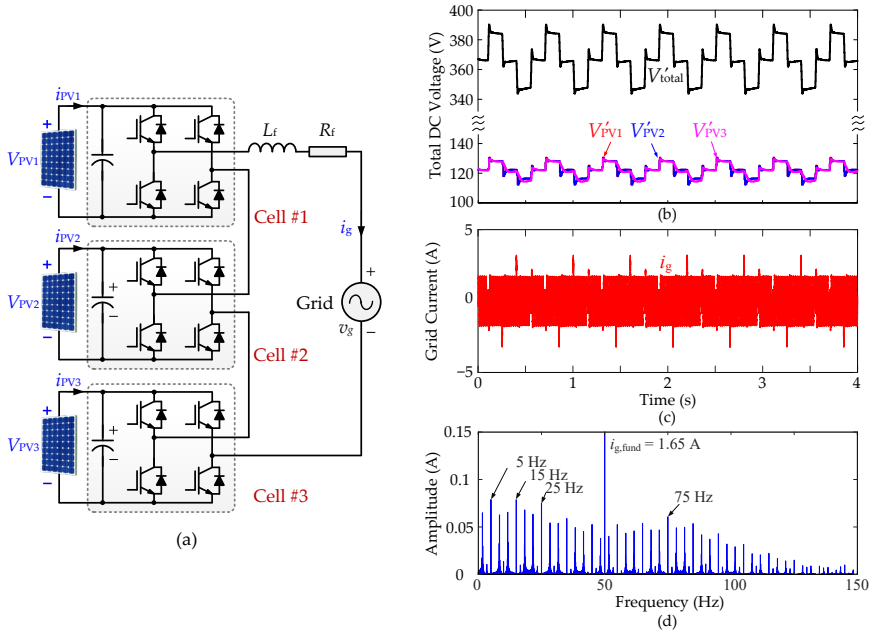

Fig. 1.4: Simulation results of a grid-connected 3-cell CHB PV inverter with in-phase MPPT perturbations on individual converters, where L_f and R_f refer to the impedance of the output AC filter: (a) topology of the CHB PV inverter, (b) filtered PV voltages, (c) grid current i_g, and (d) frequency spectrum of i_g, where $V'_{PV,k}$ and $V'_{DC,total}$ are the filtered PV voltage of the k^{th} PV converter and the filtered equivalent total DC voltage, respectively, and $i_{g,fund}$ is the grid fundamental component of i_g. Source: **[C2]**.

interharmonics, e.g., through the coordinated control of individual converters. Thus, interharmonic mitigation methods for series-topology-based PV inverters should be explored, while the methods should be achieved with minimum ES requirements.

1.1.3. Distributed Control Schemes for Series Systems

Although many distributed control methods have been developed for series-converter systems, most of them are not suitable for series-PV-battery systems. This is because only ideal DC sources with equal power sharing, or DC sources of the same type are considered in these methods [20]-[24], [66]-[71]. When different types of DC sources are adopted, e.g., PV and battery units, or the active/reactive power sharing among individual converters is unequal, these methods cannot be directly applied to series-PV-battery systems. In fact, the distributed control schemes suitable for series-PV-battery systems can only be found in a few studies [37]-[40]. Among them, one typical solution is a communication-based hierarchical control [37], [38]. However, this approach highly relies on a low-bandwidth communication (LBC) system. Through the LBC, many control signals should be transmitted in real-time between the central and local controllers, resulting in poor communication fault tolerance and low

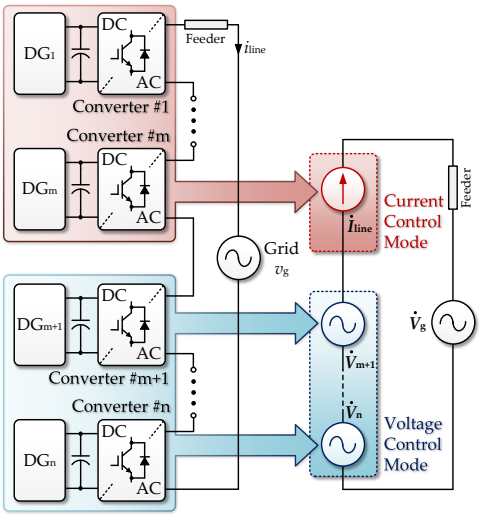

Fig. 1.5: Diagram of the current-/voltage-mode control for series converters.

reliability. As the communication burden will increase with the number of series converters, it will become more difficult to implement such hierarchical control. In addition, this LBC-dependent feature also challenges the plug-and-play implementation in distributed series systems.

To alleviate the dependency on communication, the current-/voltage-mode (CVM) control method has been proposed in [30] and [24], where one or several converters are controlled as a current source in a centralized manner, while others are distributed controlled as voltage sources, as shown in Fig. 1.5. With the CVM control, the communication burden can be alleviated. However, only the grid-connected operation with unity PF has been addressed in those studies [30], [24], [41], [40]. The non-unity PF operation has been considered in a few studies, but only the current-source-controlled converters are responsible for reactive power regulation, which limit the grid support capability of the entire system [70], [71]. Besides, as the CVM control is designed for grid-connected systems, it has rarely been studied on the islanded operation of series-PV-battery systems. In this case, the load PF is variable in a wide range, and the reactive power distribution will be of significance. If the load reactive power fails to be properly distributed, certain converters may easily suffer from overloading or even overmodulation, which may eventually lead to unwanted PV power curtailment [42], output voltage/current distortion or even instability of the system [38]. Therefore, this issue needs to be addressed for series-PV-battery systems.

On the other hand, due to the increasing grid-integration of PV systems, some adverse impacts appear, which are related to the voltage and frequency stability of the distribution grid, as mentioned previously. It thus calls for more flexibly controlled and grid-friendly PV systems to enhance the stability of DG systems [72]-[75]. As several grid codes have involved PV systems in their grid regulation [76]-[78], PV

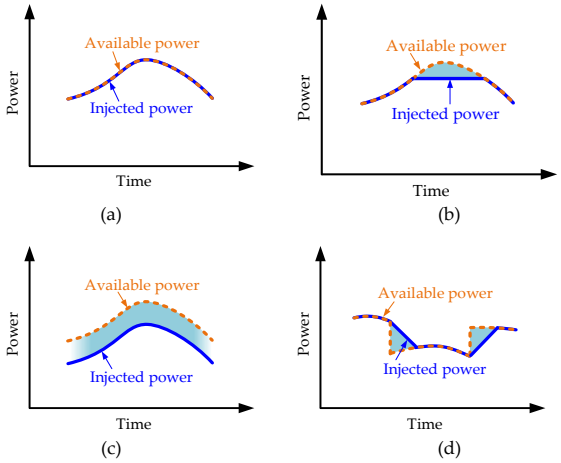

Fig. 1.6: Active power control functions for PV systems: (a) MPPT operation, (b) power limiting control (PLC), (c) power reserve control (PRC), and (d) power ramp-rate control (PRRC) [6]. Source: [**J4**].

systems should achieve three main functions in active power control, in addition to the MPPT operation, which are the power limiting control (PLC), power reserve control (PRC), and power ramp-rate control (PRRC), as exemplified in Fig. 1.6 [6]. However, for series-PV-battery systems, these flexible active power control (FAPC) strategies including the PLC, PRC, and PRRC have rarely been studied. Only in [40] and [41], a ramp-rate control and a virtual inertia control have been respectively developed. Moreover, when the battery power and SoC reach their upper or lower limits, the battery converter may fail to provide the power buffering. However, the battery SoC constraint in series-PV-battery systems has rarely been considered previously. Therefore, it requires further explorations on how to achieve those flexible power control functionalities, while ensuring optimal power utilization from the PV panels, and maintaining the battery power SoC within the required limits.

Another control challenge is overmodulation, which can occur in series-PV-battery systems when the islanded load is light, or the total power is flexibly controlled according to grid commands. According to [38], the overmodulation of PV converters can significantly affect the MPPT operation, leading to power oscillation and voltage and current distortions. To cope with this issue, one basic idea is to curtail the PV power yeilding. By doing so, the modulation indices of PV converters can be directly reduced, while the operating points of PV panels will move away from their maximum power points (MPPs), and be in the region of a higher voltage [33], [38]. Nevertheless, only the anti-overmodulation (AOM) control of PV converters can be found in the literature [33], [38]. In series-PV-battery systems, the overmodulation issue can be more complex, where not only the PV converters, but also the battery converters may suffer from overmodulation. Therefore, the main causes of overmodulation in series-PV-battery systems should be further analyzed, while the corresponding AOM control should be developed.

1.2. Project Motivation

1.2.1. Research Questions

As discussed above, although a variety of approaches have been proposed to improve the performance of series converter systems, most of them are not suitable for series-PV-battery systems. Moreover, several essential issues in series-PV-battery systems remain unaddressed, which limit the application of series-PV-battery systems. This Ph.D. project aims to tackle those control-related challenges. The overall research goal of this Ph.D. project is "to improve the control schemes for better integration of distributed PV panels and batteries into distribution systems using series configurations".

To achieve this goal, on one hand, improved modulation and distributed control strategies have been developed considering various operating conditions of series-PV-battery systems. On the other hand, it is also highly demanded to reduce the cost of the overall system while ensuring high power quality and maximize energy harvesting. Accordingly, the following questions are considered:

- **Q1:** How to improve the dynamic performance of the VAPS PWM method for series-PV-battery systems?

- **Q2:** How to mitigate large interharmonics from series-connected PV converters with the minimal requirement of batteries, or even without batteries in a cost-effective way?

- **Q3:** What can be a suitable distributed control scheme for series-PV-battery systems with low communication requirements?

- **Q4:** What could be the additional flexibility for power regulation of individual converters while considering PV power harvesting, battery power, and battery SoC status?

1.2.2. Research Objectives

With the above research questions, the objectives of this Ph.D. project are summarized as follows:

- **O1 – Develop a hardware computation-efficient approach for the VAPS PWM method using parallel computing.**
  To address Q1, one possible solution is to accelerate the optimization process using parallel computing, which can be achieved using additional hardware, e.g., FPGAs. In this Ph.D. project, efforts will be made on how to implement the VAPS PWM method in an FPGA with a minimum hardware requirement.

Then, the improvements on the dynamic performance will be evaluated through experiments.

- **O2 – Explore the interharmonic emission mechanism for series PV converters, and accordingly develop interharmonic mitigation methods.**
  To answer Q2, solutions to suppress interharmonics without the battery converter need to be developed, which can possibly be achieved by the coordinated control of multiple series PV converters. Then, both the dynamic and steady-state performance of the proposed control approaches need to be investigated, evaluated and compared with each other considering the requirements of practical applications.

- **O3 – Advance the distributed control methods for series-PV-battery systems with low communication requirements**
  To address Q3, a distributed control scheme with low communication requirements should be developed, where the power control and AOM control of individual converters, reactive power distribution among all converters should be considered. A stability analysis on the proposed control is also required, and based on that, the guidelines on how to tune the control parameters will be provided.

- **O4 – Propose flexible active power control methods for grid-connected series-PV-battery systems**
  To answer Q4, FAPC strategies should be designed for series-PV-battery systems to achieve the PRRC, PLC, and PRC functionalities. Those strategies are developed based on the distributed control architecture proposed in this Ph.D. project (O3). Various constraints should be considered when developing the FAPC strategies, including the total active power constraints, charging/discharging power and SoC constraints for the battery converter, as well as the available PV power and the MPP estimation of each PV converter.

1.3. Project Limitations

There are still several limitations in this Ph.D. project, as listed in the following:

- **L1:** Since this Ph.D. project is mainly focused on the control-related issues of series-PV-battery systems, how to determine the capacity and power rating of the battery system is not considered. As the design of the battery system should consider various factors, such as the requirements of distributed systems, power ratings and generation profiles of PV converters, etc., it is a complex issue, and it remains to be addressed in future studies. Nevertheless, several guidelines have already been developed for conventional PV-battery

systems in the literature and application notes, which can be referred to when sizing the battery for series-PV-battery systems [79]-[82].

- **L2:** In this Ph.D. project, only the single-phase system has been discussed. On the other hand, there are more control challenges in three-phase series-PV-battery systems. For instance, the three-phase unbalance is a common issue, which includes both the three-phase generation unbalance and the grid unbalance [34], [83]-[85]. In those cases, how to coordinatively control the individual converters with three-phase balanced power generation and optimized power distribution among all converters requires further exploration. Besides, various three-phase series topologies have provided more flexibilities in integrating PV panels and batteries [86]-[88], e.g., through hybrid cascaded converters [86], [87]. It indicates that the configuration and control of three-phase series-PV-battery systems can be more complex, which are expected to be addressed in future studies.

- **L3:** In the experiments, PV/battery simulators have been employed to emulate the behavior of PV panels and batteries, and only down-scaled tests were performed. Nevertheless, it is sufficient to validate the effectiveness and demonstrate the performance of the proposed control on the down-scaled experimental setup using PV/battery simulators, although the operation of the series-PV-battery system can be more complex in practice.

1.4. Thesis Outline

The dissertation consists of two main parts: Report and Selected Publications. In Report, the outcomes of this Ph.D. project are summarized based on the publications during the Ph.D. study, as illustrated in Fig. 1.7 (Journals – J, Conference - C). The Report is organized with five chapters, which are briefly introduced in the following:

- **Chapter 1 – Introduction**
  In Chapter 1, the background of the research project is discussed, and the focus of which is put on the limitations in state-of-the-art control methods for series-PV-battery systems. Accordingly, the objectives of this Ph.D. project are clarified.

- **Chapter 2 – Computation-efficient variable angle phase-shifting PWM**
  In this chapter, an FPGA-based VAPS PWM method is developed to improve the harmonic optimization speed for cascaded converters, and the performance of the developed method is evaluated and compared with the conventional DSP-based approach. The hardware requirement of the proposed method, extendibility of the method for more cascaded cells, and potential methods that can further improve the optimization, are discussed.

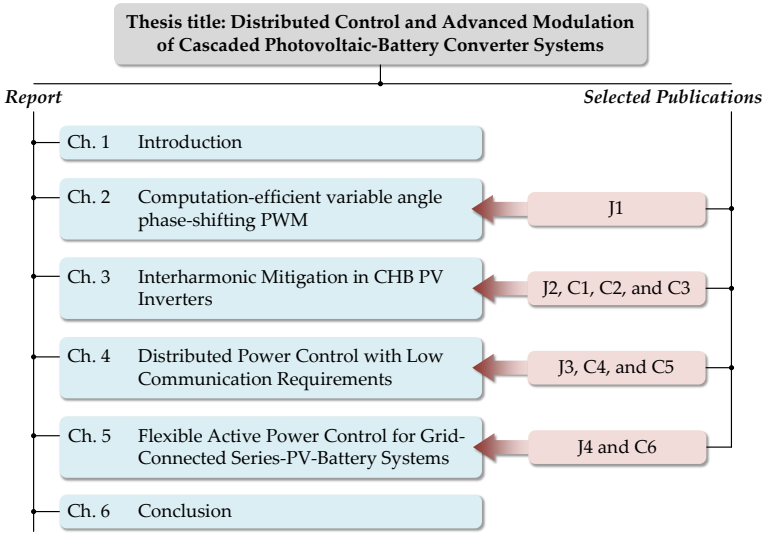

Fig. 1.7: Structure of this Ph.D. thesis including related publications to the chapters.

- **Chapter 3 – Interharmonic mitigation for CHB PV inverters**
  In this chapter, the interharmonic issue in series PV converters is discussed firstly. Then, three interharmonic mitigation methods (phase-shifting MPPT, random sampling-rate MPPT, and the series interharmonic filter) are introduced and compared. Furthermore, hybrid MPPT methods are developed to further suppress interharmonics.

- **Chapter 4 – Distributed power control with low communication requirements**
  In this chapter, a distributed control architecture for islanded series-PV-battery systems is developed, where the *PQ* control for individual converters, AOM of both the PV and battery converters, and power distribution among all converters, are achieved with very low communication requirements. A small-signal model is also developed for the stability analysis of the proposed control.

- **Chapter 5 – Flexible active power control for series-PV-battery systems**
  In this chapter, FAPC strategies including the PRRC, PLC, and PRC strategies are proposed for series-PV-battery systems, which are realized by the coordinated control of all converters. Various control constraints are considered in the control, including the total power ramp-rate/limiting/reserve constraints, battery charging/discharging power and SoC limits, available PV power, and the MPP estimation of each PV converter.

- **Chapter 6 – Conclusion**
  In this chapter, concluding remarks and the main contributions of this Ph.D. thesis are summarized, and the future research perspectives are presented.

1.5. List of Publications

The outcomes during the Ph.D. study have been published in journals and conference proceedings. Parts of them are used in the Ph.D. thesis (**J1**-**J4**; **C1**-**C6**), as listed below.

Journal Papers

J1. **Y. Pan**, A. Sangwongwanich, T. Pereira, Y. Yang, M. Liserre, and F. Blaabjerg, "Computation-efficient variable angle phase-shifting PWM method for cascaded H-bridge converters," *IEEE Trans. Power Electron*., 2022. Status: to be Submitted.

J2. **Y. Pan**, A. Sangwongwanich, Y. Yang, and F. Blaabjerg, "A phase-shifting MPPT to mitigate interharmonics from cascaded H-bridge PV inverters," *IEEE Trans. Ind. Appl*., vol. 57, no. 3, pp. 3052-3063, May-Jun. 2021.

J3. **Y. Pan**, A. Sangwongwanich, Y. Yang, and F. Blaabjerg, "Distributed control of islanded series PV-battery-hybrid systems with low communication burden," *IEEE Trans. Power Electron*., vol. 36, no. 9, pp. 10199-10213, Sept. 2021.

J4. **Y. Pan**, A. Sangwongwanich, Y. Yang, X. Liu, M. Liserre, and F. Blaabjerg, "Flexible active power control of distributed photovoltaic systems with integrated battery using series converter configurations," *IEEE J. Emerg. Sel. Top. Power Electron*., DOI: 10.1109/JESTPE.2021.3134203. Status: Early Access.

- **Y. Pan,** Y. Yang, J. He, A. Sangwongwanich, C. Zhang, Y. Liu, and F. Blaabjerg, "A dual-loop control to ensure fast and stable fault-tolerant operation of series resonant DAB converters," *IEEE Trans. Power Electron*., vol. 35, no. 10, pp. 10994-11012, Oct. 2020.
- Z. Quan, Y. W. Li, **Y. Pan**, C. Jiang, Y. Yang, and F. Blaabjerg, "Reconsideration of grid-friendly low-order filter enabled by parallel converters," *IEEE J. Emerg. Sel. Topi. Power Electron*., vol. 9, no. 3, pp. 3177-3188, Jun. 2021.

Conference Papers

C1. **Y. Pan,** A. Sangwongwanich, Y. Yang and F. Blaabjerg, "A Phase-shifting MPPT method to mitigate interharmonics from cascaded H-bridge PV inverters," in *Proc. IEEE APEC*, 2020, pp. 157-163.

C2. Y. Pan, A. Sangwongwanich, Y. Yang, and F. Blaabjerg, "A random sampling-rate MPPT method to mitigate interharmonics from cascaded H-bridge photovoltaic inverters," in *Proc. IEEE IPEMC-ECCE Asia*, 2020, pp. 3252-3257.

C3. Y. Pan, A. Sangwongwanich, Y. Yang, and F. Blaabjerg, "A series interharmonic filter for cascaded H-bridge PV inverters," in *Proc. IEEE ECCE*, 2020, pp. 341-346.

C4. Y. Pan, Y. Yang, and F. Blaabjerg, "Distributed control of islanded series PV-battery-hybrid systems with low communication burden," in *Proc. IEEE PEDG*, 2020, pp. 315-321.

C5. Y. Pan, A. Sangwongwanich, Y. Yang, and F. Blaabjerg, "Optimization of reactive power distribution in series PV-battery-hybrid systems," in *Proc. IEEE ECCE*, 2021, pp. 520-525.

C6. Y. Pan, A. Sangwongwanich, Y. Yang, and F. Blaabjerg, "Flexible power control of distributed grid-connected series-photovoltaic-battery systems," in *Proc. IEEE APEC*, 2021, pp. 68-75.

- **Y. Pan,** Y. Yang, J. He, A. Sangwongwanich, and F. Blaabjerg, "Low-frequency oscillation suppression in series resonant dual-active-bridge converters under fault tolerant operation," in *Proc. IEEE ECCE*, 2019, pp. 1499-1505.
- W. Liu, **Y. Pan**, and Y. Yang, "Small-signal modeling and dynamic analysis of the quasi-Z-source converter," in *Proc. IEEE IECON*, 2019, pp. 5039-5044.
- S. He, **Y. Pan**, D. Zhou, X. Wang, and F. Blaabjerg, "Current harmonic analysis of multisampled LCL-type grid-connected inverter," in *Proc. IEEE ECCE*, 2020, pp. 4329-4335.
- Y. Wei, T. Pereira, **Y. Pan**, M. Liserre, F. Blaabjerg, and H. A. Mantooth, "RMS current based automated optimal design tool for LLC resonant converters," in *Proc. IEEE APEC*, 2022, Accepted.
- C. Song, Y. Yang, A. Sangwongwanich, **Y. Pan**, and F. Blaabjerg, "Modeling and analysis of 2/3-level dual-active-bridge DC-DC converters with the five-level control scheme," in *Proc. IEEE APEC*, 2021, pp. 1958-1963.

Book Chapter

- A. Sangwongwanich, J. He, and **Y. Pan**, "*Advanced Power Control of Photovoltaic Systems*," in Control of Power Electronic Converters and Systems, Vol. 3, Frede Blaabjerg, Ed.: Elsevier, 2021, ch. 15.

Chapter 2. Computation-Efficient Variable Angle Phase-Shifting PWM

2.1. Background

According to the discussions in Chapter 1, the variable angle phase-shifting (VAPS) PWM methods can be applied to distributed series systems. Considering the operating conditions of series-PV-battery systems, where the phase angles of the fundamental voltage for different converter cells are usually none identical, it is difficult to analytically obtain the optimal carrier phase shifting (PS) angles [52], [54], and [55], which are mathematically unfeasible. In such cases, the most suitable VAPS PWM methods are obtained by using mathematical searching algorithms, e.g., the exchange marketing algorithm (EMA) [56] and the particle swarm optimization (PSO) [57]. However, these methods have slow dynamics. For instance, the optimal carrier PS angles are calculated every two seconds in [57] (100 fundamental grid cycles). This is due to a large number of computations are involved in the optimization, which is time-consuming when it is implemented with ordinary digital signal processors (DSPs). Due to the slow optimization rate, the output harmonic suppression performance cannot be guaranteed within dozens of grid fundamental cycles, when the calculation of the optimal angles is not accomplished. During that period, the high-frequency voltage harmonics can be significant, leading to increased power losses and higher electromagnetic interference (EMI) issues. In fact, the optimization speed of the VAPS PWM method has not been evaluated previously, while only steady-state performance has been demonstrated [56], [57].

Therefore, efforts should be made to improve the optimization speed of the VAPS PWM method. In this chapter, firstly, a PSO-based algorithm to search the optimal carrier phase-shifting (PS) angles for CHB converters is introduced, as well as its dynamic response when it is realized using a DSP. Then, the implementation of the optimization algorithm with FPGAs is discussed, and the dynamic of the VAPS PWM method with the hardware implementation is compared with the conventional DSP-based method. The performance of the proposed method is also evaluated through

quantitative analysis of the execution time and hardware resources, and methods to further improve the optimization are also discussed.

2.2. Variable Angle Phase-Shifting PWM Method

2.2.1. Particle Swarm Optimization Algorithm

The objective of PSO-based algorithms [57] is to find a set of PS angles for individual converters that minimizes the total harmonics in the output voltage / current of multi-converter systems. The analytical expressions of the total harmonics in CHB converters can be obtained through a double integral Fourier analysis [57], [89]

$$U_{\mathrm{h,sum}} = \sqrt{\sum_{f=f_0+1}^{\infty}\left[\left(\sum_{k=1}^{n} U_{\mathrm{hkf}}\cos\varphi_{\mathrm{hkf}}\right)^2 + \left(\sum_{k=1}^{n} U_{\mathrm{hkf}}\sin\varphi_{\mathrm{hkf}}\right)^2\right]} \tag{2.1}$$

$$\varphi_{\mathrm{hkf}} = \varphi_{\mathrm{hk}\left(\mathrm{h}_1\mathrm{f_c}+\mathrm{h}_2\mathrm{f}_0\right)} = 2h_1\pi\varphi_{\mathrm{c,k}} + \left(2h_2-1\right)\varphi_{\mathrm{0,k}} \tag{2.2}$$

$$U_{\mathrm{hkf}} = U_{\mathrm{hk}\left(\mathrm{h}_1\mathrm{f_c}+\mathrm{h}_2\mathrm{f}_0\right)} = \frac{\sqrt{2}U_{\mathrm{DCk}}}{\pi h_1} J_{2\mathrm{h}_2-1}\left(h_1\pi M_{\mathrm{k}}\right)\cos\left(h_1+h_2-1\right) \tag{2.3}$$

Here, $U_{\mathrm{h,sum}}$ is the total harmonics in the output multilevel voltage. n is the number of cascaded cells. U_{hkf} and φ_{hkf} are the voltage amplitude and phase-angle of the harmonics with its frequency being f ($f = h_1 f_c + h_2 f_0$) for the k^{th} converter cell, with f_0 and f_c being the fundamental and carrier frequencies, respectively. M_k, U_{DCk}, $\varphi_{0,k}$ and $\varphi_{c,k}$ are the modulation index, DC voltage amplitude, phase angle of the fundamental voltage and the carrier PS angle of the k^{th} converter cell, respectively. h_1 and h_2 are multiples of the carrier and fundamental frequencies, respectively ($h_1 > 0$). $J_i(x)$ is the Bessel function given as

$$J_{\mathrm{i}}\left(x\right) = \sum_{j=0}^{\infty}\frac{\left(-1\right)^j}{j!\left(j+i\right)!}\left(\frac{x}{2}\right)^{2j+i}. \tag{2.4}$$

From (2.1)-(2.3), it can be noticed that for given $\vec{U}_{\mathrm{DC}}$, $\vec{M}$ and $\vec{\varphi}_0$ ($\vec{U}_{\mathrm{DC}} = [U_{\mathrm{DC1}}, U_{\mathrm{DC2}}, \ldots U_{\mathrm{DCn}}]$, $\vec{M} = [M_1, M_2, \ldots M_n]$, and $\vec{\varphi}_0 = [\varphi_{0,1}, \varphi_{0,2}, \ldots \varphi_{0,n}]$), it is difficult to obtain an analytical solution of $\vec{\varphi}_c = [\varphi_{c,1}, \varphi_{c,2}, \ldots \varphi_{c,n}]$ that minimizes $U_{\mathrm{h,sum}}$ in (2.1). To solve this large-scale nonlinear optimization problem, the PSO algorithm is employed, as illustrated in Fig. 2.1. As it is shown in Fig. 2.1, the PSO-based algorithm has an iteration loop, which include: 1) initialization, 2) calculation of $U^2_{\mathrm{h,sum}}$ values, and 3) the update of all particles. When the optimized $\vec{\varphi}^{\,\mathrm{best}}_{\mathrm{c,g}}$ (the global best solution) is obtained after a certain number of iterations, $U^2_{\mathrm{h,sum}}$ will be compared with that of $\vec{\varphi}^{\,*}_{\mathrm{c}}$, which is the carrier PS angles at the current state. If $U^2_{\mathrm{h,sum,new}}$ is smaller than $U^2_{\mathrm{h,sum,old}}$, the carrier PS angles $\vec{\varphi}^{\,*}_{\mathrm{c}}$ will be replaced by the optimized values. In the algorithm,

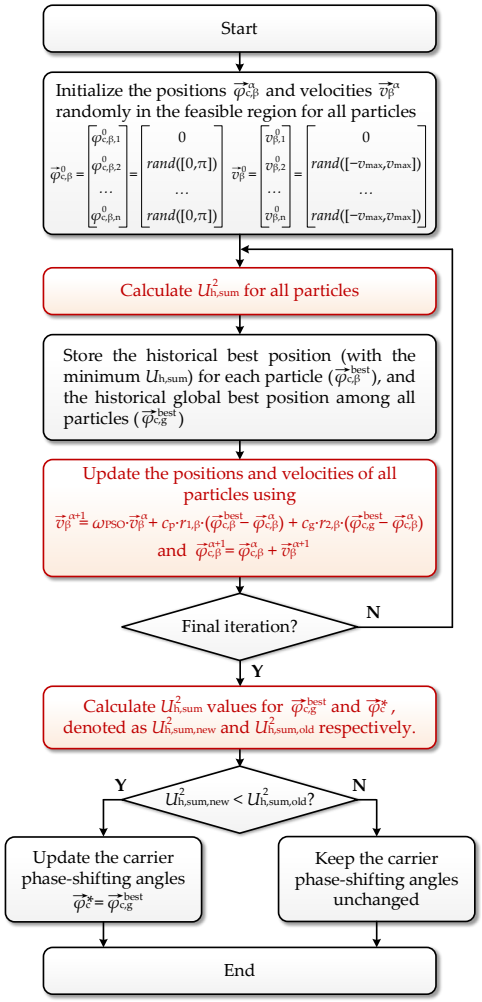

Fig. 2.1: Flow chart of the PSO-based algorithm for the VAPS PWM method to search for the optimal carrier PS angles, where $\vec{\varphi}_{c,\beta}^{\alpha}$ and $\vec{v}_{\beta}^{\alpha}$ are the arrays of the carrier PS angles and velocities for the β^{th} particle in the α^{th} iteration, respectively, $rand([a,b])$ is a random number between a and b, v_{max} refers to the pre-defined maximum velocity, ω_{PSO}, c_P, and c_g are three coefficients for updating the velocity of each particle, respectively, and $r_{1,\beta}$ and $r_{2,\beta}$ are two random numbers within the range of [0,1] for the β^{th} particle [**J1**].

$U_{h,sum}^{2}$ is used instead of $U_{h,sum}$ to avoid the square root calculation, and only the main harmonics are involved in the calculation, e.g., $h_1 = 1$, 2, and $h_2 = -2$, -1, 0, 1, 2, 3.

The evolution response of the PSO-based algorithm is demonstrated in **F**ig. 2.2, where 20 independent cases are performed for the optimization of a 4-cell CHB converter with 100 particles. It can be noticed that optimal solutions can be obtained after 10 to 20 iterations. Obviously, a large number of calculations are involved in the PSO-based VAPS PWM method, where $U_{h,sum}^{2}$ should be calculated for all particles in each

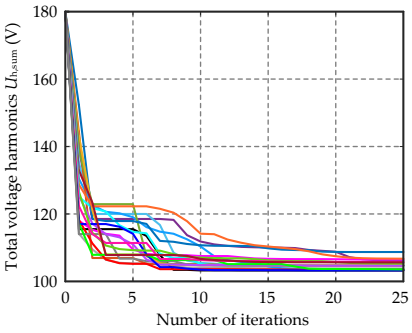

Fig. 2.2: Twenty evolution responses of the carrier PS angle optimization for a 4-cell CHB converter with 100 particles, where $\vec{U}_{DC}$ = [120 V, 100 V, 110 V, 80 V], $\vec{M}$ = [0.9, 0.8, 0.7, 0.3], and $\vec{\varphi}_0$ = [0.1963, 0, 0, 3.1293]. Source: [**J1**].

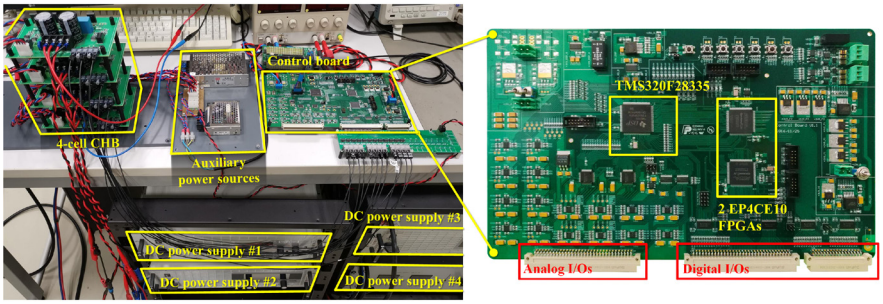

Fig. 2.3: Photo of the experimental platform. Source: [**J1**].

round of iteration. For instance, an optimization with 100 particles and 10 times of iteration requires 1000 times in the calculation of $U_{h,sum}^2$. Considering that (2.1) is complex, it will take longer time (hundreds of milliseconds) for a DSP to solve the optimization problem. When the output voltage of each converter changes, the conventional VAPS PWM methods cannot timely update the optimized carrier PS angles. During the period when the optimization is not ready, the power quality performance of the converter can be degraded due to the presence of high-frequency harmonics.

In practice, although the calculations of the Bessel function and trigonometric functions can be simplified by using lookup tables (LUTs) to accelerate the optimization, the computational burden remains high. To demonstrate the dynamic response of the conventional DSP-based VAPS PWM method, experiments have been performed on a 4-cell CHB converter, as demonstrated in Fig. 2.3, where the optimization algorithm is implemented in TMS320F28335 DSP (ω_{PSO} = 0.5, c_p = c_g = 0.25), and the switching frequency f_s for one bridge arm is 1.25 kHz. Two cases have been tested, where their reference voltages are given in Fig. 2.4(a) and (b), respectively. Experimental results for Case 1 are shown in Figs. 2.5 and 2.6, where the optimization

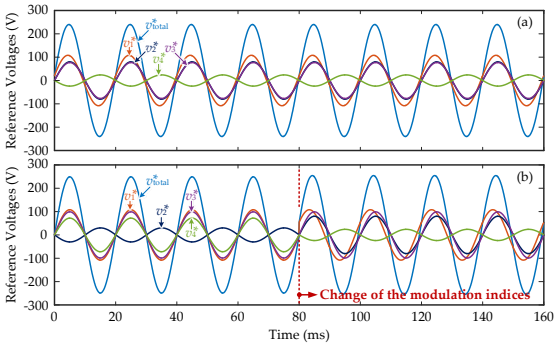

Fig. 2.4: Reference voltages in the experiments with $\vec{U}_{dc}$ = [120 V, 100 V, 110 V, 80 V]: (a) Case 1: $\vec{M}$ = [0.9, 0.8, 0.7, 0.3], and $\vec{\varphi}_0$ = [0.1963, 0, 0, 3.1293], and (b) Case 2: the modulation indices change from $\vec{M}$ = [0.9, 0.3, 0.9, 0.9] and $\vec{\varphi}_0$ = [0, 3.1293, 0, 0] to $\vec{M}$ = [0.9, 0.8, 0.9, 0.3] and $\vec{\varphi}_0$ = [0.5277, 0, 0, 3.1293], where v_k^* and v_{total}^* are the reference AC voltages for the k^{th} converter cell and total AC voltage reference, respectively. Source: [**J1**].

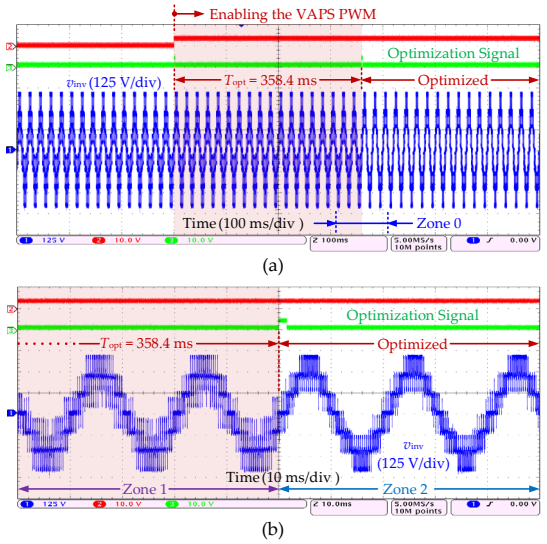

Fig. 2.5: Experimental results of Case 1 with the DSP-based VAPS PWM: (a) output multilevel voltage, and (b) the zoomed-in plot of Zone 0 in Fig. 2.5(a). Source: [**J1**].

is executed with 100 particles and 20 times of iteration. Initially, the conventional PSPWM method with fixed PS angles is employed [43]. When the VAPS PWM method is enabled, the output voltage of the CHB converter remains unchanged for 358.4 ms, which is the time until the optimized carrier PS angles are calculated. In steady state, the total harmonic distortion (THD) of the multilevel voltage v_{inv} is reduced from 44.85% to 35.91% with the optimized carrier PS angles ($\vec{\varphi}_c^*$ = [0, 2.1967, 1.0063, 2.7121]) and harmonic components near $2f_s$ are significantly suppressed. However, it requires almost 18 fundamental cycles for the algorithm to find the optimal carrier PS angles, which results in a slow speed.

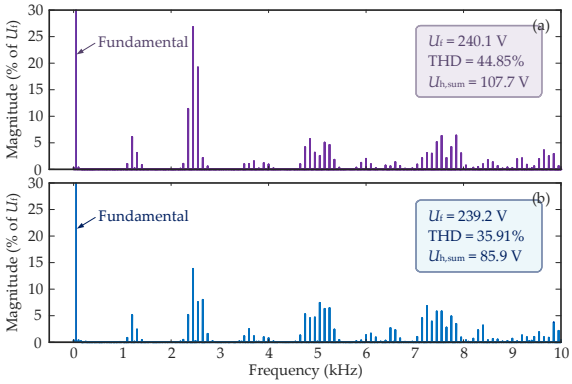

Fig. 2.6: Frequency spectra of the multilevel voltage in (a) Zone 1 and (b) Zone 2 of Fig. 2.5(b), where U_f is the fundamental voltage of v_{inv}. Source: [**J1**].

Case 2 demonstrates the performance when the outputs of the individual converters change according to the voltage references in Fig. 2.4(b), and the carrier PS angles are continuously updated with the VAPS PWM implemented in the DSP. Experimental results are shown in Fig. 2.7, and 100 particles with 10 times of iteration are employed in this test. Initially, the CHB converter is operating with optimal carrier PS angles ($\vec{\varphi}_c^*$ = [0, 1.1290, 2.0249, 1.6690], Zone 3 in Fig. 2.7(b)). After the change of the modulation indices, the THD performance of v_{inv} is degraded for 580 ms, until the new optimal angles $\vec{\varphi}_c^*$ = [0, 0.0736, 2.1598, 1.0677] are obtained by the optimization algorithm. The harmonic performance is even worse during the transition, i.e., in the first 11 fundamental cycles (Zone 4 in Figs. 2.7(b) and (c)), where the THD of v_{inv} is increased to 58.03%, which is much higher than the initial 31.50% and the steady-state 37.74%, as shown in Figs. 2.7 and 2.8. After that, the voltage harmonic performance is improved when the optimized PS angles are obtained in the first round of optimization after the reference voltage step change (Zone 5 in Figs. 2.7(c) and (d)), with its THD optimized to 41.28%, which is still not as good as the steady-state value. The optimal 37.74% THD is obtained at the end of the 3rd optimization (Zone 6 in Fig. 2.7(d)). Notably, even if the optimal PS angles can be obtained within one round of optimization, the dynamic period T_d is always longer than the optimization period T_{opt} (180 ms), being a major limitation of the VAPS PWM method.

From the above, it is shown that the VAPS PWM method has a slow dynamic response when the optimization is solely achieved by a DSP. For operating conditions when the output voltages of individual converters frequently change (e.g., MPPT control of PV converters), the DSP-based optimization may fail to timely optimize the voltage THD. It thus calls for faster VAPS PWM methods.

2.2.2. FPGA-Enabled Computation-Efficient Method

From the above, it is challenging to further improve the optimization speed of the VAPS PWM method only with a DSP due to its limited computing capability. To

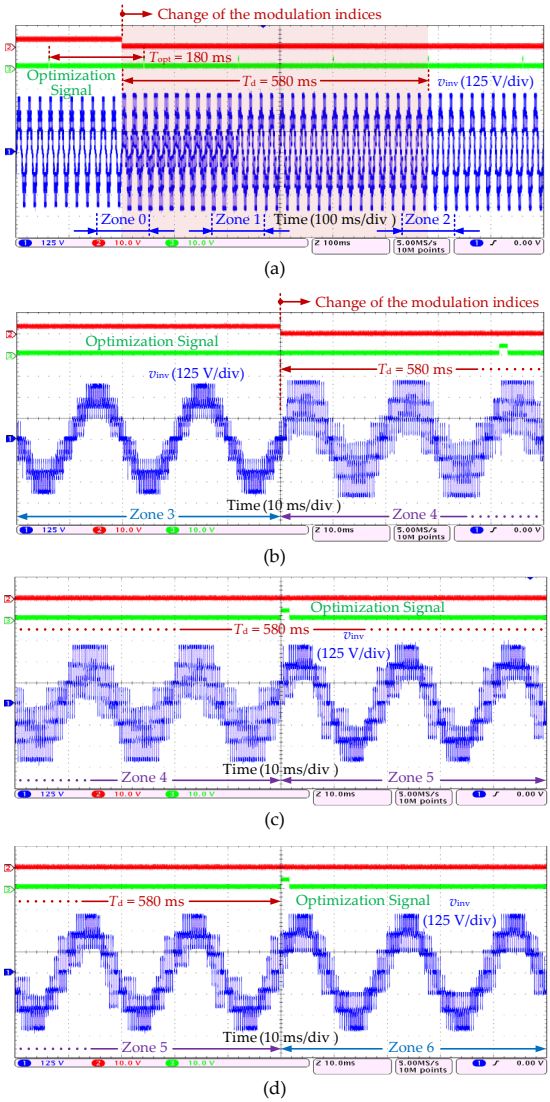

Fig. 2.7: Experimental results of Case 2 with the DSP-based VAPS PWM: (a) output multilevel voltage, and (b), (c), and (d) zoomed-in plots of Zones 0, 1, and 2 in Fig. 2.7(a). Source: [**J1**].

overcome this limitation, multicore computing approaches can be considered. The basic idea is to build a few calculation units (CUs) with additional hardware, where multiple calculations can be executed in parallel, thus improving the optimization. The schematic of the proposed FPGA-based VAPS PWM method is shown in Fig. 2.9. As it can be seen in Fig. 2.9, multiple CUs are implemented in the FPGA, which include a few harmonic calculation units (HCUs) and particle updating calculation units

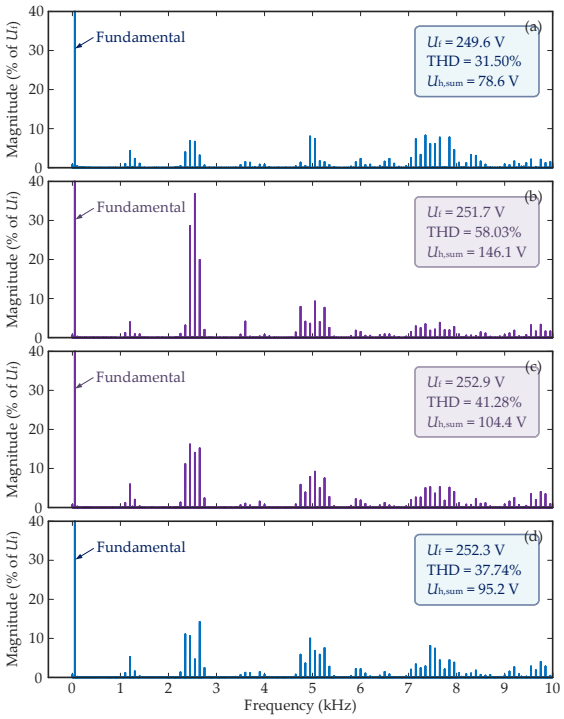

Fig. 2.8: Frequency spectra of the multilevel voltage in (a) Zone 3, (b) Zone 4, (c) Zone 5, and (d) Zone 6 of Fig. 2.7. Source: [**J1**].

(PUCUs). The HCUs are responsible for calculating $U^2_{h,sum}$ with the given U_{hkf}, $\vec{\varphi}_0$ and $\vec{\varphi}_c$ from the DSP using (2.1) and (2.2), while the PUCUs are responsible for calculating the updated position $\vec{\varphi}^{\alpha+1}_{c,\beta}$ and velocity $\vec{v}^{\alpha+1}_{\beta}$ of each particle with the given $\vec{v}^{\alpha}_{\beta}$, $\vec{\varphi}^{\alpha}_{c,\beta}$, $\vec{\varphi}^{best}_{c,\beta}$, $\vec{\varphi}^{best}_{c,g}$, $r_{1,\beta}$, and $r_{2,\beta}$ from the DSP, as illustrated in Fig. 2.9. Those variables are exchanged between the DSP and the FPGA through high-bandwidth parallel communication bus. A random-access memory (RAM) is implemented in the FPGA to provide the data buffering for the parallel communication. In this structure, the DSP is still responsible for executing the remaining part of the algorithm, e.g., initialization, logic execution, etc.

To better utilize the limited hardware resources in the FPGA, the hardware structure of HCUs is optimized, as shown in Fig. 2.10. It can be noticed that after calculating φ_{hkf}, the following calculations are processed in series. This is because the calculations of trigonometric functions and multiplications require a large amount of hardware resources. More specifically, according to (2.1), 48 CORDIC (coordinate rotation digital computer, which is used for calculating trigonometric functions) elements and 192 hardware multipliers are required if all computing is executed in parallel. Although the series computing can slow down the calculation speed, more HCUs can be implemented in FPGAs due to the reduced circuit size, enabling the parallel computing of multiple particles.

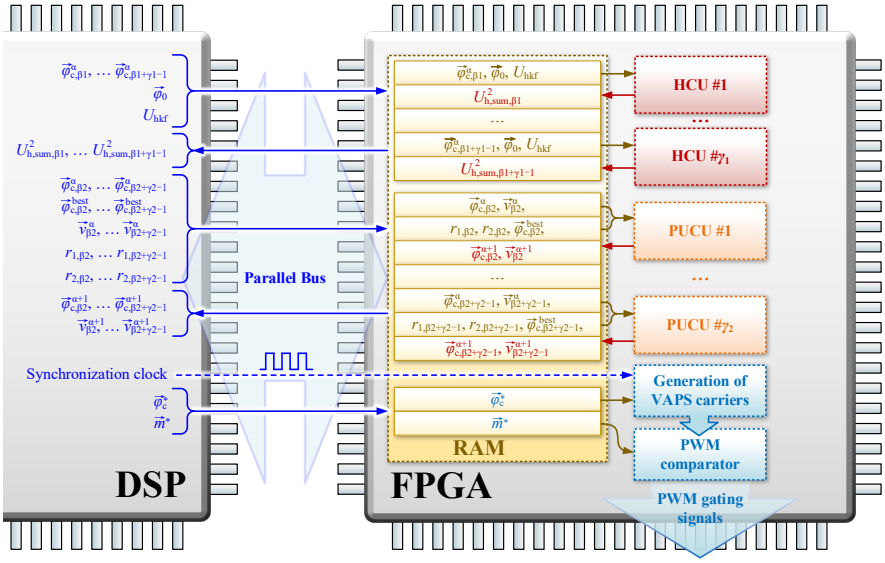

Fig. 2.9: Hardware schematic for the proposed computation-efficient VAPS PWM method, where $\vec{m}^* = [m_1^*, m_2^*, \ldots m_n^*]$ is the array of the modulation indices for all converter cells, which will be sent to the modulator in the FPGA. Source: [**J1**].

With the above approaches, the speed of the optimization algorithm can be improved from the following aspects:

1) When calculating $U_{\text{h,sum}}^2$, $\vec{\varphi}_{\text{c,}\beta}^{\alpha+1}$ and $\vec{v}_{\beta}^{\alpha+1}$ values for each particle, multiple additions and multiplications (can be replaced by shifts and additions) can be executed in parallel.
2) Multiple particles can be processed in parallel with multiple CUs.
3) The calculation speed can be further improved with higher clock frequency for the FPGA (e.g., using hardware phase locked loop (PLL) in the FPGA).

To evaluate the performance of the computation-efficient VAPS PWM method, experiments have been performed with the same test conditions as in section 3.2.1, and the results are shown in Figs. 2.11-2.14. The bus-frequency and the bus-width are 28 MB/s and 12-bit, respectively. The FPGA clock frequency is 150 MHz, being the same with as DSP. The resolution of all variables is given in Table 2.1. Firstly, compared with the results in Fig. 2.5, it takes only 18.5 ms for the proposed algorithm to obtain the optimal PS angles, which is 19.4 times faster than the conventional DSP-based method. The THD values of v_{inv} in Zones 1 and 2 of Fig. 2.11 are shown in Fig. 2.12, which are almost the same with those in Fig. 2.6(a) and (b), respectively, indicating that both methods have successfully obtained the optimal PS angles. For the test case 2 (Fig. 2.13), the THD of v_{inv} in Zones 1 and 2 is shown in Fig. 2.14, which is almost identical with that in Fig. 2.8(a) and (d), respectively. However, the required time to calculate the optimal angles is reduced from 580 ms to 28 ms, indicating a significant improvement in the optimization speed. Especially for the period where the voltage THD is

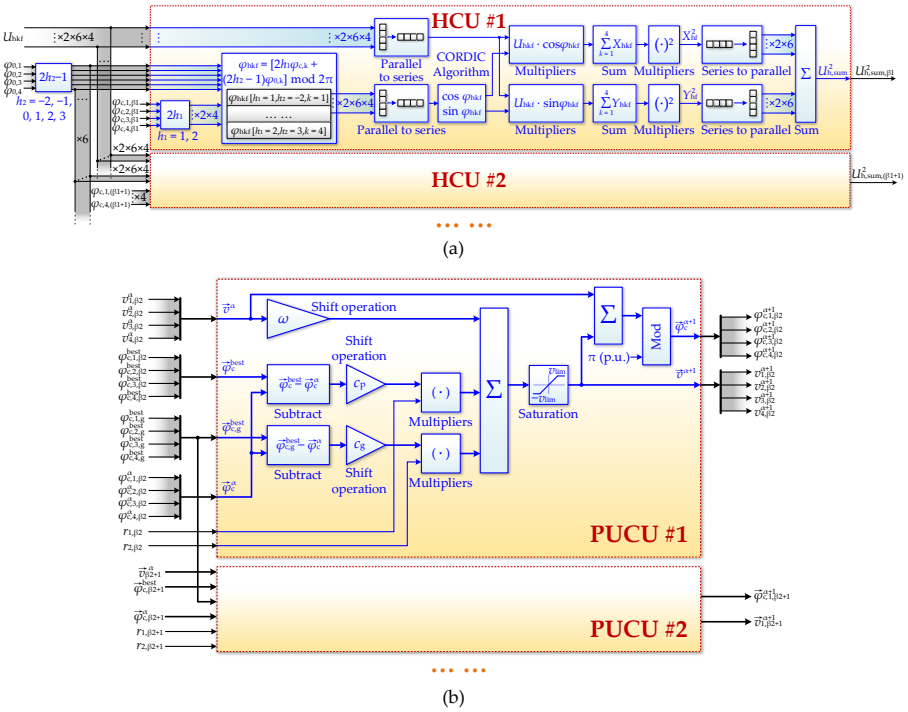

Fig. 2.10: Hardware structures of the CUs in the FPGA: (a) harmonic calculation units (HCUs) and (b) particle updating calculation units (PUCUs). Source: [**J1**].

significantly degraded (Zone 3 in Fig. 2.12), it only lasts for less than one fundamental cycle, while it was a period of 11 fundamental cycles in Fig. 2.7 (Zone 4). Thus, with the acceleration of FPGAs, the dynamic response of the VAPS PWM method can be significantly improved.

2.3. Performance Comparisons

2.3.1. Evaluation of Required Hardware Resources

In terms of the execution time for the optimization, three cases of the hardware-based method are compared with the conventional DSP-based approach, as shown in Fig. 2.15. According to Fig. 2.15(a), for one round of iteration with 100 particles, the calculation speed can be accelerated 9.0 times faster than the DSP-based method using 1 HCU in the FPGA. The most time-consuming part in the optimization is the calculation of $U^2_{\mathrm{h,sum}}$ which takes 93% of the total time for the DSP-based method. In the proposed method, this part can be significantly accelerated by the parallel computing. Although the calculation of $U^2_{\mathrm{h,sum}}$ remains the most time-consuming part in the optimization after the acceleration, it only accounts for 43% of the total time,

Table 2.1: Operational precision for variables in HCUs and PUCUs. Source: [**J1**].

Variables	Sign bit	Integer bits	Decimal bits
U_{hkf}	1	12	12
φ_{hkf} (p.u.)	0	1	8
$\cos(\varphi_{hkf})$ and $\sin(\varphi_{hkf})$	1	1	8
$U_{hkf}\cos(\varphi_{hkf})$ and $U_{hkf}\sin(\varphi_{hkf})$	1	10	18
ΣX_{hkf} and ΣY_{hkf}	1	10	10
X_{hf}^2 and Y_{hf}^2	0	20	20
$U_{h,sum}^2$	0	20	4
$\varphi_{c,k}^{\alpha}$, $\varphi_{c,k}^{best}$ and $\varphi_{c,kg}^{best}$ (p.u.)	0	1	8
v_k^{α} (p.u.)	1	0	8
r_1 and r_2	0	0	9

*subscript "k" is the converter index.

being only 0.86 ms to calculate $U_{h,sum}^2$ for 100 particles. On the other hand, although the calculation of $\vec{\varphi}_{c,\beta}^{\alpha+1}$ and $\vec{v}_{\beta}^{\alpha+1}$ is more simple than that of $U_{h,sum}^2$, it still takes 34% of the total time (0.68 ms) for the DSP to calculate the updated positions and velocities. This part of calculation can be accelerated by adding 1 PUCU in the FPGA, with which the total time is reduced to 1.57 ms, being 11.4 times faster than the DSP-based method. The time for calculating all $\vec{\varphi}_{c,\beta}^{\alpha+1}$ and $\vec{v}_{\beta}^{\alpha+1}$ values is reduced to 0.27 ms (17% of the total time, including the time for manipulating the parallel bus). When 4 HCUs and 1 PUCU are equipped, the calculation speed can be further accelerated 19.3 times faster than the DSP-based method. However, compared to the case with 1 HCU, the improvements of the 4-HCU approach is not very significant, being only 1.7 times faster. This is because the manipulation of the parallel bus as well as other codes in the DSP (e.g., logic execution) have become the most time-consuming parts in the entire algorithm, being 33% and 37% of the total time, respectively, while the calculations which are accelerated by FPGAs only account for 29% of the total time. This indicates that the improvements will become minor when more CUs are equipped, because the communication between the DSP and the FPGA will be the bottleneck in the optimization speed.

On the other hand, the acceleration process is also limited by hardware resources. The hardware requirements for different parts of the optimization are shown in Fig. 2.16. For the control system shown in Fig. 2.3 with 2 EP4CE10 FPGAs, the maximum of 4 HCUs and 1 PUCU can be achieved. More specifically, since each FPGA only has 10320 LEs and 23 hardware multipliers (18×18 bits), it takes 98% of the total logic elements (LEs) for FPGA #1 (including a RAM, 2 BCUs and the VAPS PWM circuits) and 99% of the total LEs for FPGA #2 (including a RAM, 2 BCUs and 1 PUCU). To further accelerate the optimization speed, efforts should be made considering the following aspects:

1) In the control system shown in Fig. 2.3, only the lower 12 bits of parallel data bus are connected between the DSP and FPGAs. A bus with wider bus-width can be employed to reduce the time spent on the communication, e.g., a maximum 32-bit data bus.
2) Apart from the implementation of a few CUs, the rest of the optimization can be incorporated in the FPGA. More specifically, for the proposed method, the

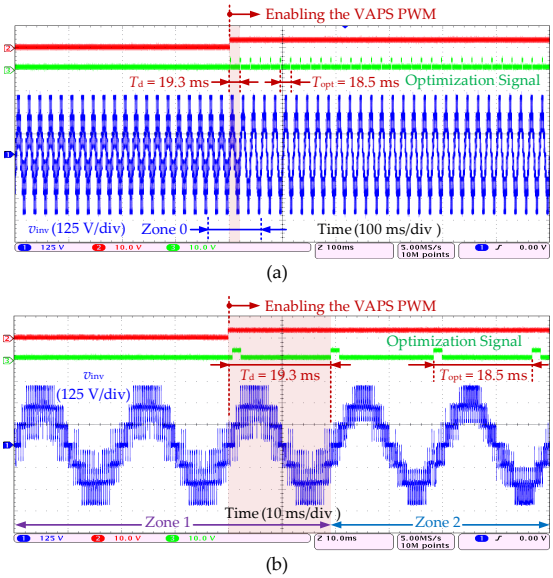

Fig. 2.11: Experimental results of Case 1 using the proposed computation-efficient VAPS PWM method: (a) output multilevel voltage, and (b) zoomed-in plot of Zone 0 in Fig. 2.11(a). Source: **[J1]**.

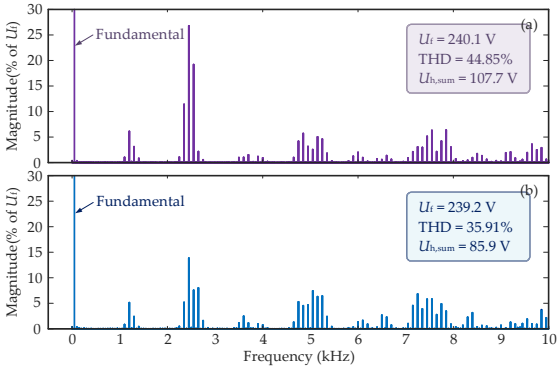

Fig. 2.12: Frequency spectra of the multilevel voltage in (a) Zone 1, and (b) Zone 2 of Fig. 2.11(b). Source: **[J1]**.

DSP is still responsible for executing the optimization algorithm. If the entire optimization algorithm can be solely achieved by the FPGA, the time spent on the communication between the FPGA and the DSP (33% of the total time in Fig. 2.15(e)), as well as the logic execution of the optimization algorithm (37% of the total time in Fig. 2.15(e) (Other codes)) can be further reduced.

3) Pipeline optimization of the circuits in FPGAs can further reduce the required time for the calculation.

Nevertheless, it is challenging to achieve the above-mentioned methods with the limited hardware resources of the available control system (Fig. 2.3). In other words,

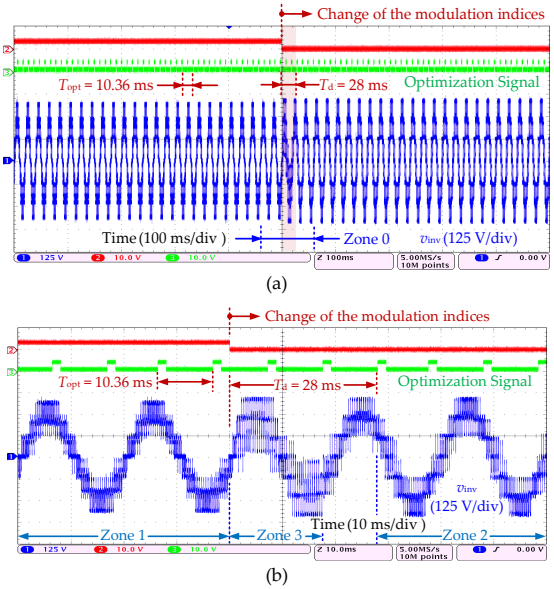

Fig. 2.13: Experimental results of Case 2 using the proposed computation-efficient VAPS PWM method: (a) output multilevel voltage, and (b) the zoomed-in plot of Zone 0 in Fig. 2.13(a). Source: [**J1**].

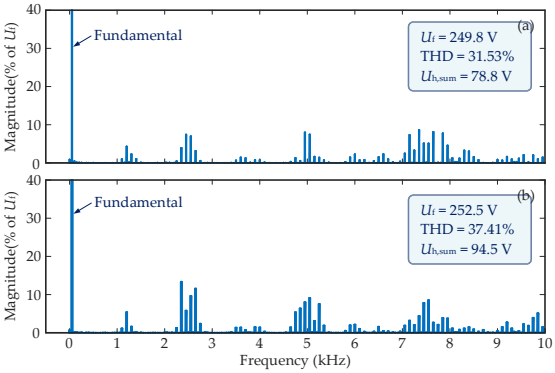

Fig. 2.14: Frequency spectra of the multilevel voltage in (a) Zone 1 and (b) Zone 2 of Fig. 2.13(b). Source: [**J1**].

the existing hardware should be upgraded to further improve the optimization speed, which will be done in the future.

2.3.2. Evaluation of *N*-cell CHB Converters

The improvements in terms of the dynamic response will be more significant for CHB converters with a higher number of cascaded cells. As it can be noticed in Fig. 2.17(a), for an optimization with 100 particles and 20 times of iteration, with the increase of the cascaded cell number, more time is required to obtain the optimal

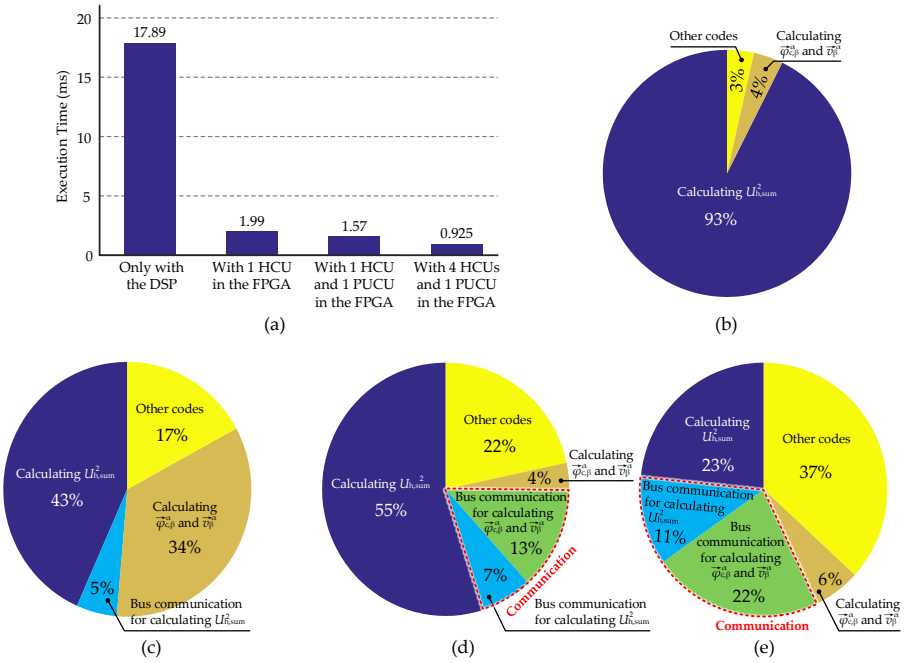

Fig. 2.15: Comparisons between the DSP-based and the FPGA-based VAPS PWM methods with 100 particles for one time of iteration: (a) time consumption for different methods, and time proportions for different parts of the optimization with (b) only the DSP, (c) with 1 HCU, (d) with 1 HCU and 1 PUCU, and (e) with 4 HCUs and 1 PUCU. Source: [**J1**].

carrier PS angles due to an increased amount of computation. When 10 cells are cascaded, the required time for the DSP-based method is 1075 ms, being 53.75 fundamental cycles. In this case, the optimization speed can be improved 24.1 times faster with the FPGA-accelerated method using 4 HCUs and 1 PUCU, being only 44.6 ms (around 2 fundamental cycles). At the same time, with the increase of the cascaded cell number, more hardware resources are required for the FPGA-accelerated approach, as it is illustrated in Fig. 2.17(b). For instance, approximately 42800 LEs and 148 hardware 9-bit multipliers are required for the 10-cell VAPS PWM method with 4 HCUs and 1 PUCU. To achieve this, the two EP4CE10 FPGAs in Fig. 2.3 should be updated by two EP4CE22 FPGAs, which have more hardware resources.

To implement the computation-efficient VAPS PWM method, the cost of the control system might be increased due to the additional hardware. However, in applications where the DSP+FPGA hardware architectures are already employed (e.g., centrally controlled systems with a large number of converter cells), the proposed computation-efficient method can be achieved by utilizing existing hardware resources. In such cases, the DSP+FPGA control architecture is employed because of the insufficient PWM resources of a single DSP (e.g., only 12 PWM channels for the TMS320F28335 DSP), and the FPGA is responsible for generating the carriers and PWM signals for all converters. Considering that the PWM generation only requires a small amount of

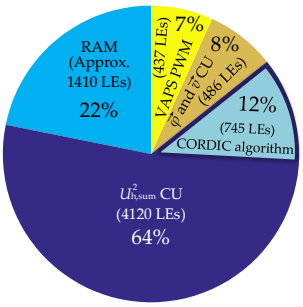

Fig. 2.16: Requirement of hardware resources for the FPGA-based VAPS PWM method with 1 HCU and 1 PUCU. Source: [**J1**].

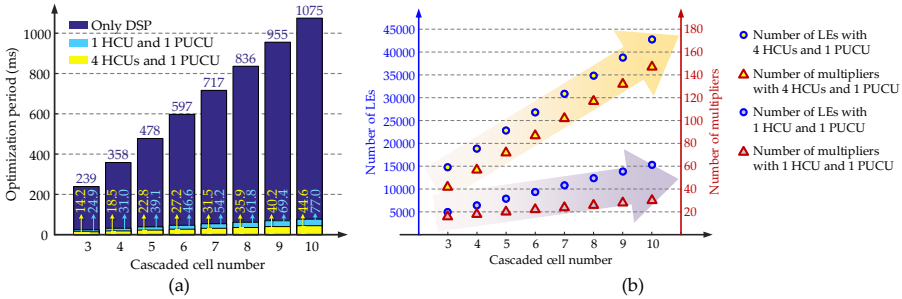

Fig. 2.17: Optimization speed and the required hardware resources for *N*-cell CHB converters with VAPS PWM method accelerated by 4 HCUs and 1 PUCU: (a) optimization period and (b) requirement of hardware resources. Source: [**J1**].

hardware resources (i.e., LEs), the remaining hardware resources of the FPGA can be used to implement the proposed method. Therefore, for such applications, the proposed hardware-based approach can be a cost-effective solution to improve the dynamic response of the high-frequency voltage harmonic optimization.

2.4. Summary

In this chapter, a computation-efficient VAPS PWM method has been proposed, which uses the FPGA-based parallel computing to reduce the time for obtaining the optimal carrier PS angles, improving the dynamic response of the VAPS PWM method. The optimization algorithm in the VAPS PWM method was accelerated from three aspects: 1) by building multiple CUs in the FPGA, multiple particles are calculated in parallel, 2) for each particle, multiple calculations are executed simultaneously, and 3) by simply improving the clock frequency of the FPGA, the calculation can be further accelerated. With the acceleration of FPGAs, the optimization speed can be improved to be at least ten times faster compared to the DSP-based optimization. The

acceleration performance was also evaluated by quantitatively analyzing 1) the consumed time for each part of the optimization algorithm and 2) the required hardware resources, while methods that can further accelerate the optimization speed were also discussed. The proposed computation-efficient VAPS PWM method can be easily applied to *N*-cell CHB converters. Experimental tests have been performed to demonstrate the effectiveness of the proposed method.

Related Publications

J1. **Y. Pan**, A. Sangwongwanich, T. Pereira, Y. Yang, M. Liserre, and F. Blaabjerg, "Computation-efficient variable angle phase-shifting PWM method for cascaded H-bridge converters," *IEEE Trans. Power Electron*., 2020. Status: to be Submitted.

Chapter 3. Interharmonic Mitigation in CHB PV Inverters

3.1. Background

As discussed in Section 1.1.2, for a single-phase CHB PV inverter shown in Fig. 3.1(a), when the DC-side oscillations due to the MPPT operation are in-phase for all inverter cells, the equivalent total voltage reference will oscillate further. Consequently, interharmonics will be amplified through the voltage / current control loops shown in Fig. 3.1(b) [**J2**], [**C1**]. To suppress interharmonics, compensation systems like energy storage systems can be employed, where the interharmonics can be suppressed through the feedback control [90], [91]. However, these approaches are not cost-effective. On the other hand, for power-electronic-interfaced systems which generate interharmonics, it is challenging to compensate for the generated interharmonics through conventional feedback control without additional hardware. This is due to the fact that the feedback control relies on the measurement of interharmonics. In that case, it requires a wide sampling window, a large amount of sampling data and computational efforts [60], [92].

However, if the main sources of interharmonics can be identified, e.g., MPPT operation for PV systems, the interharmonics can be suppressed through a control modification. Nevertheless, this approach is difficult to be achieved on one single PV inverter, where the MPPT perturbation is inevitable. On the other hand, for series-topology-based PV systems, the multi-cell configuration can provide more control flexibilities in suppressing interharmonics, e.g., through the coordinated control of each inverter cell. One potential solution is to shift the phase angles of PV voltage oscillations of different inverter cells in a way to counteract with each other, as shown in Fig. 3.2. With such approach, the oscillation on the equivalent total DC voltage will be suppressed. As a consequence, interharmonics can be suppressed as well. This is the core idea of the phase-shifting MPPT (PS-MPPT) method proposed in [**J2**], [**C1**]. In addition to the PS-MPPT, more solutions will be explored for CHB PV inverters in this chapter, e.g., the random sampling-rate MPPT, hybrid PS-MPPT, and an "interharmonic filter" method [**J2**], [**C5**], [**C3**]. All these methods will be evaluated and compared, through simulations or experimental results.

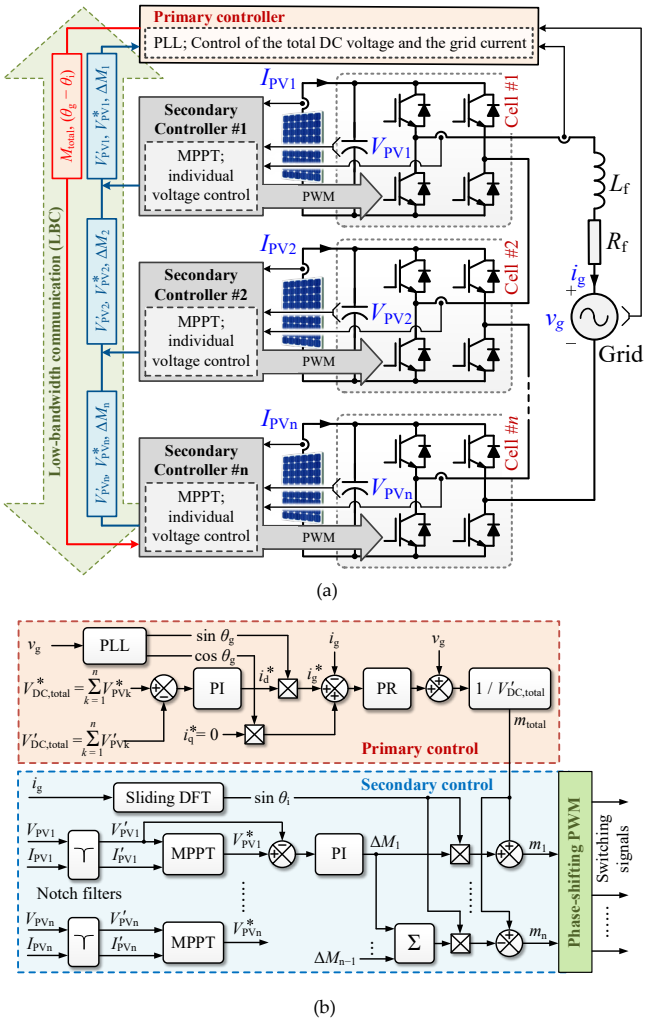

Fig. 3.1: Overall diagram of a single-phase CHB PV inverter: (a) configuration of the system with n cells, and (b) control diagram, PLL refers to the phase locked loop, DFT refers to discrete Fourier transform, PI refers to the proportional-integral regulator, θ_g and θ_i are the phase-angles of the grid voltage and current, respectively, m_{total} and m_k are the total modulation index and the modulation index for the k^{th} converter cell, respectively, and ΔM_k is the adjustment calculated by the secondary voltage controller of the k^{th} converter cell. Source: [**J2**].

3.2. Interharmonic Mitigation Methods

3.2.1. Phase-Shifting MPPT Method

The operational principle of the PS-MPPT method is to detect the phase-angles of the DC-side oscillations for individual PV inverters, and thus adjust them in a way to

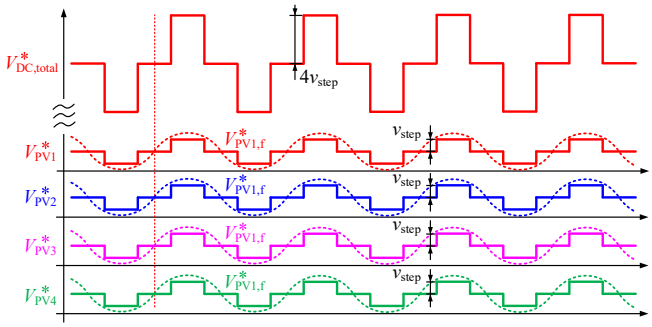

Fig. 3.2: PV voltage references of a 4-cell CHB PV inverter in steady state when the PV voltage oscillations are phase-shifted. Source: [**J2**].

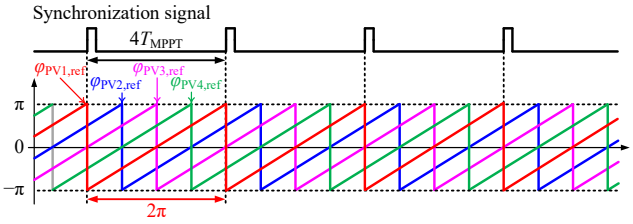

Fig. 3.3: Synchronization signal and phase-angle references $\varphi_{PV1,ref}$ – $\varphi_{PV4,ref}$ of the DC-side oscillations for a 4-cell CHB PV inverter, where T_{MPPT} is the MPPT period. Source: [**J2**].

minimize the oscillations on the total DC voltage $V^*_{DC,total}$ [**J2**]. The implementation of the PS-MPPT consists of three parts: detection, synchronization, and phase-shifting.

- **Detection:** The "detection" is to detect the phase angle of the PV voltage oscillation. It is obtained through a sliding discrete Fourier transform (SDFT) algorithm expressed as

$$A_{fund}(x+1) = e^{\frac{j\cdot 2\pi\cdot f_{fund}}{N_{SDFT}}}\left[A_{fund}(x) + V^*_{PVk}(x+N) - V^*_{PVk}(x)\right] \tag{3.1}$$

where $f_{fund} = f_{MPPT}/4$, and is the fundamental frequency of the SDFT algorithm (f_{MPPT} is the MPPT frequency), $A_{fund}(x)$ is the amplitude of the PV voltage oscillation obtained after the x^{th} transform. N_{SDFT} is the width of the sampling window for SDFT, while $V^*_{PVk}(x+N)$ is the latest sampled voltage reference. With (2.1), the phase-angle of the DC voltage oscillation for the k^{th} inverter cell can be obtained as

$$\varphi_{PVk} = \arctan\left(\mathrm{Im}\left(A_{fund}(x+1)\right)/\mathrm{Re}\left(A_{fund}(x+1)\right)\right) \tag{3.2}$$

where "Re(·)" and "Im(·)" refer to the real and imaginary part of the variable, respectively.

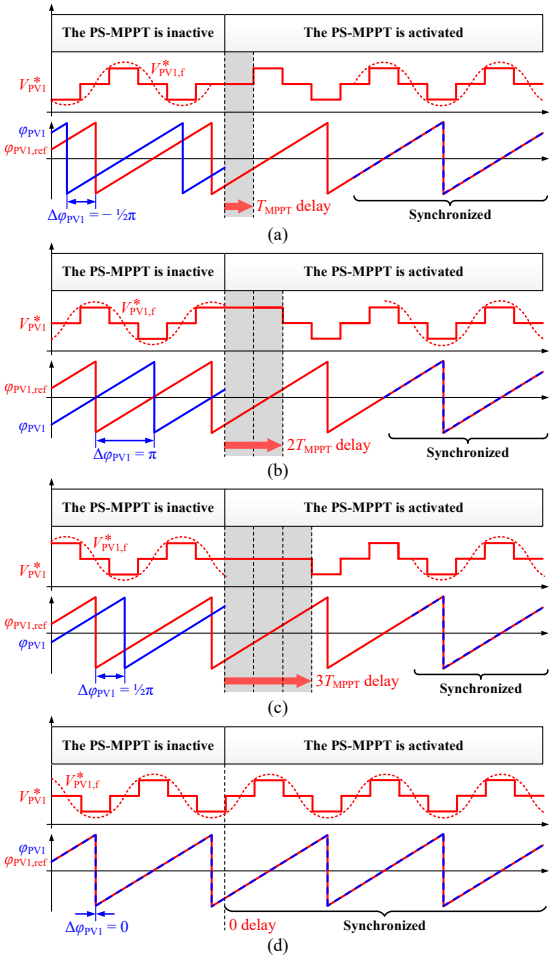

Fig. 3.4: Four cases for the PS-MPPT to insert time delays when the phase-angle difference for the 1st cell (a) $\Delta\varphi_{PV1} = -\frac{1}{2}\pi$, (b) $\Delta\varphi_{PV1} = \pi$, (c) $\Delta\varphi_{PV1} = \frac{1}{2}\pi$, and (d) $\Delta\varphi_{PV1} = 0$. Source: [**J2**].

- **Synchronization:** In order to precisely phase-shifting the PV voltage oscillations, all PV inverters are synchronized to a common clock signal, as demonstrated in Fig. 3.3, where synchronization signal appears every $4/f_{MPPT}$. With this common clock signal, the phase-angle reference of the PV voltage oscillation can be generated locally by the individual PV inverter, which is phase-shifted by a specified value with respect to the former inverter, e.g., $\pi/2$ for each in a 4-cell CHB PV inverter, as demonstrated in Fig. 3.3.
- **Phase-shifting:** If one inverter cell is operating in steady state (the phase-angle of the PV voltage oscillation remains unchanged for a few consecutive MPPT cycles), the PS control will be executed for this inverter cell. The phase-

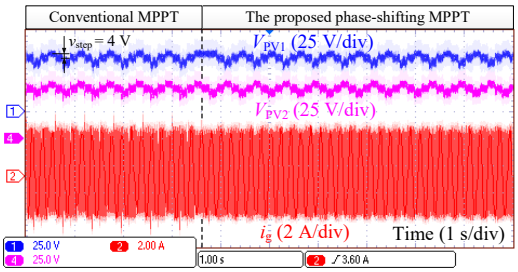

Fig. 3.5: Grid current and PV voltages of a 2-cell CHB PV inverter using the conventional and the proposed PS-MPPT methods, with the two 300-W PV panels operated at 20% of its rated power, and the grid voltage being 40 V(rms). Source: [**J2**].

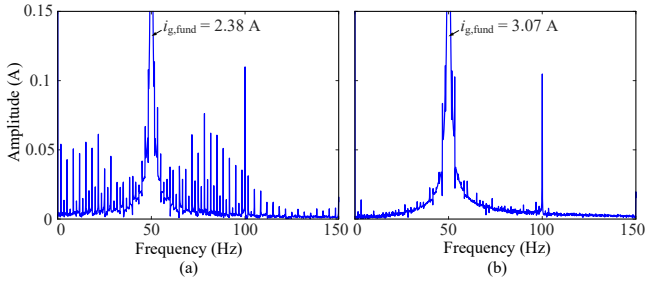

Fig. 3.6: Frequency spectra of i_g in Fig. 3.5: (a) with in-phase PV voltage oscillations, and (b) with the PS-MPPT, where $i_{g,fund}$ refer to the fundamental grid current. Source: [**J2**].

shifting control is achieved by skipping the MPPT control for a certain period of MPPT cycles, which will insert time delays to the oscillation on the PV voltage reference. According to the phase-angle difference, four different time delays can be inserted, i.e., T_{MPPT}, $2T_{MPPT}$, $3T_{MPPT}$ and 0, as demonstrated in Fig. 3.4. By doing so, the PV voltage of each inverter cell can oscillate in-phase with its phase-shifted reference $\varphi_{PVk,ref}$.

To validate the effectiveness of the PS-MPPT, experiments have been performed on a 2-cell CHB PV inverter, and the results are shown in Figs. 3.5 and 3.6. It can be noticed that the two PV voltages are oscillating in phase at the beginning, with the oscillating frequencies being 1.67 Hz. Meanwhile, periodical spikes appear on the envelope of the grid current, and interharmonics are significant, with certain dominant components being higher than 0.05 A. When the PS-MPPT is enabled, the phase angles of the two PV voltages are in opposite phases (phase-shifted by $2T_{MPPT}$), eliminating the spikes on the grid current as well as the dominant interharmonics. Thus, the amplified interharmonics due to the in-phase MPPT oscillation can be significantly mitigated with the PS-MPPT control.

In practice, various sets of PV voltage PS angles can be employed by the PS-MPPT method to minimize the total DC voltage oscillation. For instance, they can be linearly dispatched among all cells (i.e., phase-shifted by $2\pi/n$ for each cell with respect to the

Table 3.1: PV voltage phase-angle references of the PS-MPPT method for *n*-cell CHB PV inverters. Source: [**J2**].

Total number of cells / Converter index	2-cell	3-cell	4-cell	5-cell	6-cell	7-cell
Converter #1	0	0	0	0	0	0
Converter #2	π	π/2	π/2	π/2	π/2	π/2
Converter #3	/	π	π	π	π	π
Converter #4	/	/	3π /2	3π /2	3π /2	3π /2
Converter #5	/	/	/	0	0	0
Converter #6	/	/	/	/	π	π/2
Converter #7	/	/	/	/	/	π

former cell), or non-linearly dispatched, as shown in Table 3.1, where one case of non-linear dispatching (6-cell case) is given.

3.2.2. Hybrid Phase-Shifting MPPT Method

When applying the PS-MPPT to CHB PV inverters with an even cascaded number, it is possible to fully eliminate the oscillation on the total DC voltage reference. However, the total voltage oscillation, as well as interharmonics cannot be eliminated for CHB PV inverters with an odd number of cascaded converters, regardless of the applied PS angles. In this case, the oscillation amplitude of the total voltage equals to that of one inverter cell, as illustrated in Fig. 3.7, where the PV voltage references of a 3-cell inverter are exemplified. To solve this issue, a hybrid PS-MPPT method is developed in [**J2**], which is demonstrated in Fig. 3.8. It can be explained as follows: for an *n*-cell inverter (*n* is odd number), the PS-MPPT is applied to (*n*−1) converters, and the oscillation on the sum of voltage references of these (*n*−1) converters can be fully canceled. Meanwhile, the random-sampling rate MPPT is adopted for the remaining converter. By doing so, the interharmonic contents of the entire system will be similar with one inverter cell with the random sampling-rate MPPT. With such approach, the interharmonic suppression performance can be further improved for systems with an odd number of cascaded converters, compared with the case where the PS-MPPT is applied to all cells. The effectiveness of this hybrid PS-MPPT is verified by simulations on a 3-cell CHB PV inverter, as shown in Figs. 3.9 and 3.10, where the interharmonic performances of the conventional, PS-, and hybrid PS-MPPT are demonstrated.

3.2.3. Random Sampling-Rate MPPT Method

For both the PS-MPPT and the hybrid PS-MPPT methods, when part of the CHB cells are not operating in the steady-state, e.g., under varying irradiance, the PV voltage oscillations of these cells may not be properly phase-shifted. As a result, interharmonics will appear again. In addition, as the PS-MPPT is dependent on the

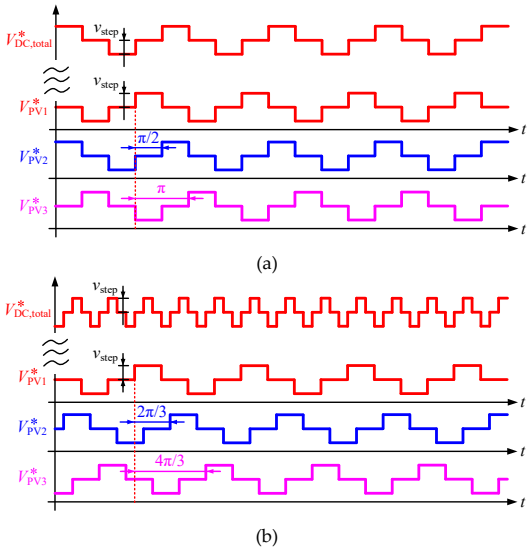

Fig. 3.7: PV voltage references for a 3-cell inverter when the PV voltage oscillations for cells #2 and #3 are phase-shifted by (a) $\pi/2$ and π, and (b) $2\pi/3$ and $4\pi/3$, respectively. Source: [**J2**].

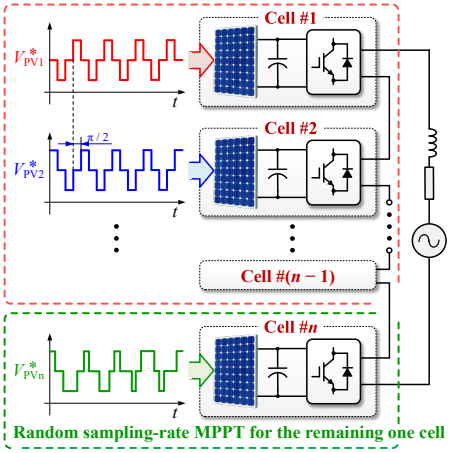

Fig. 3.8: Diagram of the hybrid PS-MPPT. Source: [**J2**].

communication to realize the MPPT synchronization of all converters, additional LBC system should be equipped for each inverter cell, making the PS-MPPT not cost-effective, especially for CHB PV system with a large number of cells. To address this issue, the random sampling-rate MPPT method can be used as an alternative solution [**C5**]. In this method, the MPPT frequency is randomly selected for each inverter cell, as illustrated in Fig. 3.11, and the oscillation frequency of the total voltage can thus become more arbitrary. Consequently, interharmonics will be distributed among a

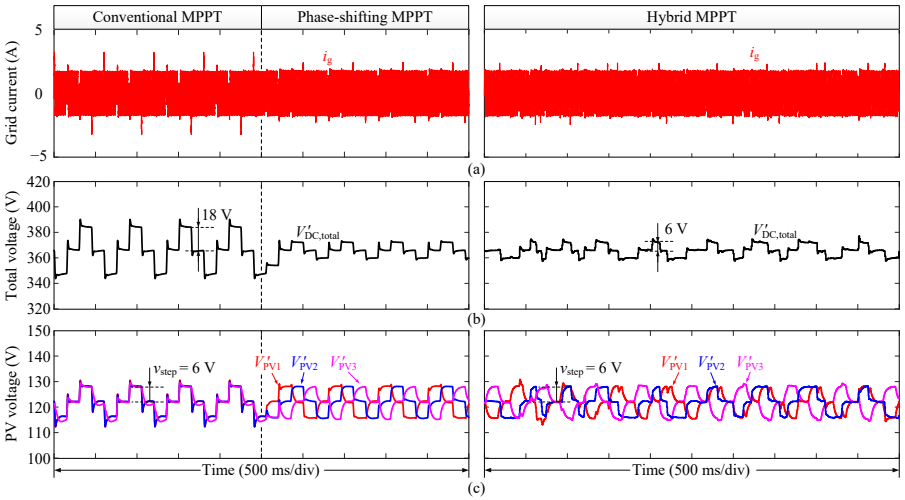

Fig. 3.9: Grid current and PV voltages of a 3-cell CHB PV converter operated at 10% of its rated power with the conventional, PS-, and hybrid PS-MPPT: (a) grid current, (b) filtered total DC voltage, and (c) filtered DC voltages for individual converters. Source: **[J2]**.

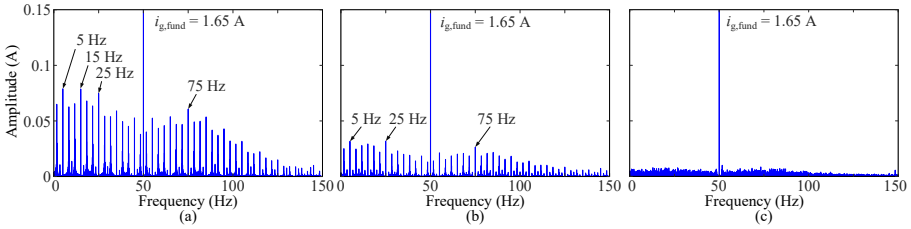

Fig. 3.10: Frequency spectra of the grid current shown in Fig. 3.9: with the (a) conventional, (b) PS-, and (c) hybrid PS-MPPT. Source: **[J2]**.

wider range of frequencies, with the amplitudes of dominant interharmonics being reduced to a large extent.

The effectiveness of the random sampling-rate MPPT is validated by simulation results as shown in Figs. 3.12 and 3.13, where the both the steady-state and dynamic performance of the random sampling-rate MPPT are compared with those of the PS-MPPT. The simulation was performed on a 4-cell CHB PV inverter. It can be noticed that although the PS-MPPT has a satisfying interharmonic performance in steady state, where the interharmonics are almost fully eliminated, interharmonics of/near the dominant frequencies appear again during the dynamic changing period. On the other hand, interharmonics can be effectively suppressed by the random sampling-rate MPPT in the same period, as shown in Fig. 3.12, where the sampling-rate of each converter cell randomly varies among any frequencies between 2 Hz to 10 Hz.

The steady-state interharmonic suppression performance of all above methods are compared in Fig. 3.14, where the total interharmonic distortion (TIHD) values for *n*-

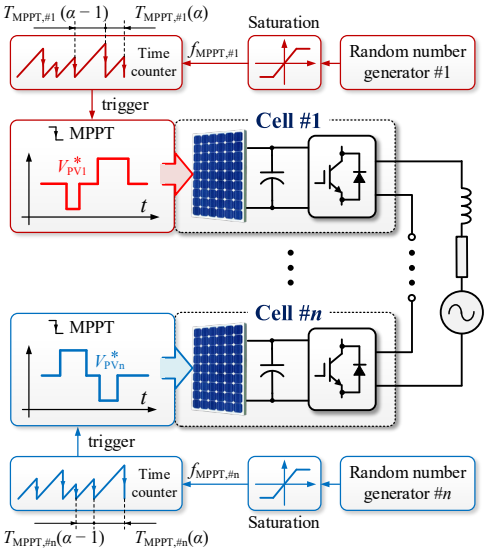

Fig. 3.11: Diagram of the random sampling-rate MPPT, where $T_{MPPT,\#k}(\alpha)$ is the MPPT period of the α^{th} MPPT cycle for cell #*k*, and the saturation units limit the upper and lower sampling-rate for the MPPT. Source: [**C2**].

cell inverters are shown. Firstly, although the interharmonics increase with the number of cascaded converters, the TIHD values for the conventional MPPT method with in-phase oscillations are almost constant. Compared with the in-phase oscillation case, the TIHD values are much smaller for the random sampling-rate MPPT method, which further decreases with the increase of the cascaded number. When the cascaded converter number is even, the PS-MPPT method with linear- and non-linear-dispatched angles have similar performance, where interharmonics are almost fully eliminated (below 0.3%). On the other hand, when the cascaded number is odd, the PS-MPPT method with non-linear dispatched angles exhibits superior interharmonic performance. In this case, even the random sampling-rate MPPT method outperforms the PS-MPPT method with linear-dispatched PV voltage PS angles. Among all these approaches, the hybrid PS-MPPT method has the best interharmonic suppression performance. Compared with the PS-MPPT method with non-linear dispatched angles, the TIHD values are almost halved for the hybrid PS-MPPT method when the cascaded number is odd.

3.2.4. Series Interharmonic Filter

Although the interharmonics can be effectively suppressed by both the PS-MPPT and random sampling-rate MPPT methods, they are compromised either in the dynamics or in the steady-state. Therefore, more efforts are expected to overcome these limitations. Considering that an additional series converter cell can be used as a harmonic filter [33], the concept of "series interharmonic filter" is developed [**C3**],

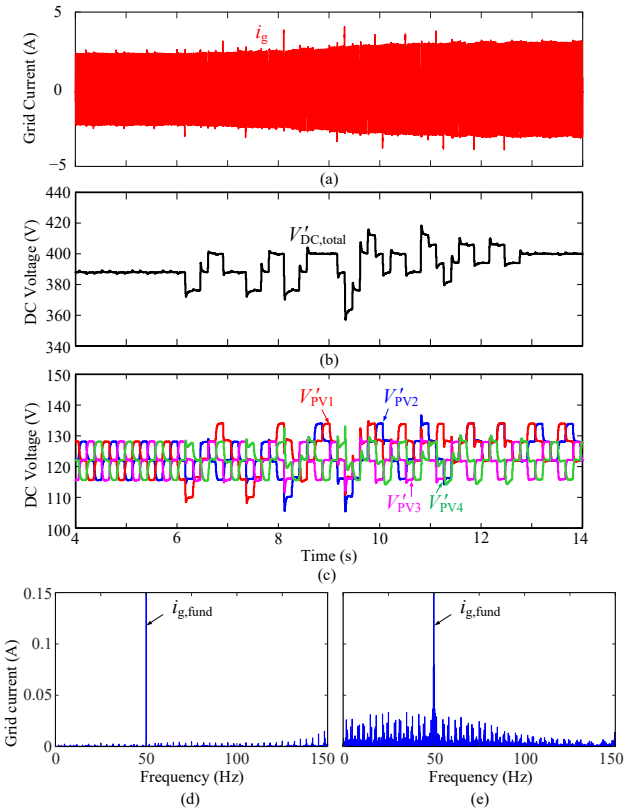

Fig. 3.12: Dynamic performance of the PS-MPPT on a 4-cell CHB PV inverter, where the power of PV #1 and #2 ramps from 10% to 15% of its rated from 6 s to 10 s and 8 s to 12 s, respectively: (a) grid current, (b) total DC voltage, (c) PV voltages of the 4 converters, (d) frequency spectrum of i_g before t = 6 s, and (e) frequency spectrum of i_g between t = 6 s to 13 s. Source: **[C2]**.

where a series converter only with capacitors in its DC-side is employed to mitigate interharmonics. The configuration of the CHB PV system with the interharmonic filter is shown in Fig. 3.15(a).

Considering that the oscillations on the total DC voltage plays a major in the generation of interharmonics, the operational principle of the interharmonic filter is to control its DC voltage in a way to cancel the oscillation on the total DC voltage of all other inverters. In this way, the total voltage can be kept constant regardless of the DC voltage oscillation of all other inverters, thus preventing the generation of interharmonics through the total voltage control loop. The control diagram of the CHB PV system with the interharmonic filter is shown in Fig. 3.15(b), where the control of the filter is achieved by collecting the modulation indices of all PV converters.

To evaluate the performance of the series interharmonic filter, experimental results on a 2-cell CHB PV inverter without and with the interharmonic filter are shown in Fig. 3.16(a) and (b), respectively. As it is shown in Fig. 3.16, the DC voltage of the filter

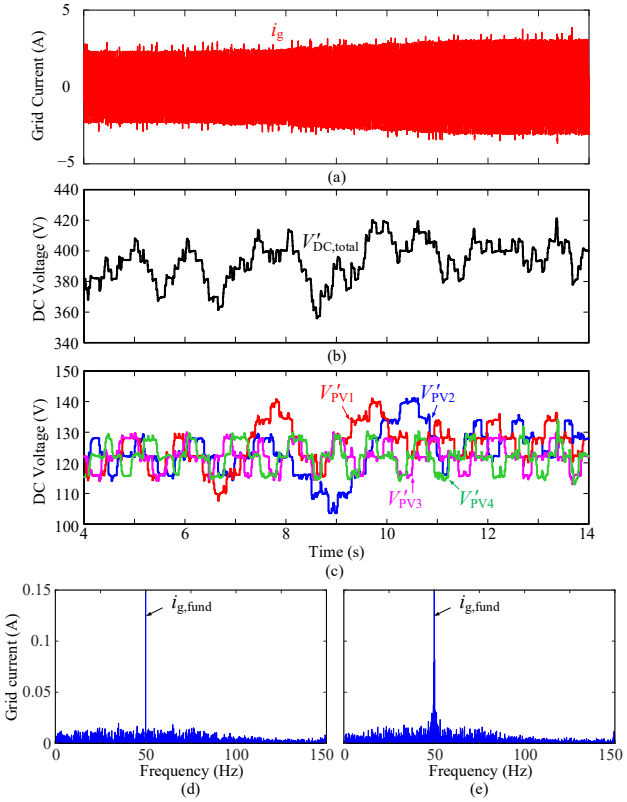

Fig. 3.13: Dynamic performance of the random sampling-rate MPPT on a 4-cell CHB PV inverter, where the simulation conditions are the same with Fig. 3.12: (a) grid current, (b) total DC voltage, (c) PV voltages of the 4 converter cells, (d) frequency spectrum of the i_g before t = 6 s, and (e) frequency spectrum of i_g between t = 6 s to 13 s. Source: **[C2]**.

cell oscillates with a reversed oscillating voltage, which cancels the in-phase oscillation of the two PV converters. Periodic spikes on the grid current are mitigated, as well as the interharmonics.

In practice, the interharmonic filter can be implemented by adding a redundant converter cell or employing one existing PV inverter, e.g., use the one with the smallest PV power. By doing so, the MPPT efficiency of this cell will only be affected a little, and in return, the interharmonic performance of the entire system can be significantly improved. Nevertheless, rather than merely operate as an interharmonic filter, the redundant/selected converter cell can also operate as a conventional harmonic filter, which is responsible for compensating low-order harmonics from either PV converters or the grid background distortion. A similar approach has been developed in [33], where the low-order harmonics can be properly distributed among all converter cells. With such an approach, the power quality performance of the CHB PV converter can also be improved.

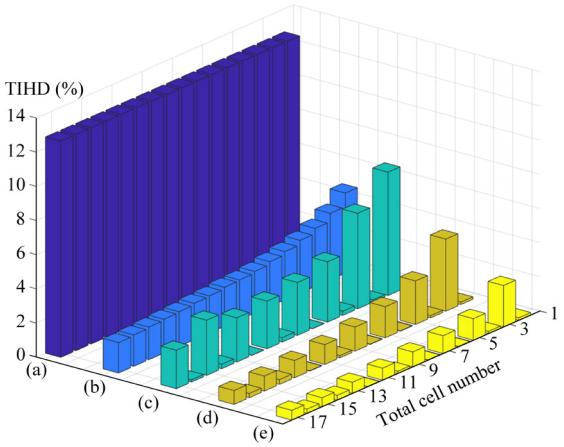

Fig. 3.14: TIHD performance of different MPPT schemes for *n*-cell inverters: (a) conventional MPPT with in-phase DC voltage oscillations, (b) random sampling-rate MPPT, (c) PS-MPPT with linearly dispatched PV voltage PS angles, (d) PS-MPPT with non-linearly dispatched PV voltage PS angles shown in Table 3.1, and (e) hybrid PS-MPPT. Source: [**J2**].

Although the oscillations on all other converters can be compensated by the interharmonic filter, interharmonics cannot be completely eliminated because the periodical MPPT disturbances on the total voltage loop remain. More specifically, the abrupt change of individual PV voltage references will result in disturbances on the total voltage loop, which grow larger when 1) more cells are oscillating in-phase or 2) the total PV power increases [**C3**]. In addition, if all other converters are oscillating in-phase, with the increase of the cascaded cell number, the interharmonic filter should generate a reversed oscillation voltage with a higher amplitude, which will significantly increase the voltage rating of the interharmonic filter. To improve the interharmonic suppression performance, the in-phase oscillations of PV converters should also be avoided even with the involvement of the interharmonic filter. This can be achieved by the combination of both the PS-MPPT and the interharmonic filter. With the PS-MPPT, the oscillation on the total voltage can be minimized. Then, the interharmonic filter will be responsible for suppressing this minimized oscillation in both the steady states and dynamics, which fails to be eliminated by the PS-MPPT.

3.3. Summary

The interharmonic mitigation methods for CHB PV inverters were discussed in this chapter, which are achieved by a coordinated control of individual PV inverters. With the PS-MPPT method, PV voltage oscillations of all converter cells are phase-shifted to minimize the oscillation on the total DC voltage, and thereby interharmonics. The hybrid PS-MPPT method was subsequently developed to enhance the interharmonic suppression capability, where the PS-MPPT and the random sampling-rate MPPT

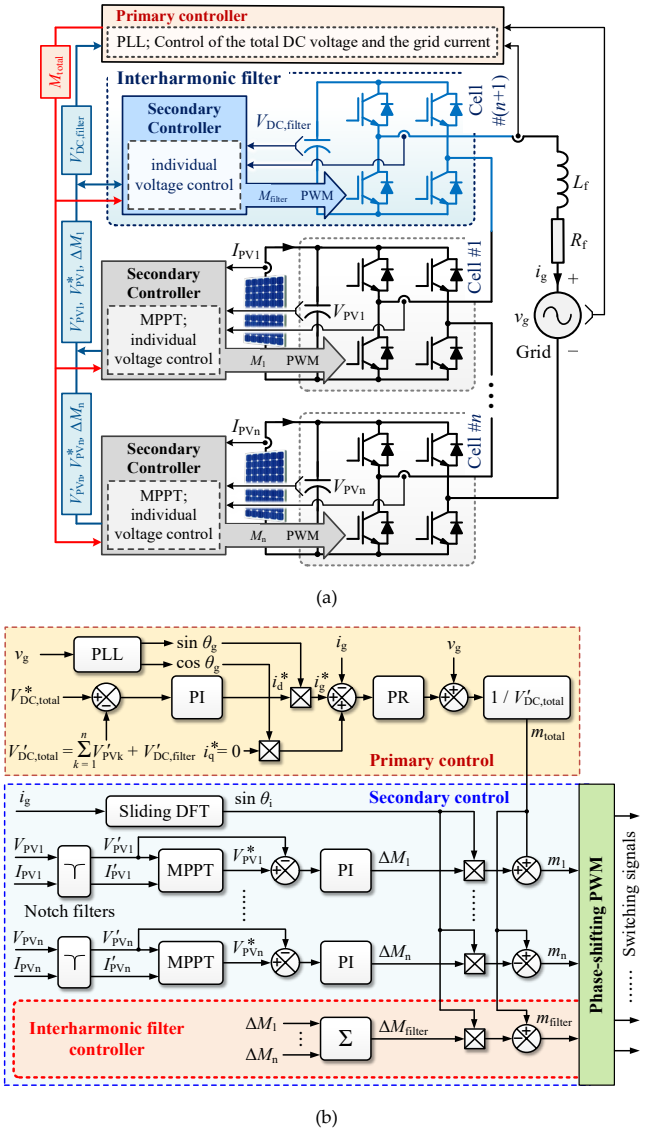

(a)

(b)

Fig. 3.15: Control diagram of a single-phase CHB PV system with a series interhamonics filter: (a) configuration of the system, and (b) control diagram, where $V_{dc,filter}$ and m_{filter} are the DC capacitor voltage and the modulation index of the interharmonic filter, respectively, and ΔM_{filter} is the modified value on the amplitude of m_{total} for the interharmonic filter. Source: **[C3]**.

methods are simultaneously applied to different converter cells. As these methods rely on the LBC, when the cascaded converter number is large, the random sampling-rate MPPT can be a more cost-effective alternative for interharmonic suppression. To address the issues that the PS-MPPT cannot ensure the interharmonic mitigation

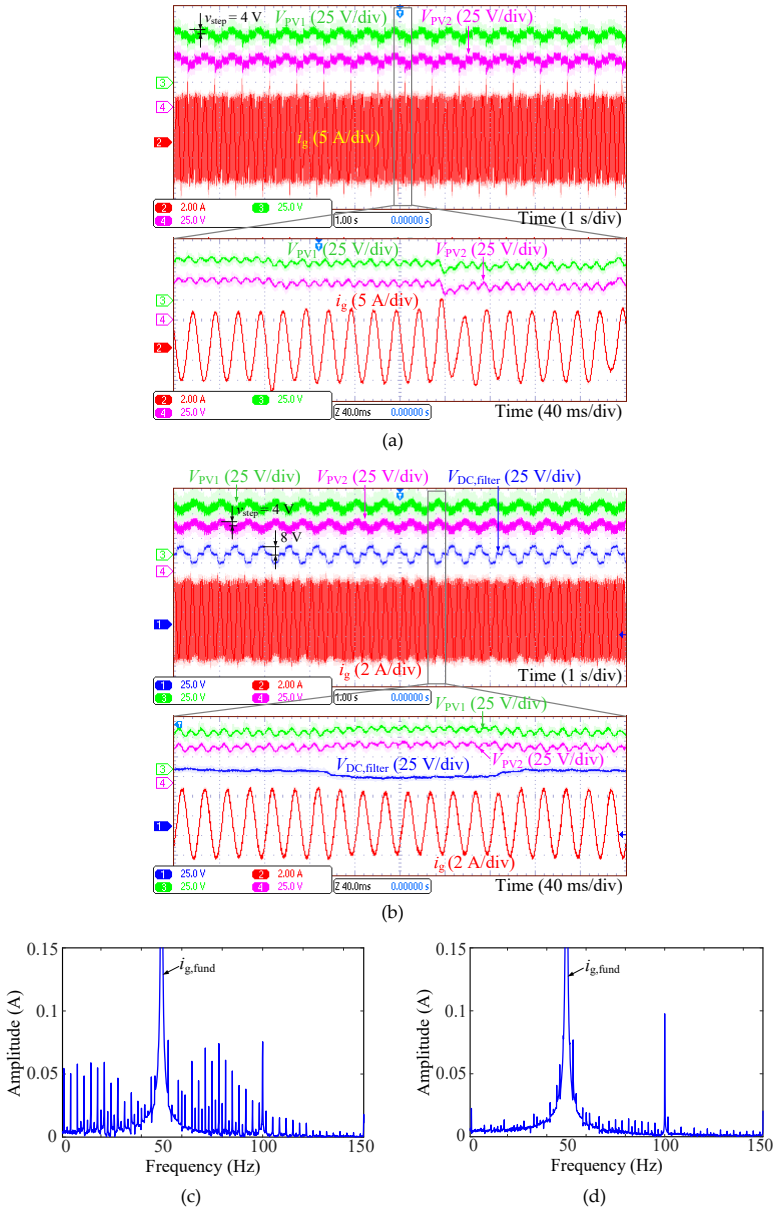

Fig. 3.16: Experimental results of a 2-cell CHB PV inverter (a) without the interharmonic filter and (b) with the interharmonic filter, where each PV converter is operated at 20% of its rated power (300 W), and the frequency spectra of the grid current in (a) and (b) are shown in (c) and (d), respectively. Source: [**C3**].

during the dynamics, while the steady-state performance of the random sampling-rate MPPT is compromised, the concept of "series interharmonic filter" was developed. By

controlling the DC voltage of one converter cell in a way to cancel the DC voltage oscillations of all other converters, the total voltage can be oscillation-free, thus eliminating the generation of interharmonics through the total voltage loop. Nevertheless, as the interharmonics can be added in hardware, or selected among existing PV converters, this method is also compromised either in cost or the MPPT efficiency. All these methods are simple to be achieved, which can be easily applied to *n*-cell inverters. The interharmonic performance of all the above-mentioned methods were evaluated through either simulations or experimental tests.

Related Publications

J2. **Y. Pan**, A. Sangwongwanich, Y. Yang, and F. Blaabjerg, "A phase-shifting MPPT to mitigate interharmonics from cascaded H-bridge PV inverters," *IEEE Trans. Ind. Appl.*, vol. 57, no. 3, pp. 3052-3063, May-Jun. 2021.

C1. **Y. Pan**, A. Sangwongwanich, Y. Yang, and F. Blaabjerg, "A phase-shifting MPPT method to mitigate interharmonics from cascaded H-bridge PV inverters," in *Proc. IEEE APEC*, 2020, pp. 157-163.

C2. **Y. Pan**, A. Sangwongwanich, Y. Yang, and F. Blaabjerg, "A random sampling-rate MPPT method to mitigate interharmonics from cascaded H-bridge photovoltaic inverters," in *Proc. IEEE IPEMC-ECCE Asia*, 2020, pp. 3252-3257.

C3. **Y. Pan**, A. Sangwongwanich, Y. Yang, and F. Blaabjerg, "A series interharmonic filter for cascaded H-bridge PV inverters," in *Proc. IEEE ECCE*, 2020, pp. 341-346.

Chapter 4.
Distributed Power Control with Low Communication Requirements

4.1. Background

To avoid the high-bandwidth communication (HBC), various distributed and decentralized control methods have been developed for series-connected systems in the literature [20]-[24], [27]-[30], [37]-[40], [66]-[71]. However, only a few are specifically designed for series-PV-battery systems [37]-[42]. As discussed in Chapter 1, these methods either highly rely on the low-bandwidth communication (LBC) with poor communication fault tolerance [37], [38], or are only applicable for certain operating conditions, e.g., unity-PF operation [40], [41], or the PFs for all converters should be the same [42]. It thus calls for the development of a more suitable distributed control method for series-PV-battery systems with less requirements on the communication. Although various distributed/decentralized control schemes for series converters have been proposed, they usually have certain limitations if adopting them for series-PV-battery systems, as listed in Table 4.1, where most of them are communication-free control methods. However, the "communication-free" is only effective under certain conditions, and the limitations are summarized as follows:

- **Effective only with equal power sharing, equal PFs, or limited PF range** [24], [28]-[30], [40]-[42], [67]-[69]. For instance, the methods in [30], [24], [40] and [41] are only suitable for unity-PF operation; the Q-ω and P-V control in [69] is only suitable for reactive load conditions (PF close to 0); and the AC voltage amplitudes for individual converters are not adjustable in [28], [29], [67] and [68], which is obviously not suitable for series-PV-battery systems, where the active and reactive power (PQ) for individual converters are variable.
- **Only considering ideal or the same kind of DC sources** [12], [13], [15], [60]-[62]**.** When different kinds of power sources are interfaced (PV panels and batteries), these methods cannot be directly applied.
- **Reactive power distribution not considered** [14], [15], [33], [34], [59]**.** As discussed in Chapter 1, the inappropriate reactive power distribution among individual converters can increase the overloading and overmodulation risks of

Table 4.1: Prior-art distributed and decentralized control methods for series-connected inverter systems. Source: [**J3**].

Ref.	DC-source types	Control architecture		Communication burden	Operating condition	Limitations when employed for series-PV-battery systems		Over-modulations
[37], [38]	PV panels and batteries	Two-layer hierarchical control		High	Grid-connected operation at any power factors (PFs)	Highly rely on the LBC; control signals should be transmitted in real-time		Only addressed for PV converters
[66]	PV panels	Distributed active and reactive power (PQ) control		Low	Grid-connected operation at any PFs	Additional grid voltage sensor for each converter; same kind of DC sources;		Not addressed
[30]	Ideal DC sources	Current-/voltage-mode (CVM) control	/	Low	Grid-connected operation at unity PF	Additional grid voltage sensor for each converter	Reactive power distribution not considered	
[24]	PV panels		/	Low		Same kind of DC sources		
[40]	PV panels and batteries		/	Low		/		
[41]	PV panels and batteries		Active power versus voltage (P-V) and PF versus angular frequency (PF-ω) control for PV converters	Communication-free		/		
[28]	Ideal DC sources	Inverse droop control			Islanding operation with resistive and inductive (RL) loads	Only suitable for RL loads	Cannot adjust the AC voltage amplitude for each converter; ideal DC sources; only equal power sharing among all converters is considered	
[67]		Frequency versus the ratio of active power to reactive power (f-P/Q) droop control			Islanding operation at quadrant I and IV	Mathematically unfeasible for pure resistive loads		
[29]		Active power versus angular frequency (P-ω) droop control			Grid-connected operation at any PFs	/		
[68]		PF droop control			Grid-connected and islanding operation	/		
[69]	DC capacitors	Reactive power versus angular frequency (Q-ω) and P-V control			Grid-connected operation with PF close to 0	Only effective when the load of all converters is reactive (PF close to 0 for all converters); Specially designed STATCOMs		
[42]	PV panels and a dispatchable source (can be batteries)	Decentralized master-slave control: droop control for the master (dispatchable) converter; PF synchronization control for slave (non-dispatchable) converters			Islanding operation at quadrant I and IV	Poor PV power utilization when the PF of the entire series system is small	Overloading risk of the dispatchable converter; reactive power distribution not considered	
[93]						/		
[94]	Batteries	Cascaded two-layer control: droop control for the system and inverse droop control for each converter cell		Low	Grid-connected and islanding operation	Rely on the central controller and the communication to calculate and transmit power references; specially developed for battery energy storage systems		

certain converters, which may result in performance degradation, or even instability of the entire system.

In fact, a few communication-free methods have been further studied in [94]-[96], where the LBC is additionally equipped. Nevertheless, as these methods are designed for other applications, e.g., battery systems, they are still not suitable for series-PV-battery systems. In addition, overmodulation is another essential issue, as discussed in Chapter 1. However, this issue has rarely been studied, as also shown in Table 4.1. Considering the above challenges, a distributed power control method is necessary, which is expected to achieve 1) the distributed/decentralized power control for individual converters regardless of their active and reactive power conditions, 2) properly distributed reactive power among all converters, 3) AOM control for all converters, and 4) low communication dependency. Therefore, a distributed control architecture for series-PV-battery systems is proposed in this chapter. Firstly, a *PQ* decoupling control is developed to achieve the power regulation of each converter at any PFs. The proposed *PQ* decoupling control is communication-free and can be realized with only local measurements. The droop control is employed for the battery converter, which automatically compensates the power difference between the PV power and the load demand, involving the entire system in the voltage and frequency regulation of the islanded grid. Then, reactive power distribution strategies are discussed with the aim to distribute the reactive power and balance the loading among individual converters. Subsequently, AOM control strategies for the PV and battery converters are respectively proposed, ensuring a stable operation of the system under 1) light load and 2) low PF conditions. All the above functions can be achieved with low requirements of the LBC. Experiments have been performed to validate the effectiveness of the proposed control.

4.2. Power Control and Anti-Overmodulation for Individual Converters

4.2.1. *PQ* Decoupling Control for PV Converters

In the following analysis, an n-cell system with one battery converter and (n−1) PV converters is studied. For simplicity, a 3-cell system is exemplified, as shown in Fig. 4.1, where it can be noticed that all converters have a common line current i_{line}. When the amplitude and phase angle of the output AC voltage of one converter change, its active and reactive power will be affected, as shown with the phasor diagram in Fig. 4.2. The relationship can be expressed as

$$\begin{bmatrix} \Delta P_{\text{k}} \\ \Delta Q_{\text{k}} \end{bmatrix} = I_{\text{line}} \begin{bmatrix} \cos\theta_{\text{k}} & -V_{\text{k}}\sin\theta_{\text{k}} \\ \sin\theta_{\text{k}} & V_{\text{k}}\cos\theta_{\text{k}} \end{bmatrix} \begin{bmatrix} \Delta V_{\text{k}} \\ \Delta\theta_{\text{k}} \end{bmatrix} = I_{\text{line}} A \begin{bmatrix} \Delta V_{\text{k}} \\ \Delta\theta_{\text{k}} \end{bmatrix} \tag{4.1}$$

where θ_{k} and V_{k} refer to the PF angle and amplitude of the output AC voltage of the k^{th} converter, respectively, $\Delta\theta_{\text{k}}$, ΔV_{k}, ΔP_{k} and ΔQ_{k} are the increments on θ_{k}, V_{k}, P_{k}, and

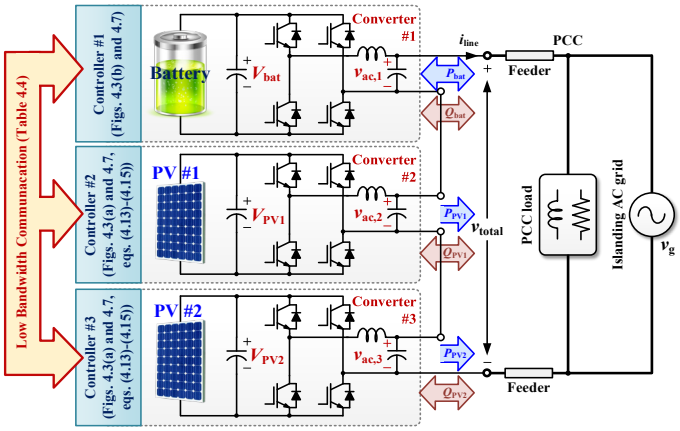

Fig. 4.1: Hardware configuration of a 3-cell series-PV-battery system, where $v_{ac,k}$ is the AC voltage of the k^{th} converter, V_{PVm} and V_{bat} are the DC voltages of PV #m and the battery, respectively, and v_{total} is the output AC voltage of the system. Source: **[J3]**, **[C4]**.

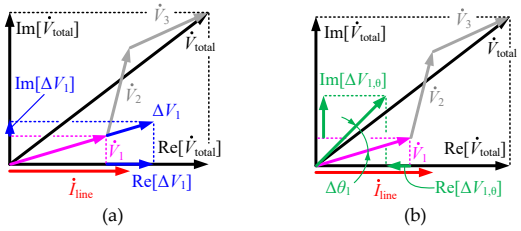

Fig. 4.2: Phasor diagram of a 3-cell series system when (a) the output voltage amplitude of the 1st converter changes (ΔV_1), and (b) the phase angle of the 1st converter changes ($\Delta\theta_1$), where $\dot{V}_k$ is the phasor of $v_{ac,k}$, Re[·] and Im[·] refer to the real and imaginary part of the variable, respectively, and $\Delta V_{1,\theta}$ refers to the increment on $\dot{V}_1$ caused by the variations of phase-angle of $\dot{V}_1$. Source: **[J3]**, **[C4]**.

Q_k respectively, and A is the coupling matrix. Clearly, there is a coupling relationship between $[\Delta P_k, \Delta Q_k]^T$ and $[\Delta V_k, \Delta\theta_k]^T$, which is also dependent on the static PF and voltage of the k^{th} converter. Reformatting (4.1), it gives

$$\begin{bmatrix}\Delta V_k \\ \Delta\theta_k\end{bmatrix} = \frac{A^{-1}}{I_{line}}\begin{bmatrix}\Delta P_k \\ \Delta Q_k\end{bmatrix} = \frac{1}{I_{line}}\begin{bmatrix}\cos\theta_k & \sin\theta_k \\ -\dfrac{\sin\theta_k}{V_k} & \dfrac{\cos\theta_k}{V_k}\end{bmatrix}\begin{bmatrix}\Delta P_k \\ \Delta Q_k\end{bmatrix} \tag{4.2}$$

where A^{-1} is the decoupling matrix. According to (4.2), the control diagram of distributed PV converters can be designed, as given in Fig. 4.3(a), where the PQ of each converter is controlled by PI regulators, with the active power reference obtained from the MPPT controller. The outputs of the two PI regulators are then decoupled by A^{-1}, and the voltage reference of each converter can be obtained. Afterwards, through the voltage and current dual-loop control, the PQ regulation of each converter can be achieved regardless of its static PF using only local measurements. As the output

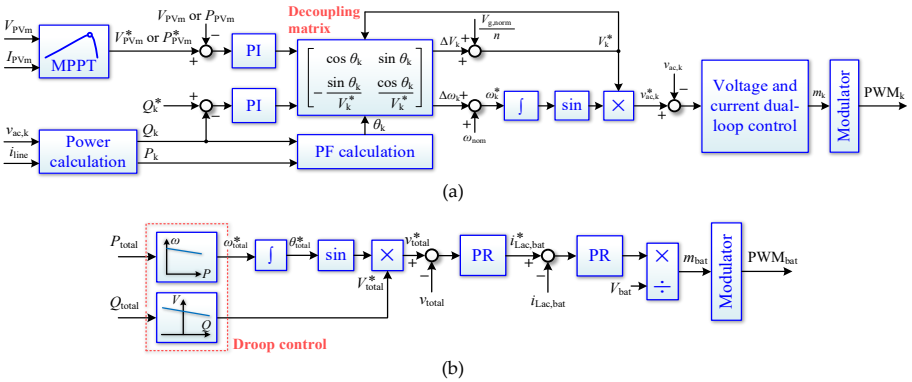

Fig. 4.3: Control diagrams of (a) the distributed PV converter and (b) the battery converter. The subscript "PVm" indicates PV #*m*, and the superscript "*" indicates that the variable is a control reference. I_{PVm}, and P_{PVm} are the PV current and active power of the m^{th} PV panel, respectively, $V_{g,nom}$, ω_{nom}, ω_k, $\Delta\omega_k$ are the amplitude of the nominal grid voltage, the nominal grid angular frequency, the angular frequency of the k^{th} converter, and the increment on ω_k, respectively, θ^*_{total} is the phase angle of the entire system, $v_{ac,k}$ is the AC voltage of the k^{th} converter, $i_{Lac,bat}$ is the filter inductor current of the battery converter, m_k and PWM_k are the modulation index and PWM signals of the k^{th} converter, respectively, m_{bat} and PWM_{bat} are the modulation index and PWM signals of the battery converter, respectively, and PR refers to the proportional-resonant regulator. Source: **[J3]**, **[C4]**.

frequency of each converter is generated locally, all distributed converters can be self-synchronized without any communication.

4.2.2. Droop Control for the Battery Converter

The conventional droop control is adopted for the battery converter to enable the participation of the series system in the voltage and frequency regulation of the islanded grid, and the control diagram is shown in Fig. 4.3(b). According to the droop curve, the frequency and total voltage reference of the series system is generated, which is subsequently regulated by the voltage and current dual-loop control of the battery converter. By doing so, the entire system will behave as a voltage source with a droop characteristic, while the power difference between the grid load and the PV power generation is automatically compensated by the battery.

4.2.3. Stability Analysis

To analyze the stability performance of the system under the above distributed control scheme and tune the control parameters, a small signal model has been derived in **[J3]**, where the tracking errors of the inner voltage/current loops have not been considered for simplification. The model is detailed in the following.

According to the control diagram in Fig. 4.3(a), for the k^{th} converter, it satisfies

$$\begin{bmatrix} \Delta V_k \\ \Delta\theta_k \end{bmatrix} = \begin{bmatrix} G_{11,k} & G_{12,k} \\ G_{21,k} & G_{22,k} \end{bmatrix} \begin{bmatrix} \Delta P_k \\ \Delta Q_k \end{bmatrix} \tag{4.3}$$

in which $G_{11,k}=-\left(k_{p,p}+k_{i,p}/s\right)\cos\theta_k$, $G_{12,k}=-\left(k_{p,q}+k_{i,q}/s\right)\sin\theta_k$, $G_{21,k}=\left(k_{p,p}+k_{i,p}/s\right)\sin\theta_k/sV_k$, and $G_{22,k}=-\left(k_{p,q}+k_{i,q}/s\right)\cos\theta_k/sV_k$. Here, $k_{p,P}$, $k_{i,P}$, $k_{P,q}$, and $k_{i,q}$ are the proportional and integral gains for the *PQ* control loops, respectively. The *PQ* of each converter can be expressed as

$$\begin{aligned}P_k+jQ_k&=V_k e^{j\theta_k}\left[\left(V_{total}e^{j\theta_{total}}-V_g e^{j0}\right)/\left|Z_f\right|e^{j\theta_f}\right]^*\\&=\frac{V_k}{\left|Z_f\right|}\left[V_{total}\cos\left(\theta_k-\theta_{total}+\theta_f\right)-V_g\cos\left(\theta_k+\theta_f\right)\right]\\&+j\frac{V_k}{\left|Z_f\right|}\left[V_{total}\sin\left(\theta_k-\theta_{total}+\theta_f\right)-V_g\sin\left(\theta_k+\theta_f\right)\right]\end{aligned}\tag{4.4}$$

where $|Z_f|$ and θ_f are the amplitude and phase-angle of the line impedance, respectively. Accordingly, ΔP_k and ΔQ_k can be calculated by

$$\begin{bmatrix}\Delta P_k\\ \Delta Q_k\end{bmatrix}=G_{LPFk}(s)\begin{bmatrix}a_{P1,k}&a_{P2,k}&a_{P3,k}&a_{P4,k}\\a_{Q1,k}&a_{Q2,k}&a_{Q3,k}&a_{Q4,k}\end{bmatrix}\begin{bmatrix}\Delta E_k&\Delta\theta_k&\Delta V_{total}&\Delta\theta_{total}\end{bmatrix}^T.\tag{4.5}$$

Here, $G_{LPFk}(s)$ is the equivalent low-pass filter (LPF) due to the power measurement, and the other coefficients are expressed as

$$\begin{bmatrix}a_{P1,k}\\a_{P2,k}\\a_{P3,k}\\a_{P4,k}\\a_{Q1,k}\\a_{Q2,k}\\a_{Q3,k}\\a_{Q4,k}\end{bmatrix}=\frac{1}{\left|Z_f\right|}\begin{bmatrix}V_{total}\cos\left(\theta_k-\theta_{total}+\theta_f\right)-V_g\cos\left(\theta_k+\theta_f\right)\\V_k\left[-V_{total}\sin\left(\theta_k-\theta_{total}+\theta_f\right)+V_g\sin\left(\theta_k+\theta_f\right)\right]\\V_k\cos\left(\theta_k-\theta_{total}+\theta_f\right)\\V_kV_{total}\sin\left(\theta_k-\theta_{total}+\theta_f\right)\\V_{total}\sin\left(\theta_k-\theta_{total}+\theta_f\right)-V_g\sin\left(\theta_k+\theta_f\right)\\V_k\left[V_{total}\cos\left(\theta_k-\theta_{total}+\theta_f\right)-V_g\cos\left(\theta_k+\theta_f\right)\right]\\V_k\sin\left(\theta_k-\theta_{total}+\theta_f\right)\\-V_kV_{total}\cos\left(\theta_k-\theta_{total}+\theta_f\right)\end{bmatrix}.\tag{4.6}$$

Secondly, according to Fig. 4.3(b), the variations on the amplitude and frequency of the total output voltage can be expressed as

$$\begin{cases}\Delta V_{total}=-\Delta Q_{total}k_{D,q}\\\Delta\theta_{total}=\dfrac{\Delta\omega_{total}}{s}=-\Delta P_{total}k_{D,P}\dfrac{1}{s}\end{cases}\tag{4.7}$$

where $k_{D,P}$ and $k_{D,q}$ are the droop coefficients. The total apparent power of the system is obtained as

$$\begin{aligned}P_{total}+jQ_{total}&=V_{total}e^{j\theta_{total}}\left[\left(V_{total}e^{j\theta_{total}}-V_g e^{j0}\right)/\left(\left|Z_f\right|e^{j\theta_f}\right)\right]^*\\&=\left[V_{total}^2\cos\theta_f-V_{total}V_g\cos\left(\theta_{total}+\theta_f\right)\right]/\left|Z_f\right|\\&+j\left[V_{total}^2\sin\theta_f-V_{total}V_g\sin\left(\theta_{total}+\theta_f\right)\right]/\left|Z_f\right|\end{aligned}.\tag{4.8}$$

With (4.7) and (4.8), the variations on the measured total *PQ* can be written as

$$\begin{bmatrix}\Delta P_{\text{total}}\\ \Delta Q_{\text{total}}\end{bmatrix}=\frac{G_{\text{LPF,total}}(s)}{|Z_{\text{f}}|}\cdot\begin{bmatrix}2V_{\text{total}}\cos\theta_{\text{f}}-V_{\text{g}}\cos(\theta_{\text{total}}+\theta_{\text{f}}) & V_{\text{total}}V_{\text{g}}\sin(\theta_{\text{total}}+\theta_{\text{f}})\\ 2V_{\text{total}}\sin\theta_{\text{f}}-V_{\text{g}}\sin(\theta_{\text{total}}+\theta_{\text{f}}) & -V_{\text{total}}V_{\text{g}}\cos(\theta_{\text{total}}+\theta_{\text{f}})\end{bmatrix}\begin{bmatrix}\Delta V_{\text{total}}\\ \Delta\theta_{\text{total}}\end{bmatrix}. \quad (4.9)$$

in which $G_{\text{LPF,total}}(s)$ is the LPF in the droop control. Then, with (4.5)-(4.7) and (4.9), the small signal model of the closed-loop controlled series system can be described as

$$\begin{bmatrix}b_{1,1} & b_{1,2} & \cdots & 0 & 0 & b_{1,2n-1} & b_{1,2n}\\ b_{2,1} & b_{2,2} & \cdots & 0 & 0 & b_{2,2n-1} & b_{2,2n}\\ \vdots & \vdots & \ddots & \vdots & \vdots & \vdots & \vdots\\ 0 & 0 & \cdots & b_{2n-3,2n-3} & b_{2n-3,2n-2} & b_{2n-3,2n-1} & b_{2n-3,2n}\\ 0 & 0 & \cdots & b_{2n-2,2n-3} & b_{2n-2,2n-2} & b_{2n-2,2n-1} & b_{2n-2,2n}\\ 0 & 0 & \cdots & 0 & 0 & b_{2n-1,2n-1} & b_{2n-1,2n}\\ 0 & 0 & \cdots & 0 & 0 & b_{2n,2n-1} & b_{2n,2n}\end{bmatrix}\begin{bmatrix}\Delta V_1\\ \Delta\theta_1\\ \vdots\\ \Delta V_{n-1}\\ \Delta\theta_{n-1}\\ \Delta V_{\text{total}}\\ \Delta\theta_{\text{total}}\end{bmatrix}=0\ . \quad (4.10)$$

where the coefficients except the last two rows are expressed as

$$\begin{bmatrix}b_{2k-1,2k-1}\\ b_{2k,2k-1}\\ b_{2k-1,2k}\\ b_{2k,2k}\\ b_{2k-1,n-1}\\ b_{2k,n-1}\\ b_{2k-1,2n}\\ b_{2k,2n}\end{bmatrix}=\begin{bmatrix}G_{11,k}a_{\text{P1,k}}+G_{12,k}a_{\text{Q1,k}}-1\\ G_{21,k}a_{\text{P1,k}}+G_{22,k}a_{\text{Q1,k}}\\ G_{21,k}a_{\text{P2,k}}+G_{12,k}a_{\text{Q2,k}}\\ G_{21,k}a_{\text{P2,k}}+G_{22,k}a_{\text{Q2,k}}-1\\ G_{11,k}a_{\text{P3,k}}+G_{12,k}a_{\text{Q3,k}}\\ G_{21,k}a_{\text{P3,k}}+G_{22,k}a_{\text{Q3,k}}\\ G_{11,k}a_{\text{P4,k}}+G_{12,k}a_{\text{Q4,k}}\\ G_{21,k}a_{\text{P4,k}}+G_{22,k}a_{\text{Q4,k}}\end{bmatrix}. \quad (4.11)$$

Here, the subscript "*k*" indicates that the variable is for the k^{th} converter ($k < n$). The last two rows can be obtained as

$$\begin{bmatrix}b_{2n-1,2n-1}\\ b_{2n-1,2n}\\ b_{2n,2n-1}\\ b_{2n,2n}\end{bmatrix}=\begin{bmatrix}G_{\text{LPF,total}}(s)\left[2V_{\text{total}}\cos\theta_{\text{f}}-V_{\text{g}}\cos(\theta_{\text{total}}+\theta_{\text{f}})\right]/|Z_{\text{f}}|\\ G_{\text{LPF,total}}(s)V_{\text{total}}V_{\text{g}}\sin(\theta_{\text{total}}+\theta_{\text{f}})/|Z_{\text{f}}|+s/k_{\text{D,p}}\\ G_{\text{LPF,total}}(s)\left[2V_{\text{total}}\sin\theta_{\text{f}}-V_{\text{g}}\sin(\theta_{\text{total}}+\theta_{\text{f}})\right]/|Z_{\text{f}}|+1/k_{\text{D,q}}\\ -G_{\text{LPF,total}}(s)V_{\text{total}}V_{\text{g}}\cos(\theta_{\text{total}}+\theta_{\text{f}})/|Z_{\text{f}}|\end{bmatrix}. \quad (4.12)$$

According to the small signal model in (4.10)-(4.12), the root loci of a 3-cell system with the proposed distributed control can be obtained [**J3**]. Fig. 4.4 demonstrates the root loci of the system under different control parameters of PV converters, and all parameters of the system are shown in Table 4.2.. As shown in Fig. 4.4(a), all poles of the system (13 poles in total) are on the left half plane, which means that the system is stable. Among these poles, only λ_1-λ_6 are considered in the analysis, since λ_7-λ_{13} are far from the imaginary axis. As it can be observed from Fig. 4.4(b), λ_1 and λ_2, λ_3 and λ_4, and λ_5 and λ_6 are conjugate pole pairs, respectively. With the increase of $k_{\text{p,p}}$ and $k_{\text{p,q}}$,

Table 4.2: Parameters of the 3-cell system. Source: [**J3**].

Circuit parameter	Value
Feeder impedance	$(0.02 + j0.1)\ \Omega$
Amplitude of the grid nominal voltage $V_{g,nom}$	311 V
Grid nominal angular frequency ω_{nom}	$2\pi \cdot 50$ rad/s
Steady-state AC voltage amplitudes of PV converters	$V_1 = V_2 = 103.7$ V
Steady-state phase angle of the entire system	$\theta_{total} = 0.02$ rad
Steady-state phase angles of PV converters	$\theta_1 = \theta_2 = 0.02$ rad
Control parameter	**Value**
Parameters of the power loops of PV converters	$k_{p,P} = k_{p,q} = 0.12$, $k_{i,P} = k_{i,q} = 0.4$
Cut-off angular frequency of $G_{LPFk}(s)$	$\omega_{cut,k} = 100$ rad/s
Cut-off angular frequency of $G_{LPF,total}(s)$	$\omega_{cut,total} = 50$ rad/s
f/*P* Droop coefficient $k_{D,P}$	$2\pi \cdot 10^{-5}$ rad/W
V/*Q* Droop coefficient $k_{D,q}$	0.005 V/var

λ_1 and λ_2 are moving towards the imaginary axis, and λ_3 and λ_4 are moving away from the imaginary axis, while λ_5 and λ_6 are firstly moving away and then towards the imaginary axis. It means that the stability margin of the series system can be reduced when the proportional gains of the power controllers are extreme. With the movement of λ_3-λ_6, the damping ratio of the system also changes, indicating different dynamic performance of the power control can be achieved. On the other hand, when $k_{i,P}$ and $k_{i,q}$ increase, λ_1 and λ_2 will move away from the imaginary axis, and λ_3-λ_6 will become less damped according to Fig. 4.4(c). Thus, the control parameters of the PI regulators for PV converters should be tuned considering both the stability and the damping requirements. The selection of $k_{p,P}$, $k_{p,q}$, $k_{i,P}$, and $k_{i,q}$ are shown in Table 4.2, and the operating points of the system with the selected parameters can be observed in Fig. 4.4.

Other control parameters (e.g., $k_{D,P}$, $\omega_{cut,total}$, etc.) can also be tuned with the help of the root loci obtained from (4.10)-(4.12) [**J3**]. Notably, once the control parameters are determined, the stability performance of the series system with such parameters should be evaluated under different steady-state conditions. More specifically, as it is shown in (4.12), the system stability is related to the static V_{total} and θ_{total}. Nevertheless, it is not necessary to analyze the stability performance of the system with different static V_k and θ_k, as the location of poles are not affected by the variations of V_k and θ_k. The analysis on the root loci of the system under different values of $k_{D,P}$, $\omega_{cut,total}$, V_{total} and θ_{total} is detailed in [**J3**].

4.2.4. Reactive Power Distribution

As discussed previously, the inappropriate distribution of reactive power can result in overloading or overmodulation of certain converters, which may eventually lead to stability issues. To avoid such issues, the reactive power should be distributed considering the apparent power balancing of all converters. In [**J3**], a reactive power distribution strategy has been proposed, where only the information of the total active and reactive power is received by individual converters through the LBC. With the

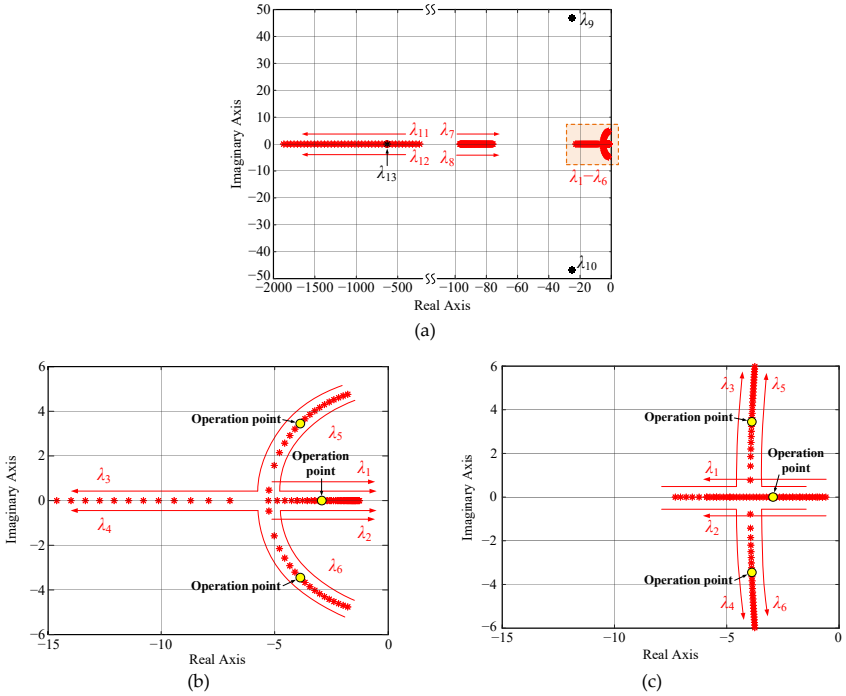

Fig. 4.4: Root loci of the islanded 3-cell system with varying control parameters of PV converters: (a) all $k_{p,P}$ and $k_{p,q}$ increase from 0.06 to 0.3, (b) zoomed-in plot of Fig. 4.4(a), and (c) root loci of the six dominant poles when all $k_{i,P}$ and $k_{i,q}$ increase from 0.08 to 0.8. Source: [**J3**].

knowledge of the total PQ, the reactive power reference of each converter can be obtained by assuming 1) the apparent power references of all converters are the same, and 2) the total voltage is maintained by all other converters with the minimum required voltage amplitude. This assumption is demonstrated in Fig. 4.5, where the assumed power are $(P_2+jQ_2)_{\min}$ and $(P_3+jQ_3)_{\min}$ for the 2nd and the 3rd converter, respectively. With the above assumption, the reactive power reference of the k^{th} converter can be obtained by solving

$$\frac{\left|P_{\text{k}}+jQ_{\text{k}}^{*}\right|}{\left|\left(P_{\text{total}}-P_{\text{k}}\right)+j\left(Q_{\text{total}}-Q_{\text{k}}^{*}\right)\right|}=\frac{1}{n-1}. \tag{4.13}$$

Accordingly, Q_{k}^{*} can be expressed as

$$Q_{\text{k}}^{*}=\begin{cases} 0, & \sigma\le 0 \\ \dfrac{\sqrt{\sigma}-Q_{\text{total}}}{n^2-2n}, & \sigma>0 \text{ and } \left|\sqrt{\sigma}-Q_{\text{total}}\right|<\left|-\sqrt{\sigma}-Q_{\text{total}}\right| \\ \dfrac{-\sqrt{\sigma}-Q_{\text{total}}}{n^2-2n}, & \sigma>0 \text{ and } \left|\sqrt{\sigma}-Q_{\text{total}}\right|>\left|-\sqrt{\sigma}-Q_{\text{total}}\right| \end{cases}, \tag{4.14}$$

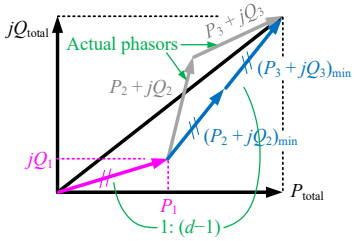

Fig. 4.5: Phasor diagram of the reactive power distribution. Source: [**J3**], [**C4**].

with

$$\sigma = Q_{\text{total}}^2 - \left(n^2 - 2n\right)\left[\left(n-1\right)^2 P_{\text{k}}^2 - \left(P_{\text{total}} - P_{\text{k}}\right)^2 - Q_{\text{k}}^2\right]. \tag{4.15}$$

where Q_{k}^* should be limited within the range of [0, Q_{total}] to avoid generating excessive and reversed reactive power. However, the values of the actual output voltages of other converters are usually not the assumed minimum values. Instead, the actual output voltages are usually larger, as shown in Fig. 4.5. Thus, the control equations in (4.14) and (4.15) can result in less reactive power contribution from PV converters, and at the same time, the battery converter is under higher risk of overloading. To address this issue, the integer n in (4.14) and (4.15) can be replaced by a non-integer d, being an adjustable coefficient for the reactive power distribution. If d is selected smaller than n, PV converters can generate more reactive power, alleviating the overloading risks of the battery converter. In practice, d can also be adjusted online to optimize the power distribution performance.

Although the reactive power distribution strategy in [**J3**] has a low communication dependency, it is still challenging to achieve optimal reactive power distribution with the strategy in [**J3**], which is based on the assumption of the operating conditions of other converters. Nevertheless, with the knowledge of the active power contribution of all other converters, it is possible to achieve an optimal reactive power distribution, as discussed in [**C5**]. According to the approach in [**C5**], the reactive power references of individual converters are obtained through mathematical searching algorithms (e.g., the PSO algorithm), which is employed to minimize the cost function g:

$$g = p_1\sqrt{\frac{1}{n}\sum_{k=1}^{n}\left(S_{\text{k}} - \overline{S}\right)^2} + p_2\sum_{k=1}^{n} S_{\text{k}}\,. \tag{4.16}$$

where S_{k} is the apparent power of the k^{th} converter, $\overline{S}$ is the average apparent power of all converters ($\overline{S} = (1/n)\sum_{k=1}^{n} S_k$), and p_1 and p_2 are two weighting factors. From (4.16), it can be noticed that the first and the second terms in the cost function are designed to minimize 1) the apparent power differences among all converters, and 2) the total apparent power contribution from all converters, respectively, for the given {P_1, … $P_{\text{n–1}}$, P_{total}, Q_{total}}. As the calculation of this optimization issue is much simpler than the harmonic optimization issue discussed in Chapter 2, it requires only 12 ms for the

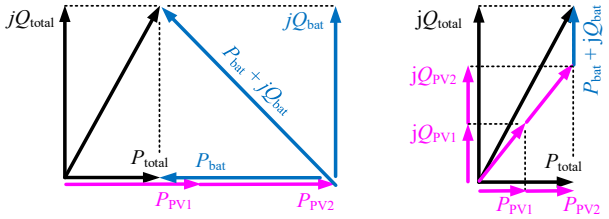

Fig. 4.6: Phasor diagram of the system when the total PF is small: (a) the battery converter is overmodulated, and (b) the battery converter is free from overmodulation with the proposed AOM loop. Source: [**J3**], [**C4**].

TMS320F28335 DSP to achieve the optimization with 100 particles and 200 iterations [**C5**], which is fast enough to meet the power distribution requirement. In practice, the PSO-based reactive power distribution algorithm can be executed by any one of the local controllers, which should collect the active power information of all converters, and dispatch the calculated reactive power reference to each converter through the LBC. Although more variables should be transmitted through the communication, the increase of the communication burden is negligible, as all transmitted data are of slow dynamics.

4.2.5. Anti-Overmodulation (AOM) Control

Overmodulation may appear on certain converters when 1) the line current i_{line} reduces, and 2) the entire system has a high reactive load [**J3**]. The first case usually leads to the overmodulation of PV converters. More specifically, when i_{line} decreases as the load power decreases, the output voltages of PV converters will increase to keep themselves operating at their MPPs, which could result in overmodulation. The second case will usually lead to overmodulation of the battery converter, which can be explained as follows. As shown in Fig. 4.6(a), when Q_{total} is large while P_{total} is small, PV converters can stay in the MPPT mode owing to a large i_{line}. As the PV converters already have a high loading, PV converters may only generate active power, according to the reactive power distribution strategy in (4.14). In this case, a large amount of excessive active power being (P_{PV1}+P_{PV2}–P_{total}) will be generated, which should be absorbed by the battery converter. In addition, the battery converter should also provide all reactive power, as demonstrated in Fig. 4.6(a), where the apparent power of the battery equals to (P_{total}–P_{PV1}+P_{PV2})+jQ_{total}. Such large power can easily result in overmodulation of the battery converter.

To address these issues, AOM control method is developed in [**J3**] for both the PV and battery converters. The basic idea of the AOM is to curtail the PV power generation, which is achieved by operating PV panels at a voltage higher than their MPP voltages. By doing so, 1) the modulation index of PV converters will decrease as the reduction of PV power, 2) higher DC voltages can be available for modulation, and 3) PV converters can generate more reactive power according to the control equation in (4.14), and the battery converter will absorb less active power, freeing the battery

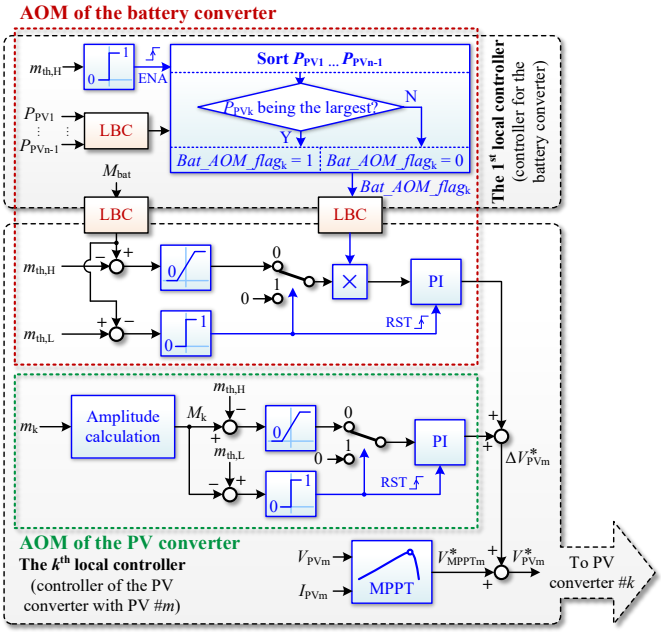

Fig. 4.7: The AOM control for both the PV and battery converters, where V^*_{MPPTm} is the PV voltage reference generated by the MPPT of PV #m, and ΔV^*_{PVm} is the total output of the two AOM loops. Source: [**J3**].

converter from overmodulation, as illustrated in Fig. 4.6(b). The diagrams of the AOM loops are shown in Fig. 4.7, where two comparison thresholds for the modulation index are introduced, i.e., the higher threshold being $m_{th,H}$ and the lower one being $m_{th,L}$. For the k^{th} PV converter, when amplitude of the modulation index M_k is higher than $m_{th,H}$, a voltage increment calculated by a PI controller will be added to the PV reference voltage. When M_k becomes lower than $m_{th,L}$, the PV converter is considered to be free from overmodulation. In this case, the AOM PI loop will be reset, enabling the MPPT operation of PV converters.

The AOM of the battery converter is achieved similarly. As shown in Fig. 4.7, a PI-controller-based AOM loop is designed, where M_{bat} (amplitude of the modulation index of the battery converter) is the input variable. All PV converters are involved in the AOM of the battery converter, but only the PV converter with the highest active power will discard part of its power. Obviously, the AOM control of the battery converter is dependent on the LBC, which collects the active power information of all converters (P_{PV1}, … P_{PVn-1}) for sorting, and sends out the AOM enabling signals *Bat_AOM_flag*s from the controller of the battery converter. Considering that all these transmitted variables are of slow dynamics, the LBC is sufficient to achieve the proposed AOM control. Overall, the architecture of the proposed LBC-based distributed control is demonstrated in Fig. 4.8, where the *PQ* decoupling control, droop control, AOM control, reactive power distribution, and all necessary communicating variables are illustrated.

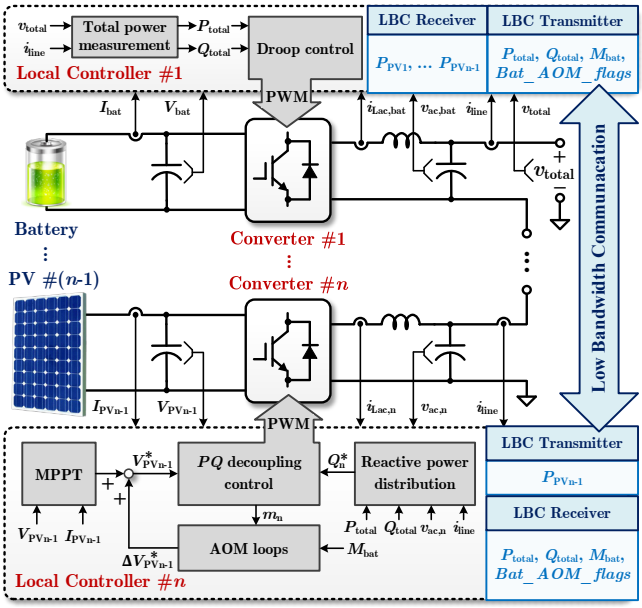

Fig. 4.8: Architecture of the proposed distributed control, where I_{bat}, $i_{Lac,n}$ and $v_{ac,bat}$ are the battery current, the filter inductor current of the n^{th} converter, and the AC voltage of the battery converter, respectively. Source: **[J3]**.

4.3. Experimental Verification

Experimental tests have been conducted on a downscaled 3-cell series-PV-battery system with two PV converters shown in Fig. 4.9. The hardware and control parameters are given in Tables 4.2 and 4.3. Three cases of experiments have been performed for validating the effectiveness of the proposed *PQ* decoupling control, AOM control and the reactive power distribution method given in (4.14):

Case 1: The first test demonstrates the active power step response of the system, and the effectiveness of the AOM control for PV converters. As it can be observed in Fig. 4.10, initially, each PV converter has an active power of 225 W, and the battery converter offers the remaining 175-W power to meet the 625-W load requirement. Both PV converters are operating in the MPPT mode, and the two PV voltages are oscillating around 55 V (MPP voltage), as shown Fig. 4.11. When the load is reduced to 165 W, the power of each PV converter is reduced to 95 W because of the AOM control, as it can be seen from Fig. 4.11, where the two PV voltages are increased to 62 V, which means that a part of PV power is curtailed to keep the modulation indices of PV converters within the allowed range. The amplitudes of $v_{ac,PV1}$ and $v_{ac,PV2}$ are maintained at around 53 V, and the amplitudes of the modulation indices for the two PV converters can be approximated as 0.85 (53 V/ 62 V), which are within the dead-band of the AOM control ([$m_{th,L}$, $m_{th,H}$]). The battery converter is charged to absorb the

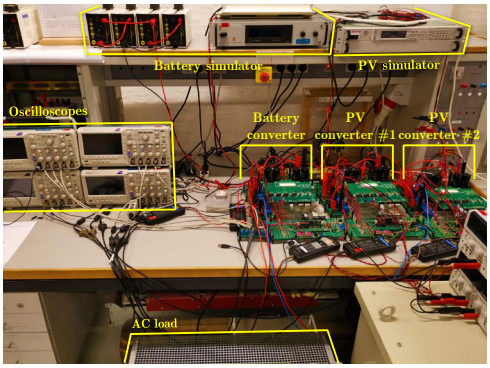

Fig. 4.9: Photo of the downscaled series-PV-battery system. Source: [**J3**].

Table 4.3: Parameters used for the experiments. Source: [**J3**].

Circuit parameters	Value
PV rated power per panel	260 W
LC filter for each converter	1.8 mH / 30 μF
DC capacitor for each converter	2000 μF
Amplitude of the grid nominal voltage $V_{g,nom}$	90 V
Battery nominal voltage	48 V
Control parameters	**Value**
Switching frequency of each converter	5 kHz
Sampling frequency of each controller	10 kHz
MPPT sampling-rate	5 Hz
MPPT perturbation step-size	2.5 V
Reactive power distribution coefficient d	2.8
Proportional gain of the AOM loop for PV converters	$k_{p,AOM,PV}$ = 50
Integral gain of the AOM loop for PV converters	$k_{i,AOM,PV}$ = 500
Proportional gain of the AOM loop for the battery converter	$k_{p,AOM,bat}$ = 30
Integral gain of the AOM loop for the battery converter	$k_{i,AOM,bat}$ = 100
Upper threshold for the AOM loop	$m_{th,H}$ = 0.9
Lower threshold for the AOM loop	$m_{th,L}$ = 0.8
Communication baud rate	9600 b/s

surplus 35-W power. The power control performance of the system is fast and stable during the load change, while the islanded AC voltage is sinusoidal with high quality.

Case 2: The control performance of the AOM loop for the battery converter is shown in Figs. 4.12 and 4.13, where the load active power steps from 165 W to 225 W, and load reactive power steps from 0 to −210 var. The initial conditions of the system are identical with the steady-state conditions of Case 1. As demonstrated in Fig. 4.12, after the load step, both P_{PV1} and P_{PV2} are increased to 160 W, while P_{bat} is decreased to −65 W. while the reactive power is distributed according to the active power contribution of each converter, being −10 var for each PV converter and −190 var for the battery converter. The apparent power can be accordingly calculated as 200 VA for the battery converter and 160 VA for each PV converter. Clearly, the battery converter contributes

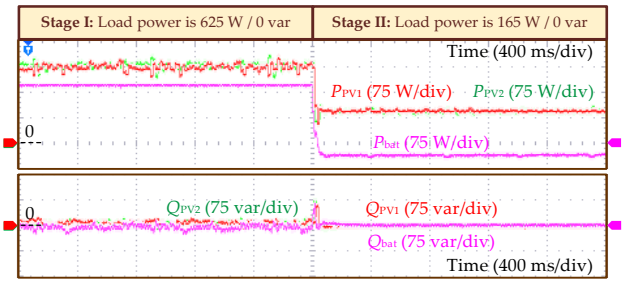

Fig. 4.10: Load active power step response of the series-PV-battery system, where P_{total} changes from 625 W to 165 W. Source: [**J3**].

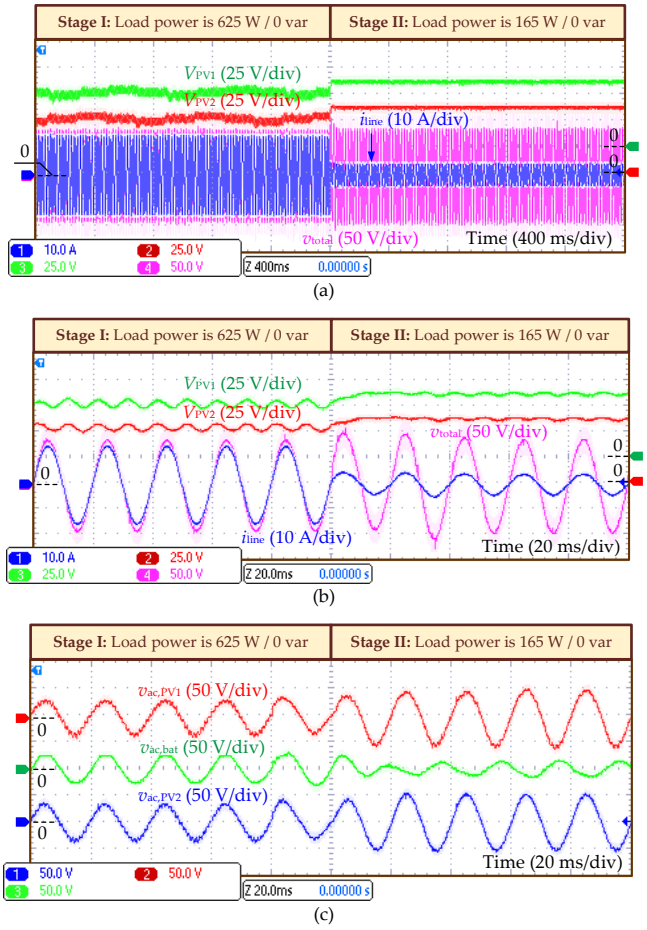

Fig. 4.11: Voltages and current of the series-PV-battery system when the load active power changes from 625 W to 165 W: (a) two PV voltages, total output AC voltage and the line current, (b) zoomed-in figure of Fig. 4.11(a), and (c) AC voltages of individual converters, where $v_{ac,PVm}$ refer to the output voltage of the m^{th} PV converter. Source: [**J3**].

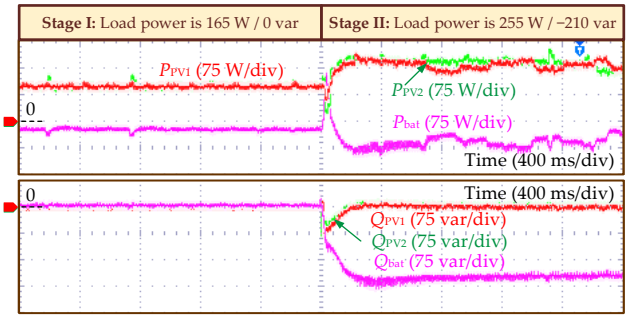

Fig. 4.12: Load *PQ* step response of the series-PV-battery system, where the load *PQ* change from 165 W / 0 var to 255 W / −210 var. Source: **[J3]**.

with more apparent power than each PV converter using the reactive power distribution strategy in (4.14) and (4.15), which can be further supported by Fig. 4.13, where the amplitude of $v_{ac,bat}$ is slightly larger than the amplitudes of $v_{ac,PV1}$ and $v_{ac,PV2}$. Since the battery converter provides more power, overmodulation of the battery converter appears at the 11th grid cycles after the load change. The overmodulation of the battery converter has lasted for approximately 13 grid cycles, and after that, the battery converter is in the linear modulation region again because of the AOM control, as demonstrated in Figs. 4.13(c) and 4.14. Both PV voltages are around 58 V, being 3-V higher than the 55-V MPP voltage, as shown in Fig. 4.13(a), which means that a small part of PV of power is discarded to keep all converters operating within the allowed modulation region. During the whole process of the load power step change, the total AC voltage is stable and sinusoidal, except a 20% voltage drop appeared in the first grid cycle after the load change (at the beginning of Stage II in Figs. 4.13(b)). In practice, such transient voltage drop can be avoided by appropriate start-up strategies. Nevertheless, the system can still be quickly stabilized with the proposed control even though the reactive load is "hard-started", which indicates that the designed system is of high stability.

Case 3: To demonstrate the reactive power distribution performance, experimental tests are performed under the same conditions as Fig. 4.11, but the PV power is halved. It can be observed from Fig. 4.15 that both P_{PV1} and P_{PV2} are approximately 120 W, while the battery converter contributes the remaining 15-W power after the load change. Both PV converters are back to the MPPT mode again, as it can be observed from Fig. 4.16(a), where V_{PV1} and V_{PV2} are oscillating around 55 V. The reactive power of −30 var is provided by each PV converter, while the battery converter contributes the remaining −150-var power. Accordingly, the apparent power can be obtained as 150.7 VA for the battery converter and 123.7 VA for each PV converter, indicating that the total load power is shared among all converters in a way to balance their loading with the reactive power distribution method. Evidence can be found by Fig. 4.16, where the AC voltages of the three converters have similar amplitudes.

Clearly, the optimal reactive power distribution is not achieved with the strategy in (4.14) and (4.15). As discussed previously, it can be accomplished by employing the

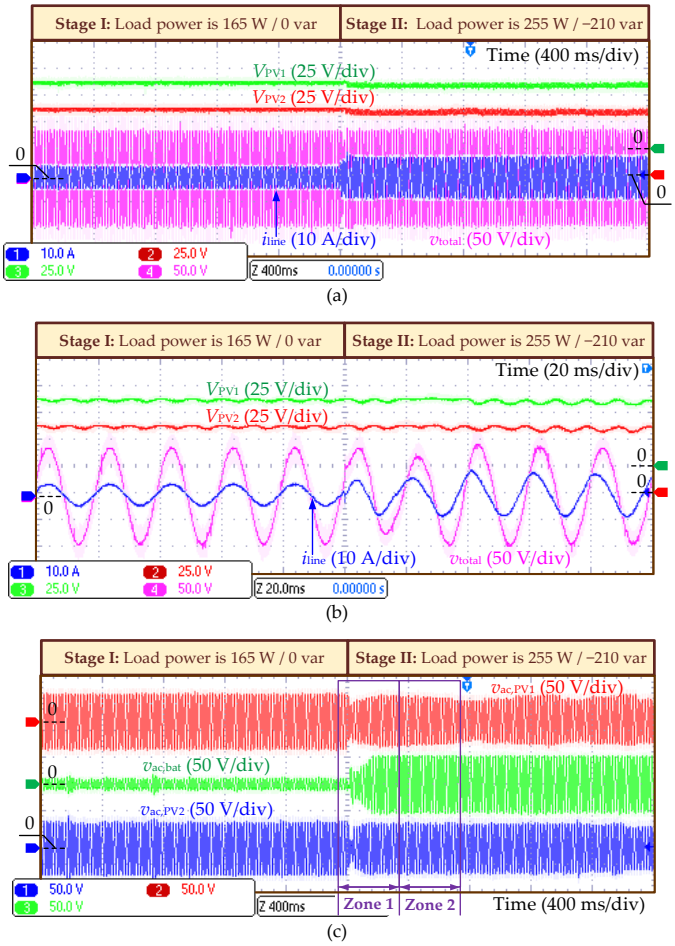

Fig. 4.13: Voltage and current response of the series-PV-battery system when the load *PQ* change from 165 W and 0 var to 255 W and −210 var: (a) two PV voltages, total output AC voltage and the line current, (b) zoomed-in plot of Fig. 4.13(a), and (c) AC voltages of individual converters. Source: **[J3]**.

optimization-based approach, which is developed in **[C5]**. More experimental results can also be found in **[C5]** in terms of the optimal reactive power distribution, which will not be detailed in this chapter.

Comparisons between the proposed distributed control scheme and the conventional hierarchical control in [37] and [38] are shown in Table 4.4. Clearly, the amount of required data for communication can be significantly reduced with the proposed control, while real-time communication is no longer required. In the experiments, the proposed distributed control is achieved with a slow communication speed (9600 b/s) using the RS-485 protocol, being much lower than the communication speed in [38] (i.e., 1 Mb/s).

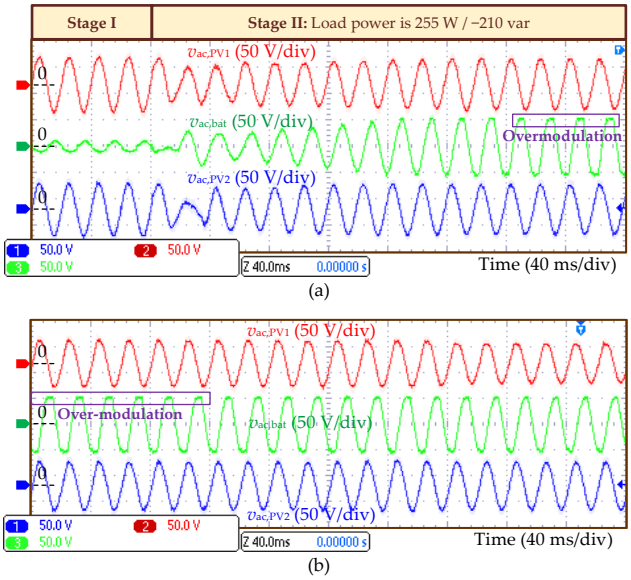

Fig. 4.14: Zoomed-in plots of (a) Zone 1 and (b) Zone 2 in Fig. 4.13(c). Source: [**J3**].

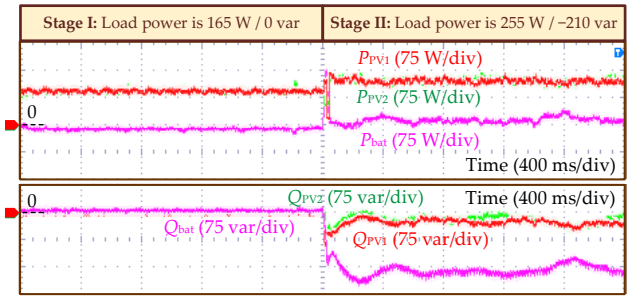

Fig. 4.15: Load *PQ* step response of the series-PV-battery system with halved available PV power, where the load *PQ* change from 165 W / 0 var to 255 W / −210 var. Source: [**J3**].

4.4. Summary

A distributed control method for islanded series-PV-battery systems was developed in this chapter, which includes the *PQ* decoupling control for distributed PV converters, droop control for the battery converter, AOM control for all converters, and the reactive power distribution strategies. With the *PQ* decoupling control, individual PV converters can achieve independent *PQ* regulation and self-synchronization using only local measurements, enabling the communication-free operation of the series system regardless of its PFs. The battery converter automatically compensates the power difference between the PV power and the load requirement, while maintaining the output of the series system following the droop curve, which

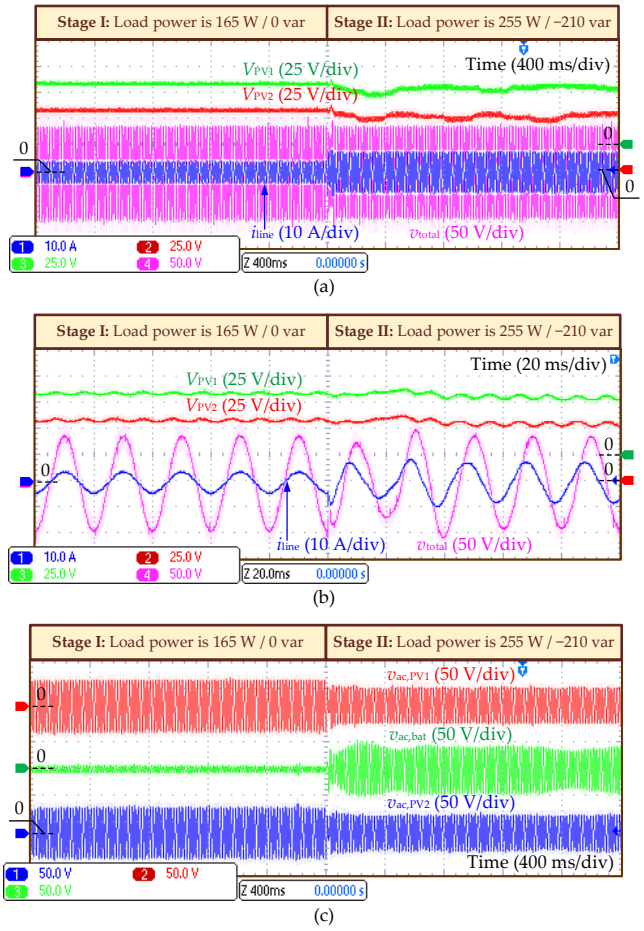

Fig. 4.16: Voltage and current response of the series-PV-battery system with halved available PV power, where the load *PQ* change from 165 W / 0 var to 255 W / −210 var: (a) two PV voltages, total output AC voltage and the line current, (b) zoomed-in plot of Fig. 4.16(a), and (c) AC voltages of individual converters. Source: [**J3**].

enables the participation of the system in the regulation of the grid voltage and frequency. To analyze the stability performance of the system, a small signal model was developed for systems with the proposed control, which can be used for the tuning of control parameters. To alleviate the overloading/overmodulation risks of certain converters, the reactive power is distributed among all converters in a way to achieve balanced apparent power sharing among all converters. In addition, two AOM loops were developed to tackle the overmodulation, which are both achieved curtailing a part of PV power. Although the reactive power distribution as well as the AOM for the battery converter are dependent on the LBC, they have very low requirements for the communication, by which only a few control variables with slow dynamics are required to be transmitted. Experiments were conducted to validate the

Table 4.4: Comparisons of the low-bandwidth communication between the conventional hierarchical control method and proposed distributed control method. Source: [**J3**].

Parameters / Methods	Necessary communication variables		Communication protocol	Baud-rate of the LBC in experiments
	Variables requiring real-time transmission	Variables not requiring real-time transmission		
Conventional hierarchical control [37], [38]	P_{PV1}, … P_{PVn-1}, P_{bat}, Q_1^*, … Q_{n-1}^*, V_{PV1}, … V_{PVn-1}, V_{bat}, M_{total} ($3n$ variables in total)	M_{total}[a], $\Delta\theta_{mtotal}$[b], $\Delta M_{p,1}$, … $\Delta M_{p,n-1}$[c], $\Delta M_{q,1}$, … $\Delta M_{q,n-1}$[d] ($2n$ variables in total)	CAN	1 Mb/s
Proposed control [**J3**]	P_{total}, Q_{total}, M_{bat}, P_{PV1}, … P_{PVn-1}, *Bat_AOM_Flags*[e] (n + 3 variables in total)	No variables	RS-485	9.6 Kb/s

[a]M_{total} is the amplitude of m_{total}, which is calculated by the total power control in the central controller [38].
[b]$\Delta\theta_{mtotal} = \theta_{mtotal} - \theta_i$, where θ_{mtotal} and θ_i are the phase angles of m_{total} and i_{line}, respectively [38].
[c,d]$\Delta M_{p,k}$ and $\Delta M_{q,k}$ are the outputs of local PQ controllers of the kth converter, both of which will be added to M_{total} to calculate M_k [38]. According to [38], $M_k = M_{total} + \Delta M_{p,k}$ and $\Delta M_{q,k}$.
[e]All *Bat_AOM_Flag* signals can be combined as one variable for communication, as each of them are bit-type signals.

effectiveness of the proposed control in terms of the individual PQ control, AOM, and the reactive power distribution.

Related Publications

J3. **Y. Pan**, A. Sangwongwanich, Y. Yang, and F. Blaabjerg, "Distributed control of islanded series PV-battery-hybrid systems with low communication burden," *IEEE Trans. Power Electron.*, vol. 36, no. 9, pp. 10199-10213, Sept. 2021.

C4. **Y. Pan**, Y. Yang, and F. Blaabjerg, "Distributed control of islanded series PV-battery-hybrid systems with low communication burden," in Proc. *IEEE PEDG*, 2020, pp. 315-321.

C5. **Y. Pan**, A. Sangwongwanich, Y. Yang, and F. Blaabjerg, "Optimization of reactive power distribution in series PV-battery-hybrid systems," in *Proc. IEEE ECCE*, 2021, pp. 520-525.

Chapter 5.
Flexible Active Power Control for Grid-Connected Series-PV-Battery Systems

5.1. Background

As discussed in Chapter 1, to avoid the voltage and frequency instability issues due to the increasing penetration of PV systems, flexible active power control (FAPC) functions are required for grid-connected PV systems [6], [72], [78]. Conventionally, the FAPC for single-PV-converter systems is achieved by the modification of the MPPT algorithm, where the PV operating point is perturbed around a curtailed power point rather than at its MPP [6], [72], [73], [97]-[100]. However, when applying these FAPC methods to series-PV-battery systems, there are certain limitations to overcome:

- How to distribute of the curtailed power among multiple converters has not been discussed in prior-art strategies in [6], [72], [73], [97]-[100], which were developed for single-converter systems. Nevertheless, it is an important issue in series-PV-battery systems, where individual converters will become unevenly loaded if the curtailed power is distributed improperly. In extreme cases, the operation of the system can be beyond its allowed operating region [101], leading to undesired power curtailment or instability of the system [**J3**], [**J4**].
- The charging/discharging power limit and SoC conditions of the battery converter should be considered when distributing the curtailed power among individual converters. However, in [6], [72], [73], [97]-[100], no batteries have been included in the system configuration, and the FAPC constraints are maintained by directly discarding a part of PV power.
- To achieve the PRC, the MPP of each PV converter should be periodically observed to determine the reserved power level [98]. The observation of MPP is usually realized by routinely operate the PV converters in the MPPT mode [98]. However, for series-PV-battery systems, if the observation of MPPs for individual PV converters is not properly coordinated, certain converters can operate in the MPPT mode simultaneously. This can lead to large excessive power, which can be difficult to be compensated by the battery converter. Consequently, the battery converter may fail to maintain the total power reserve

constraints. Especially when the reserved power is a large, the conflict between observing the MPPs of PV converters and achieving the desired power reserve will be severe.

Apart from the above FAPC strategies for single-converter systems, several FAPC strategies have particularly been designed for series-connected systems [40], [74], [102]. For instance, a PRRC method for series-PV-battery systems can be found in [40], which is based on the CVM control. Two PRC strategies have been developed for CHB PV inverters, where the total power can be curtailed according to the grid frequency and the output of a virtual synchronous generator (VSG) in [74] and [102], respectively. However, similar limitations remain in these strategies:

- The distribution of the curtailed power is not considered in [40] and [74], while all the reserved power is assigned to only one converter in [102], resulting in a limited power reserve capability (limited to the capacity of one converter cell). Especially when the power reserve becomes large, the uneven loading condition among all converters will aggravate with the strategy in [102].
- It has not been addressed in [74] and [102] about the method to avoid the conflict between observing the MPPs of PV converters and achieving the power reserve.
- The battery power and SoC constraints have not been considered either. More specifically, 1) no batteries are included in [74] and [102], and 2) the PRRC in [40] will not be effective when the battery is fully charged.

Considering the above, in this chapter, various FAPC strategies for series-PV-battery systems (including the PRRC, PLC, and PRC strategies) are proposed based on the distributed control architecture discussed in Chapter 4. With these strategies, the total power of the system can be flexibly controlled according to the power ramp-rate, limiting, and reserve constraint commands. The surplus PV power is distributed among all converters considering 1) the battery power and SoC conditions, 2) the available power of each PV converter, and 3) periodical MPP estimation of each PV converter. All converters are coordinatively controlled to achieve the above functions. Experiments have been conducted to demonstrate the effectiveness of the proposed strategies.

5.2. Flexible Active Power Control Strategies

5.2.1. Overall Control Architecture

The hardware structure and the control architecture of a series-PV-battery system with n cascaded converters is shown in Fig. 5.1, including n_1 battery converters and n_2 PV converters. The 1st battery converter (master controller) is responsible for 1) collecting and sending the operating conditions of each converter to the grid layer controller for power scheduling, 2) receiving the FAPC commands from the grid control layer, and 3) sending the commands and information to individual converters. In addition, this battery converter is also in charge of directly regulating the total PQ of the system, as shown in Fig. 5.2. All other converters are controlled locally using the

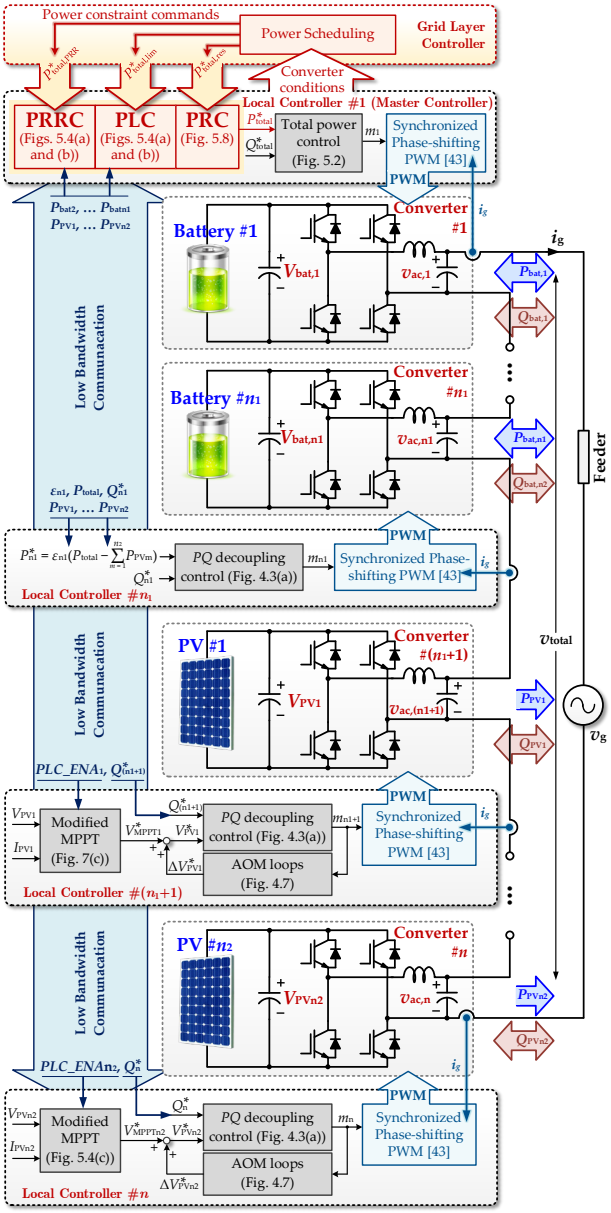

Fig. 5.1: Control diagram of an n-cell series system with n_1 battery converters and n_2 PV converters, where $P^*_{\text{total,PRR}}$, $P^*_{\text{total,lim}}$, and $P^*_{\text{total,res}}$ are the total power ramp-rate, limiting, and reserve commands from the grid layer control, respectively, P^*_{total} and Q^*_{total} are the total PQ references, respectively, $V_{\text{bat,k}}$ is the DC voltage of battery #k, and PLC_ENA_k is the power limiting signal for the k^{th} PV converter #k. Source: [**J4**].

PQ decoupling control discussed in the previous chapter, and are interlinked with the 1st battery converter through the LBC. For PV converters, their active power references

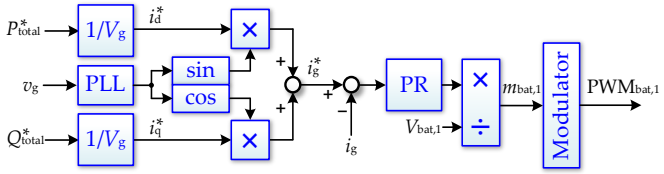

Fig. 5.2: Power control loops for the battery converter #1 in Fig. 5.1, which is responsible for regulating the total active and reactive power of the series-connected system. Source: [**J4**], [**C6**].

are generated by the MPPT control, as discussed in Chapter 4. For other battery converters (except the 1st battery converter), as they should also provide the power compensation functionality, their active power references can be obtained by

$$P_k^* = \varepsilon_k \left(P_{total} - \sum_{m=1}^{n_1} P_{PVm} \right) \tag{5.1}$$

where ε_k is the power distribution ratio of the k^{th} converter. In practice, ε_k can be related to the battery SoC and power capacity [13], [37], [103], and can be selected as

$$\varepsilon_k = SoC_k \cdot C_{bat,k} \Big/ \sum_{m=1}^{n_2} \left(SoC_m \cdot C_{bat,m} \right) \tag{5.2}$$

in which SoC_k and $C_{bat,k}$ are the SoC and capacity of the k^{th} battery, respectively. According to (5.2), the battery power will be proportionally shared among all converters depending on the available capacity of each battery, and the SoC balancing control among batteries can thus be achieved. Considering that both the battery SoC and the coefficient ε_k are of slow dynamics, only one battery unit is considered in the remaining analysis for simplification. Therefore, similar to the case in Chapter 4, an n-cell system with one battery converter is considered in the following.

5.2.2. Power Ramp-Rate and Power Limiting Control

Depending on the charging/discharging power and SoC conditions of batteries, three operating modes have been designed for the PRRC and PLC strategies, which are illustrated in Fig. 5.3, where the operation of a 3-cell system is exemplified:

- *Mode 1:* Normally, the difference between the PV power and the total required power is fully compensated by the battery, as shown in Figs. 5.3(a), (d), and (g).
- *Mode 2:* When the power required to be compensated by the battery is too much, the battery power will be limited to its maximum allowed charging/discharging power, as shown in Figs. 5.3(b), (e) and (h). As a result, a part of PV power will be discarded to maintain the total power ramp-up and power limiting constraints, while the power ramp-down constraint will not be maintained for a period being T_{sat}, during which the battery cannot provide sufficient power.
- *Mode 3:* When the battery SoC reaches its upper or lower limit, battery charging or discharging will be disabled, respectively. In this case, all excessive PV power

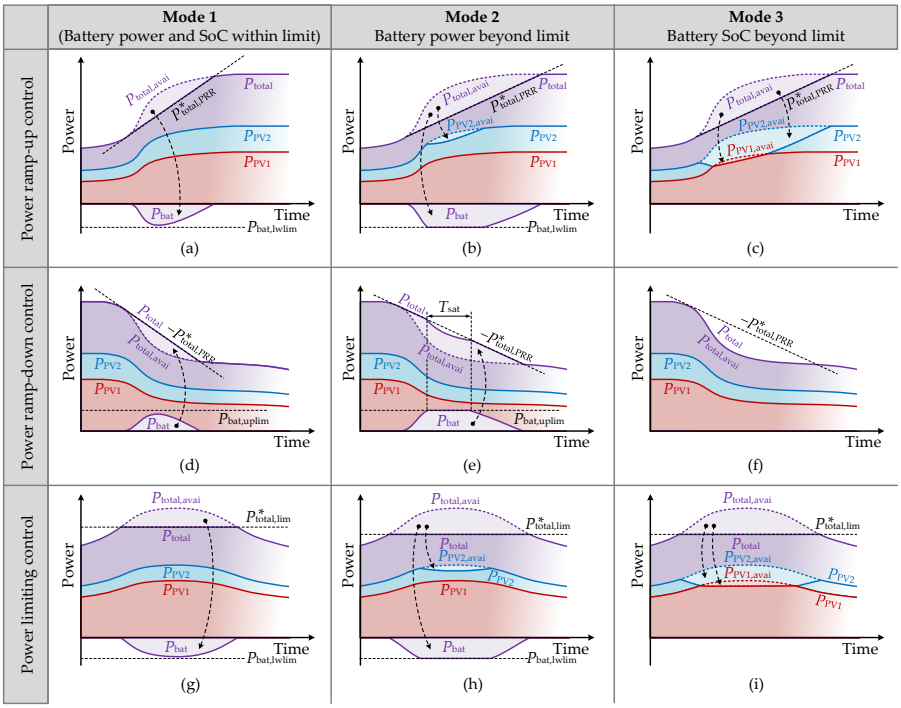

Fig. 5.3: Three operating modes of the proposed PRRC and PLC strategies, where the operation of a 3-cell system under the (a)-(c) power ramp-up, (d)-(f) power ramp-down, and (c) power limiting conditions are demonstrated, $P_{\text{total,avai}}$ and $P_{\text{PVk,avai}}$ are the available power of the entire system and the k^{th} PV converter, respectively, $P_{\text{bat,uplim}}$ and $P_{\text{bat,lwlim}}$ are the charging and discharging power limits (upper and lower power limits) of the battery converter, respectively, and T_{sat} is the period when the power ramp-down constraint fails to be maintained because of the insufficient battery power. Source: [**J4**].

will be discarded under the power ramp-up and PLC conditions, as demonstrated in Figs. 5.3(c) and (i). Notably, the power of both PV converters is curtailed to the same level to balance their loadings. During power ramp-down, since the battery cannot provide the power buffering function, the power ramp-rate (PRR) constraint cannot be maintained, as shown in Fig. 5.3(f). Nevertheless, such operation conditions (including the condition in Fig. 5.3(e)) should be prevented in practice, by allocating batteries with sufficient capacities.

According to the analysis of the three operation modes, the control flow charts of the PRRC and PLC is designed, as given in Fig. 5.4. The basic idea of the PRRC is explained in the following: if P_{bat} is higher or lower than its steady-state charging/discharging power reference P^*_{bat}, P^*_{total} will be decreased or increased by P_{step} in each control period T_{s}. With such approach, P_{total} will change with a PRR of $P_{\text{step}}/T_{\text{s}}$. P^*_{bat} can be manually set according to charging/discharging power limits and the SoC condition of the battery. For instance, it can be set as zero, which means that the battery will be neither charged nor discharged in steady state, but still responsible for compensating the power difference between the PV power and the constrained P_{total}

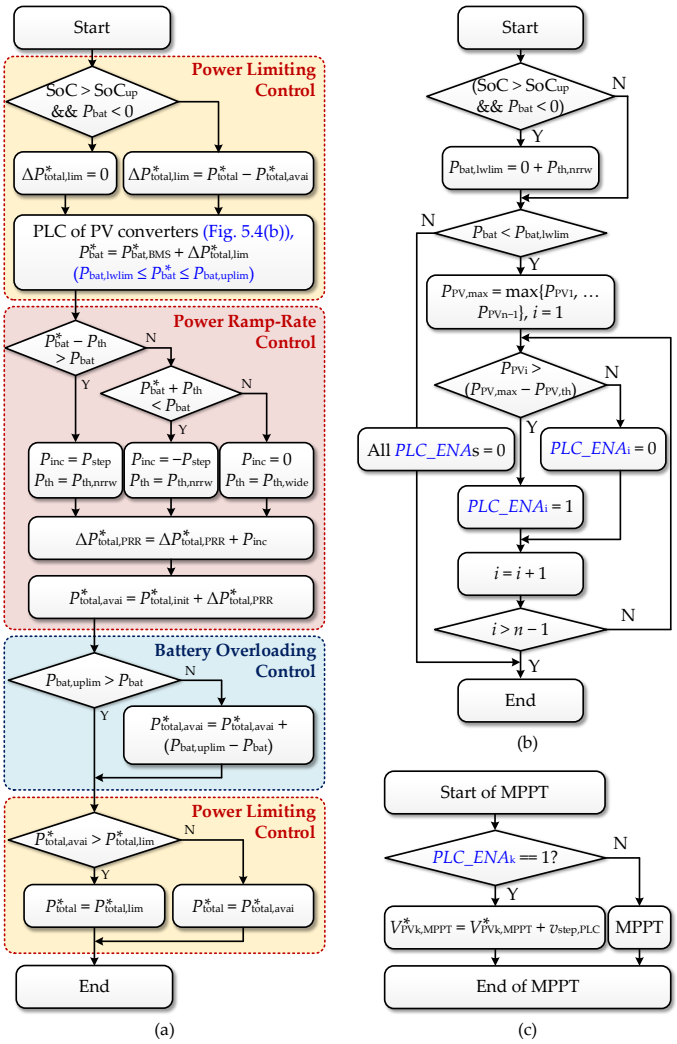

Fig. 5.4: Control flowcharts of the proposed PRRC and PLC strategies: (a) and (b) the algorithm executed by the controller of the battery converter, and (c) the algorithm executed by the controllers of PV converters ($P^*_{\text{total,init}}$ – the initial value of P^*_{total}; $P^*_{\text{total,avai}}$ – the reference of $P_{\text{total,avai}}$; and $\Delta P^*_{\text{total,PRR}}$ – the total adjustment on $P^*_{\text{total,avai}}$ for the PRRC control, accumulated by P_{inc} every control period. Source: [**J4**].

during dynamics. To eliminate the steady-state oscillation on P^*_{total}, a hysteresis band P_{th} is introduced in the control, as shown in Fig. 5.4(a). P_{th} can be assigned with two values, which are denoted as $P_{\text{th,wide}}$ and $P_{\text{th,nrrw}}$ ($P_{\text{th,wide}} > P_{\text{th,nrrw}}$). When P_{bat} is within the range of $\left(P^*_{\text{bat}} - P_{\text{th}}, P^*_{\text{bat}} + P_{\text{th}}\right)$, P_{th} will be set as $P_{\text{th,wide}}$ to avoid frequent perturbations on P^*_{total}. When P_{bat} is beyond the range of $\left(P^*_{\text{bat}} - P_{\text{th}}, P^*_{\text{bat}} + P_{\text{th}}\right)$, P_{th} will be changed as $P_{\text{th,nrrw}}$ to reduce the steady-state errors induced by the hysteresis width P_{th}.

Notably, P^*_{bat} should be maintained within the allowed operation range [$P_{bat,lwlim}$, $P_{bat,uplim}$] according to the battery conditions. However, if the battery SoC is beyond SoC_{up} (the upper limit of the SoC), or the battery charging power is beyond its maximum charging power limit (lower power limit) $P_{bat,lwlim}$, the PLC of PV converters will be activated, as demonstrated in Fig. 5.4(b). In this case, PV converters with their power close to $P_{PV,max}$ will be selected for power curtailment. As shown in Fig. 5.4(b), if the power of the i^{th} PV converter is higher than ($P_{PV,max} - P_{PV,th}$), the PLC signal for the i^{th} converter (PLC_ENA_i) will be enabled, which will disable the MPPT operation of this converter. In this case, the PV voltage reference of this converter will be increased by a small step ($v_{step,PLC}$) every MPPT period to achieve the PV power curtailment, as illustrated in Fig. 5.4(c). Here, a small threshold $P_{PV,th}$ is used to enable the power curtailment of multiple PV converters. On the other hand, if the battery is operating in normal conditions ($SoC < SoC_{up}$ and $P_{bat} > P_{bat,lwlim}$), no PV converters will be selected for power curtailment, and all *PLC_ENA* signals will be reset to zero.

The PLC of the entire system is achieved similarly. As shown in Fig. 5.4(a), when the total available power generated by the PRRC ($P^*_{total,avai}$) is larger than $P^*_{total,lim}$, P^*_{total} will be saturated to $P^*_{total,lim}$. Meanwhile, the excessive power $\left(P^*_{total} - P^*_{total,avai}\right)$ will be added to P^*_{bat}, indicating that the excessive power is fully absorbed by the battery. When the excessive power $\left(P^*_{total} - P^*_{total,avai}\right)$ is beyond the range of [$P_{bat,lwlim}$, $P_{bat,uplim}$], the power curtailment control of PV converters shown in Figs. 5.4(b) and (c) will be enabled to avoid overloading the battery converter.

During the power ramp-down, the PRR constraint cannot be maintained if the battery power reaches its maximum discharging power limit (upper power limit) or battery SoC reaches its lower limit SoC_{dw}. To avoid overloading the battery, an anti-overloading control is included. According to Fig. 5.4(a), if the battery power is higher than its upper limit ($P_{bat,uplim}$ is set as zero when the battery SoC reaches SoC_{dw}), the excessive power ($P_{bat} - P_{bat,uplim}$) will be directly subtracted from $P^*_{total,avai}$, thus preventing the battery converter from overloading.

5.2.3. Power Reserve Control

In addition to maintaining the power reserve constraint, the available power estimation of each PV converter is essential. To achieve this objective, a sensorless PRC strategy in [98] can be employed. In this strategy, individual PV converters routinely alter their operation modes between the MPPT and the PLC modes. When the MPPT is enabled, the available power of each PV converter is estimated using the measured MPP power, while the excessive power beyond the PRC limit is temporarily stored in the battery units. In the proposed PRC, the available power of series-PV-battery systems is estimated similarly, i.e., by the routinely MPPT operation. Nevertheless, if the MPPT operation of different PV converters is not properly coordinated, e.g., certain PV converters operate in the MPPT mode simultaneously, the excessive PV power will be significantly increased beyond the PRC limit, which is difficult to be fully compensated by the battery converter, as illustrated in Fig. 5.5(a). To address this, in the proposed PRC strategy, the MPPT operation of different PV converters are enabled

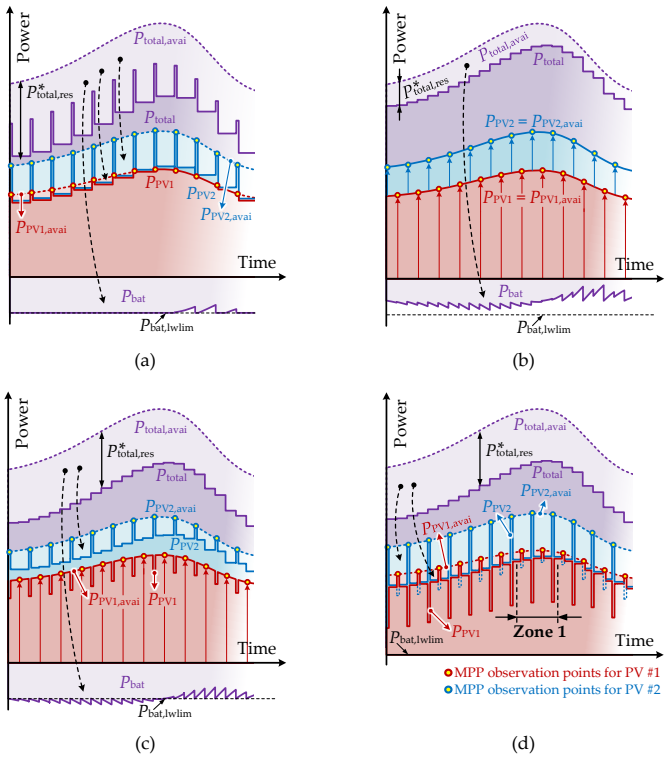

Fig. 5.5: Demonstration of the PRC: (a) conventional PRC in [98] is directly applied, (b), (c), and (d): Modes 1, 2, and 3 of the proposed PRC, where $P_{PVk,avai}$ is the available power of the k^{th} PV converter. Source: [**J4**].

in sequence, and the enabling signals are shown in Fig. 5.6. Clearly, at any time instant, the MPPT operation is enabled for only one PV converter. Then, according to the enabling signals, the operation of the k^{th} converter can be divided into three periods:

1) In Period I, the MPPT is enabled for this converter.
2) In Period II, the MPPT is disabled for all PV converters.
3) In Period III, the MPPT is enabled for any other PV converters.

With the above coordination, the simultaneous MPPT operation of multiple converters can be avoided, as shown in Figs. 5.5(b)-(d), where the operating waveforms of the proposed PRC are demonstrated. It can be noticed from Figs. 5.5(b)-(d) that three operation modes have also been designed in the proposed PRC strategy, respectively, which are similar to the three modes of the PRRC and PLC in Section 5.2.2:

- *Mode 1:* All excessive power beyond the required power reserve is compensated by the battery, as illustrated in Fig. 5.5(b).
- *Mode 2:* When $P^*_{total,res}$ is larger than the battery charging limit $|P_{bat,lwlim}|$, only a part of power being $|P_{bat,lwlim}|$ will be compensated by the battery, while the rest part of the excessive power is discarded, as demonstrated in Fig. 5.5(c).

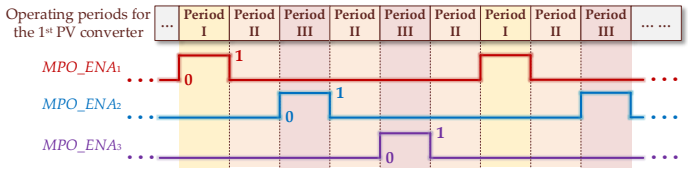

Fig. 5.6: MPPT enabling signals for individual PV converters. Source: [**J4**].

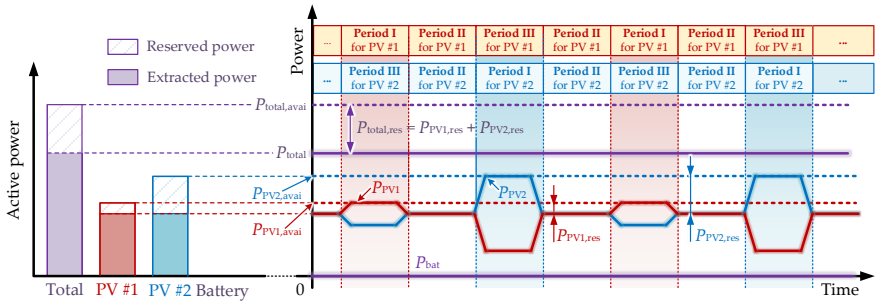

Fig. 5.7: Zoomed-in figure of Zone 1 in Fig. 5.5(d). Source: [**J4**].

- *Mode 3:* When the battery SoC reaches SoC_{up}, all reserved power is discarded, as demonstrated in Fig. 5.5(d).

It can be noticed from Figs. 5.5(b)-(d) that the operation of the system with the proposed PRC is more complex than the PRRC and PLC strategies. As shown in Figs. 5.5(c) and (d), due to the routinely operation mode switching of different PV converters, when one PV converter estimates its MPP, further power curtailment may be required for the other PV converter in order to maintain the power reserve constraints. Zoomed-in operation waveforms of Zone 1 in Fig. 5.5(d) is shown in Fig. 5.7, where the routinely MPPT of different converters is coordinated by the *PLC_ENA* signals. According to the operation waveforms in Figs. 5.5(b)-(d) and Fig. 5.7, a PRC strategy shown in Fig. 5.8 is designed, which is explained as follows:

1) At the beginning of Period I for the k^{th} converter, its MPPT operation is enabled by resetting PLC_ENA_k as 0. Then, the historical highest $P_{PVk,avg}$ (the average power of the k^{th} converter) during Period I will be regarded as the available power of the k^{th} converter ($P_{PVk,avai}$). $P_{PVk,avg}$ is obtained by using a low-pass filter (LPF). To accelerate the process of the available power estimation, the PV reference voltage can be set as $F_V V_{PV,OC}$ at the start of Period I (F_V can be selected between 71–78%, and $V_{PV,OC}$ is the PV open-circuit voltage) [98].
2) When it enters to Period II, the total available power of the system $P^*_{total,avai}$ is obtained by summing up $P_{PVk,avai}$ of all PV converters. Then, a power limiting threshold $P^*_{PV,PLC}$ is calculated, which determines the power limiting level of all PV converters. According to the number of power-curtailed PV converters, the calculation of $P^*_{PV,PLC}$ has also three cases like shown in Fig. 5.9, where the power curtailment of a 4-cell system with three PV converters is exemplified:

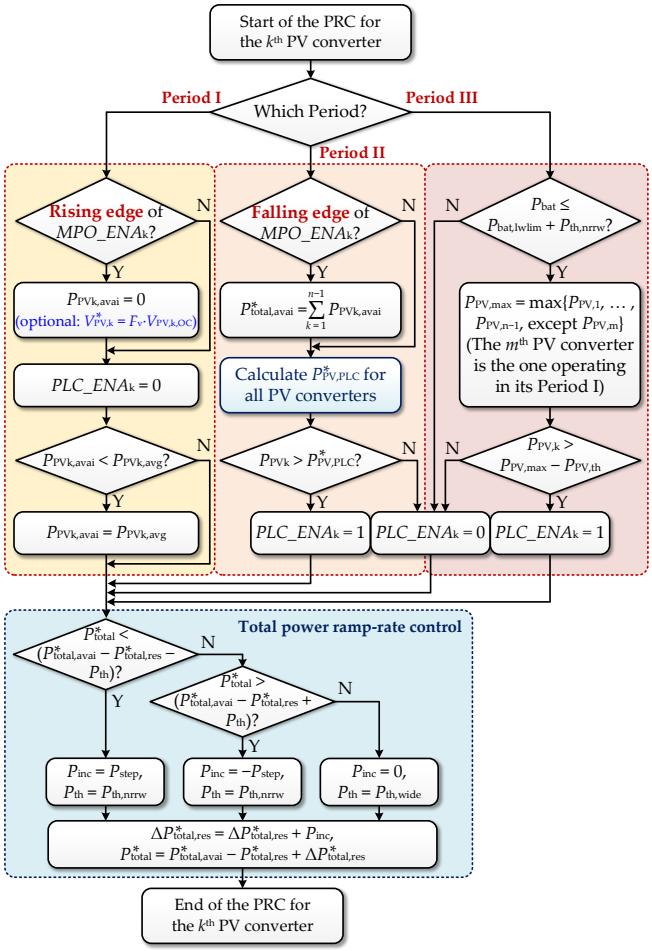

Fig. 5.8: Control algorithm of the proposed PRC. Source: [**J4**].

- Case 1: When all reserved power is absorbed by the battery, $P^*_{PV,PLC}$ is larger than any $P_{PVk,avai}$, as shown in Fig. 5.9(a).
- Case 2: When not all PV converters are power-curtailed, $P^*_{PV,PLC}$ will be larger than at least $P_{PVk,avai}$, as illustrated in Fig. 5.9(b), where only the 1st and 3rd PV converters are power-curtailed, while no power is curtailed from the 2nd PV converter.
- Case 3: When all PV converters are power-curtailed, $P^*_{PV,PLC}$ is lower than any $P_{PVk,avai}$, as shown in Fig. 5.9(c).

An algorithm is accordingly developed to obtain $P^*_{PV,PLC}$. Firstly, all PV converters are sorted according to their available power. More specifically, after the sorting, the $x(1)^{th}$ PV converter will be the one with the highest available power, while the $x(n-1)^{th}$ will be the one with the lowest. Their

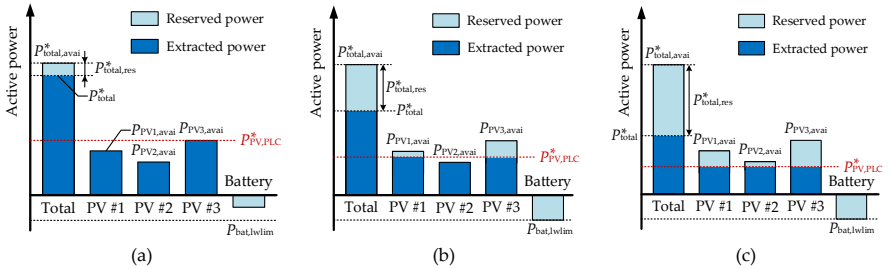

Fig. 5.9: Three cases to calculate $P^*_{\text{PV,PLC}}$ for a 4-cell system with three PV converters: (a) Case 1: no PV power curtailment, (b) Case 2: a part of PV converters are power curtailed, and (c) Case 3: all PV converters are power-curtailed. Source: [**J4**].

available power are denoted as $P_{\text{PVx(1),avai}}$ and $P_{\text{PVx(n−1),avai}}$, respectively. With the sorted indices $\boldsymbol{x}$, the $P^*_{\text{PV,PLC}}$ values for the above three cases can be calculated:

- Case 1: if $P^*_{\text{total,res}} < |P_{\text{bat,lwlim}}|$, $P^*_{\text{PV,PLC}}$ is assigned with a large value M, which is much larger than $P_{\text{PVx(1),avai}}$, and no PV power will be discarded.
- Case 2: if $P^*_{\text{total,res}} > |P_{\text{bat,lwlim}}|$, the algorithm will search from the $x(1)^{\text{th}}$ to the $x(n-1)^{\text{th}}$ PV converters to determine the number of power-curtailed PV converters. In the α^{th} searching round, $P_{\text{PVx}(\alpha+1),\text{avai}}$ is assumed as the value of $P^*_{\text{PV,PLC}}$. With this assumption, the amount of curtailed PV power can be calculated using

$$\Delta P_{\text{comp}} = \sum_{m=1}^{\alpha}\left(P_{\text{PVx(m),avai}} - P_{\text{PVx}(\alpha+1),\text{avai}}\right) \tag{5.3}$$

  where ΔP_{comp} is the assumed curtailed power. If ΔP_{comp} is smaller than the total discarded power $\left(P^*_{\text{total,res}} - P_{\text{bat,lwlim}}\right)$, the searching will be continued by increasing α by 1. If not, the searching will be stopped, and the $x(1)^{\text{th}}$ to the $x(\alpha)^{\text{th}}$ PV converters will be selected for power curtailment. $P^*_{\text{PV,PLC}}$ can be calculated by

$$P^*_{\text{PV,PLC}} = \left(\sum_{m=1}^{\alpha} P^*_{\text{PVx(m),avai}} - P^*_{\text{total,res}} - P_{\text{bat,lwlim}}\right) \Big/ \alpha \tag{5.4}$$

- Case 3: if ΔP_{comp} is still smaller than $\left(P^*_{\text{total,res}} - P_{\text{bat,lwlim}}\right)$ when $\alpha = n - 1$, the power of all PV converters should be curtailed. In this case, $P^*_{\text{PV,PLC}}$ is calculated by

$$P^*_{\text{PV,PLC}} = \left(P^*_{\text{total,avai}} - P^*_{\text{total,res}} - P_{\text{bat,lwlim}}\right) \Big/ (n-1) \tag{5.5}$$

With (5.3)-(5.5), the power limiting threshold for PV converters can be calculated. Then, the *PLC_ENA* signals can be generated for individual PV converters by comparing their power and $P^*_{\text{PV,PLC}}$.

3) In Period III of the k^{th} converter, to maintain $P^*_{\text{total,res}}$, the power of the k^{th} converter may be further curtailed due to the MPPT operation of another PV

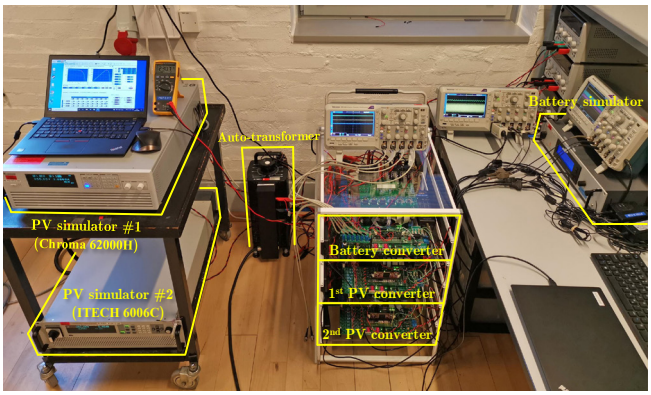

Fig. 5.10: A 3-cell series-PV-battery experimental setup for the FAPC. Source: [**J4**].

converter, as shown in Fig. 5.7. More specifically, if P_{bat} is lower than $P_{bat,lwlim}$, while the power of the k^{th} converter is close to $P_{PV,max}$, the power of this converter will be further curtailed by enabling PLC_ENA_k. $P_{PV,max}$ is the maximum power among all PV converters except the one in the MPPT mode. A control dead-band $P_{PV,th}$ is introduced to enable simultaneous power curtailment of multiple PV converters.

With the above control strategies for Period I, II, and III, the total available power reference $P^*_{total,avai}$, and the power limiting commands PLC_ENAs for individual PV converters, are obtained. Then, P^*_{total} can be calculated by subtracting the required power reserve $P^*_{total,res}$ from $P^*_{total,avai}$. In the control flowchart in Fig. 5.8, P^*_{total} is determined following a ramp-rate ($P^*_{total,PRR} = P_{step} / T_s$), which is achieved with a similar hysteresis control approach shown in Fig. 5.4(a). Overall, the available power estimation and the power curtailment control of individual PV converters can be achieved with the proposed three-stage PRC strategy, while the reserved power is coordinately assigned to individual converters considering the required total power reserve, PV available power, and the charging/discharging power limits and SoC conditions of batteries.

5.3. Experimental Validation

To validate the effectiveness of the proposed PRRC, PLC and PRC strategies, experiments tests have been performed on a 3-cell grid-connected series-PV-battery system, as shown in Fig. 5.10. Parameters in the experiments are shown in Table 5.1, unless otherwise noted. Considering that three operation modes of the proposed PRRC, PLC and PRC are similar in terms of the distribution of the curtailed power, only the operation Mode 2 of the proposed PRC is validated experimentally, when the PV power is partially curtailed. Five cases of experiments have been performed:

Case 1: The first test demonstrates the control performance of the series-PV-battery system under the power ramp-up and power limiting constraints (Mode 1 of the PRRC

Table 5.1: Parameters for the experimental setup for the FAPC. Source: **[J4]**

Circuit parameters	Value
DC-side capacitors of each PV converter	1360 μF
DC-side capacitors of the battery converter	680 μF
LC filter of each converter	1.8 mH / 30 μF
Grid nominal voltage V_g (RMS) and frequency	230 V / 50 Hz
Power rating of PV converters	1000 W
Parameters of each PV panel at the STC[a]	**Value**
Open circuit voltage $V_{PV,oc}$	333.7 V
Short circuit current $I_{PV,sc}$	4.33 A
PV voltage and current at its MPP (V_{MPP} and I_{MPP})	261.5 V / 3.824 A
Parameters of the battery converter	**Value**
Nominal DC voltage	144 V
Maximum power	±600 W
Battery capacity	20 Ah
Control parameters of individual converters	**Value**
Switching frequency of each converter	10 kHz
Sampling frequency of each converter	10 kHz
MPPT sampling rate	5 Hz
MPPT perturbation step-size	6 V
Power control parameters for PV converters[b]	$k_{p,P} = -2$, $k_{i,P} = -2$, $k_{p,q} = 0.12$, $k_{i,q} = 0.4$
Power control parameters for the battery converter[c]	$k_{p,p,total} = k_{p,q,total} = 0.005$, $k_{i,p,total} = k_{i,q,total} = 1$
Threshold for AOM loops	$m_{th,L} = 0.85$, $m_{th,H} = 0.9$
Communication baud rate	9600 b/s
Parameters of the FAPC	**Value**
Total power limit	$P^*_{total,lim} = 1600$ W
Charging/discharging power limits of the battery converter	$P_{bat,uplim} = 450$ W, $P_{bat,lwlim} = -450$ W
Thresholds for the battery power control	$P_{th,nrrw} = 10$ W, $P_{th,wide} = 20$ W
Threshold to enable the PLC of multiple PV converters	$P_{PV,th} = 50$ W
Perturbation step-size of the PLC	$V_{step,PLC} = 2$ V
Control periods for the PRC[e]	$T_{P1} = 3$ s, $T_{P2} = 7$ s, $T_{MPO} = 20$ s
Fraction value when starting the MPPT in Periods I	$F_v = 0.78$
LPF to calculate $P_{PVk,avg}$ for the MPPT estimation	1-Hz rectangular window, $f_{s,LPF} = 200$ Hz[d]

[a]STC is the abbreviation of standard test condition.
[b]$k_{p,P}$, $k_{i,P}$, $k_{p,q}$, and $k_{i,q}$ are the proportional and integral gains for the *PQ* control, which have been introduced in Chapter 4.
[c]$k_{p,p,total}$, $k_{i,p,total}$, $k_{p,q,total}$ and $k_{i,q,total}$ are the proportional and integral gains of the total *PQ* loops, correspondingly.
[d]$f_{s,LPF}$ is the sampling frequency of the LPF.
[e]T_{P1}, T_{P2} and T_{MPO} is the duration of Periods I, II and the period of the *MPO_ENA* signals.

and PLC). Initially, the available power of PV#1 and #2 are 55% and 100% of their rated, respectively. Then, the available power of PV #1 steps up to 100%. As shown in Fig. 5.11, P_{PV1} quickly increases from 506 W to 920 W, while P_{total} slowly increases with a PRR being 40 W/s, until it reaches 1.6 kW, which is the required power limiting value.

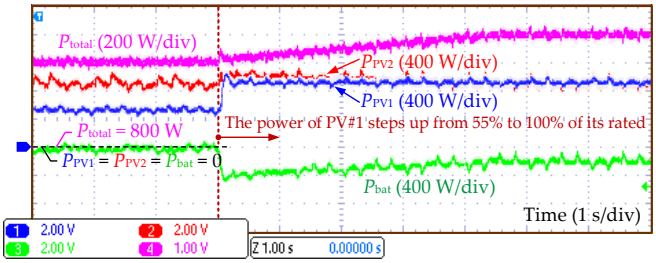

Fig. 5.11: PRRC (ramp-up) and PLC performance when the PV power steps up while the battery power and SoC are in the allowed limits (Case 1). Source: [**J4**].

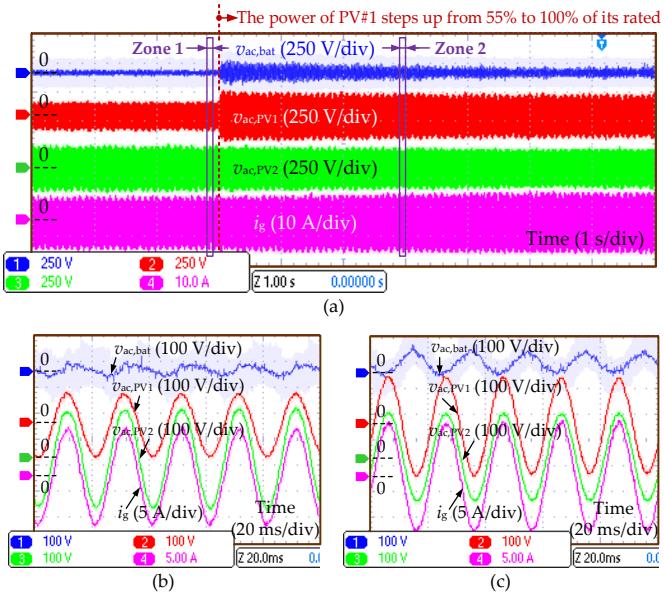

Fig. 5.12: Voltage response of each converter under the PRRC (ramp-up) and PLC (Case 1), when the PV power steps up: (a) AC voltage of each converter and the grid current, (b) and (c) zoomed-in figures of Zones 1 and 2 in Fig. 5.12(a), respectively. Source: [**J4**].

It can be observed that both the PRR and PLC constraints have been achieved with the proposed PRRC and PLC. The excessive power during the power ramp-up, and the steady-state excessive power beyond $P^{*}_{total,lim}$ (240 W), are all compensated by the battery converter. The power distribution among all converters can be confirmed by Fig. 5.12, where $v_{ac,bat}$ is quickly increased after the step up of PV power. In steady-state, $v_{ac,PV1}$ and $v_{ac,PV2}$ are in-phase with i_g, indicating that the two PV converters only inject active power to the grid; while $v_{ac,bat}$ is in opposite phase with i_g, indicating that the battery converter is absorbing power. Before and after the PV power step change, both PV voltages are around the MPP voltage, as shown in Fig. 5.13. In the entire process, the grid current i_g is kept stable, sinusoidal, and in-phase with v_g.

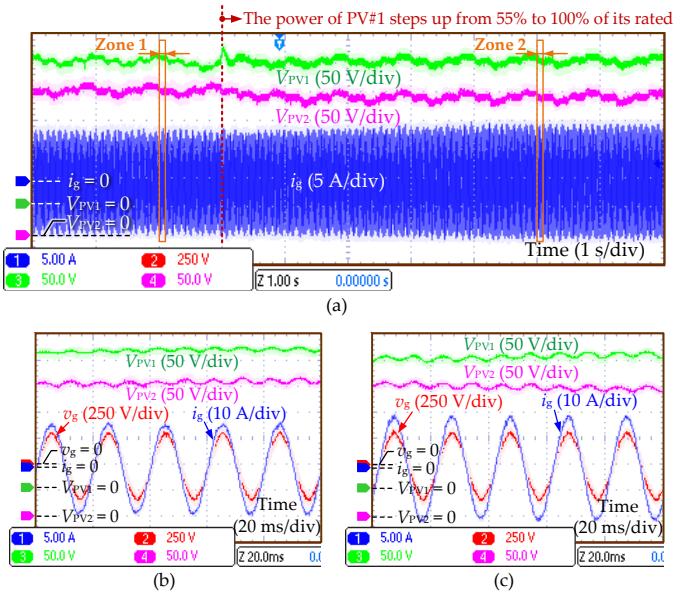

Fig. 5.13: Current and DC voltage responses of the system under the PRRC (ramp-up) and PLC (Case 1), when the PV power steps up: (a) two PV voltages and the grid current, (b) and (c) zoomed-in figures of Zones 1 and 2 in Fig. 5.13(a), respectively. Source: [**J4**].

Case 2: In this test, the PLC performance with different battery SoC conditions is demonstrated, and the experimental results are given in Figs. 5.14 and 5.15 (Mode 3 of the PLC). The initial condition of this test is identical with the steady-state condition of Case 1, and afterwards, the battery charging is disabled by setting $P_{bat,lwlim}$ as 0. As shown in Fig. 5.14, after disabling the battery charging, P_{bat} slowly increases from −240 W and oscillates around 0 in steady state. At the same time, each PV converter is curtailed by approximately 120-W power, while P_{total} is not affected, which remains constant at 1.6 kW. The PV voltages shown in Fig. 5.15 provide evidence to the PV power curtailment control, where V_{PV1} and V_{PV2} are increased to be around 285 V, being higher than the 261.5-V MPP voltage. The grid current i_g is stable during the entire process, which confirms a constant P_{total}.

Case 3: The performance of PRRC during power ramp-down is demonstrated in Figs. 5.16- 5.18, where the available power of PV #1 is reduced from 100% to 60% of its rated (Mode 1 of the PRRC). As shown in Fig. 5.16, after the reduction of P_{PV1}, P_{total} slowly decreases with a PRR being −40 W/s, while the battery converter only supports the active power during the power ramp-down, with its peak value being 360 W. Apart from the ramp-down period, P_{bat} is oscillating around zero, indicating the battery is neither charged nor discharged in steady state. The power contribution of each converter can be confirmed by its output AC voltage shown in Fig. 5.17, where the amplitude of $v_{ac,PV1}$ is decreased because of the reduction of PV power, while $v_{ac,bat}$ is only increased during the power ramp-down period. In steady state, the two PV

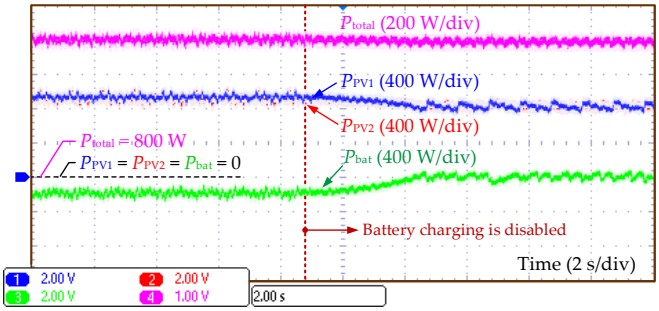

Fig. 5.14: Performance of the PLC with battery charging disabled (Case 2). Source: **[J4]**.

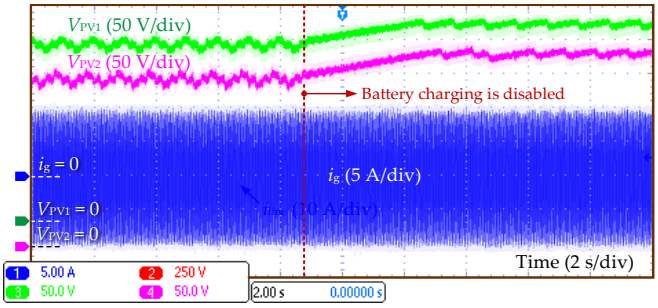

Fig. 5.15: Current and DC voltage responses of the system under the PLC with battery charging disabled (Case 2). Source: **[J4]**.

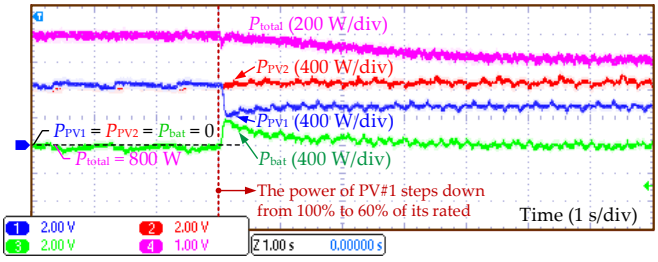

Fig. 5.16: Performance of the PRRC (ramp-down) when the PV power steps down (Case 3). Source: **[J4]**.

voltages are reduced from 285 V to be around 260 V, as shown in Fig. 5.18, which means that the MPPT control is activated for both PV converters again.

Case 4: Figs. 5.19 and 5.20 demonstrate the PRC performance. In the following test, $v_{step,PLC}$, $P_{th,nrrw}$ and $P_{th,wide}$ are increased to 6 V, 20 W and 30 W, respectively. In Stage I, $P^*_{total,res}$ is 0, and $P_{bat,lwlim}$ = −200 W. As shown in Fig. 5.19, a total power being 1.4 kW is generated by the series system, with P_{PV1} and P_{PV2} being 700 W and 680 W, respectively. Both PV converters are operating around their MPPs, as shown in Fig. 5.20(a), where both V_{PV1} and V_{PV2} are around 260 V. A small part of power being 20 W is provided by the battery converter due to the control dead-band P_{th}. Then, $P^*_{total,res}$ is increased to 100 W. As shown in Fig. 5.19, P_{total} slowly decreases to 1.3 kW with a PRR being

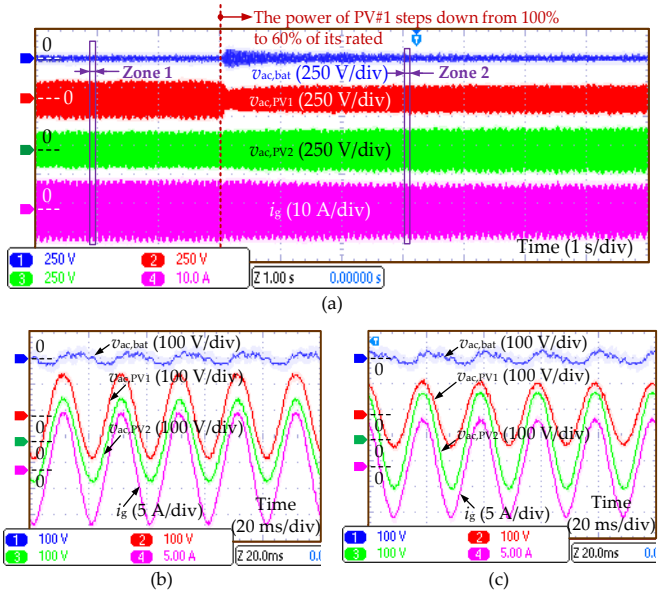

Fig. 5.17: AC voltage response of each converters under the PRRC (ramp-down) when the PV power steps down (Case 3): (a) AC voltages of individual converters and the grid current, (b) and (c) zoomed-in figures of Zone 1 and Zone 2 in Fig. 5.17(a). Source: **[J4]**.

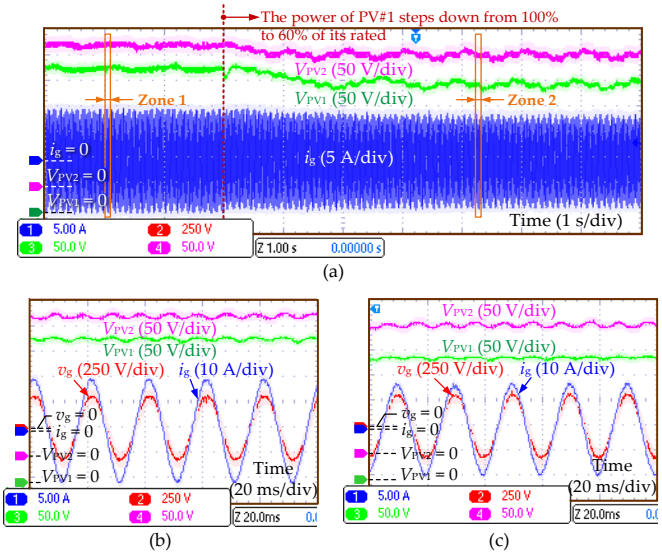

Fig. 5.18: Current and DC voltage responses of the system under the PRRC (ramp-down) when the PV power steps down (Case 3): (a) two PV voltages and the grid current, (b) and (c) zoomed-in figures of Zones 1 and 2 in Fig. 5.18(a). Source: **[J4]**.

−5.5 W/s, and the reserved power is fully absorbed by the battery (Mode 1). In Stage III, $P^*_{\text{total,res}}$ further increases to 300 W. Since $P^*_{\text{total,res}} > |P_{\text{bat,lwlim}}|$, the battery converter is

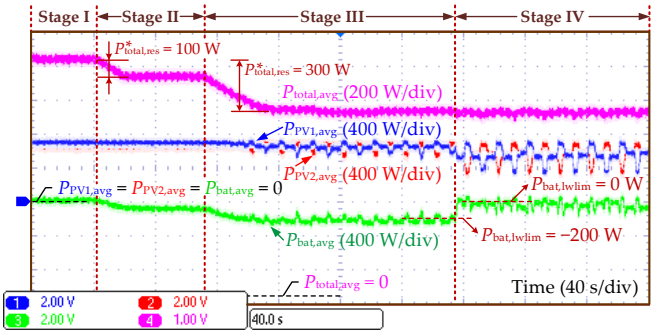

Fig. 5.19: Power reserve step response of the series-PV-battery system with different battery SoC conditions (Case 4). In Stage I, II, III, and IV, the required total power reserve is 0, 100 W, 300 W, and 300 W, respectively. The battery SoC is within its normal range in Stages I-III, and reaches its upper limit in Stage IV. Source: [**J4**].

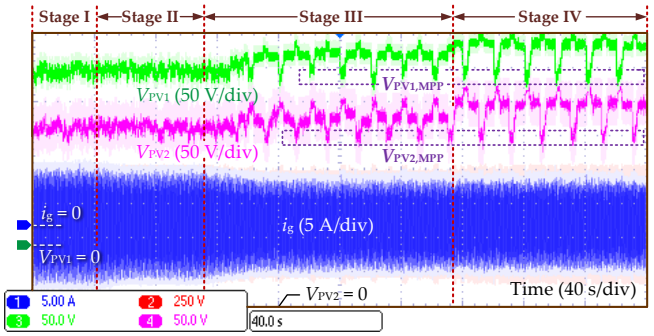

(a)

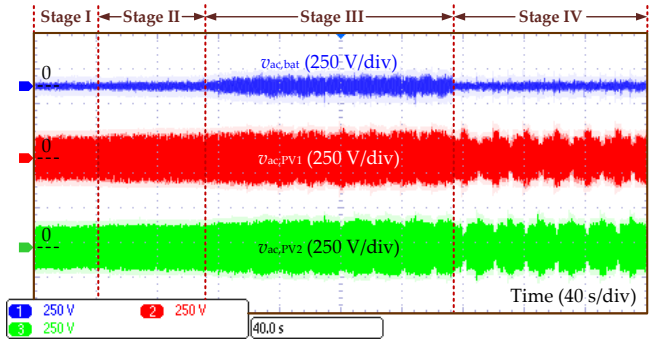

(b)

Fig. 5.20: Voltage and current response of the system under the PRC (Case 4): (a) two PV voltages and the grid current, and (b) AC voltage of each converter. Source: [**J4**].

charged with its maximum allowed power (200 W), while the remaining 100 W power is directly curtailed. As it can be noticed from Fig. 5.19, both P_{PV1} and P_{PV2} are curtailed to be around 640 W (Mode 2). In this stage, the two PV converters periodically switch their operation between the MPPT and the PLC modes, which can be confirmed by the

PV voltage waveforms in Fig. 5.20(a), where both V_{PV1} and V_{PV2} are around 260 V firstly, then increase to 280 V because of the PRC (Periods II), and further reach 300 V when the MPPT of the other PV converter is activated for the available power estimation.

In the final stage, $P_{bat,lwlim}$ is assigned as zero to disable battery charging. As a result, P_{bat} quickly increases and oscillate around zero, while the total 300-W power reserve is directly curtailed from the two PV converters, which are both curtailed to 540 W (Mode 3). Compared with the results in Stage III, the PV voltages are further increased to 295 V and 310 V in Periods II and III of both PV converters, respectively, which means that more PV power is curtailed. The periodical mode switching of PV converters can be clearly observed from Fig. 5.20(b), where the amplitudes of $v_{ac,PV1}$ and $v_{ac,PV2}$ also change in a three-stage manner, which are in accordance with the changes of P_{PV1} and P_{PV2} in Fig. 5.19, respectively.

Case 5: To demonstrate the performance of the PRC when PV power changes, experimental results are given in Figs. 5.21 and 5.22, where the conditions in Stage I are identical as the steady-state conditions of Case 4. Then, the available power of PV #1 is increased by 80 W. As shown in Figs. 5.21 and 5.22, the two PV converters routinely switch their operation from the MPPT mode, PLC mode, and further curtailed to assist the available power estimation of the other PV converter. In Stage II, the estimated $P_{PV1,avai}$ and $P_{PV2,avai}$ are 780 W and 680 W, respectively. Considering $P^*_{total,res}$ = 300 W, a total power reference being 1160 W can be calculated, being the same with the value of $P_{total,avg}$ in Stage II of Fig. 5.21. Both P_{PV1} and P_{PV2} are curtailed to be around 590 W, which is slightly larger than the desired $P^*_{PV,PLC}$ = 580 W calculated by (5.5). This small error is possibly due to the slow dynamics of the LPFs which are used to calculate the average power of PV converters. Nevertheless, the performance of the PRC performance is almost not affected by such small errors, as the small excessive power being only 20 W can easily be compensated by the battery.

In Stage III, $P_{PV1,avai}$ is decreased by 160 W. As shown in Fig. 5.21, $P_{total,avg}$ slowly ramps down with a PRR being −5.5 W/s, until it reaches 1.02 kW, which is slightly higher than the desired 1-kW power. This 20-W error is induced by the control dead-band P_{th}. The available power of the 1st and the 2nd PV converters is correctly estimated as 620 W and 680 W, respectively, and both PV converters are curtailed to 520 W in the PLC mode, with a small power being only −20 W absorbed by the battery converter to fulfil the requirement of $P^*_{total,res}$.

It can be noticed that P_{bat} is not strictly within the range of [$P_{bat,lwlim}$, $P_{bat,uplim}$] according to the experimental results in Figs. 5.19 and 5.21. This is mainly because of the low bandwidth of the PRC. In addition, since the battery should also compensate for transient power variations, the instantaneous value of P_{bat} can easily exceed the desired battery power range for a short while. Considering the above, sufficient margins should be reserved for the battery power capacity. Moreover, as it can be observed from Figs. 5.19 and 5.21, there are small steady-state errors in P_{total} and P_{bat}, which is induced by the control dead-band. As the errors are relatively small (1.25% of the system rated power), it is acceptable in practice. However, such error on P_{bat} can still lead to the cumulative charging or discharging of the battery. To avoid this, a simple hysteresis-control-based SoC self-balancing method can be employed [**J4**].

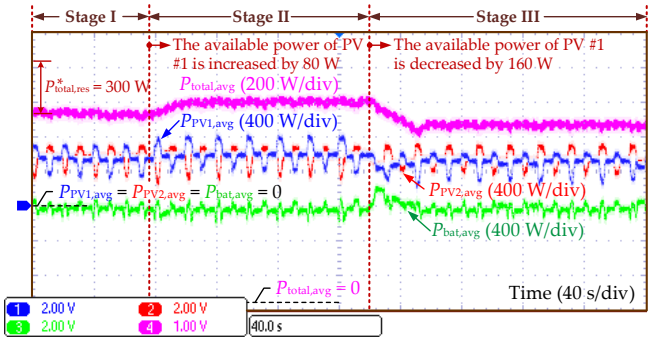

Fig. 5.21: Performance of the PRC under varying PV power (Case 5). Source: [**J4**].

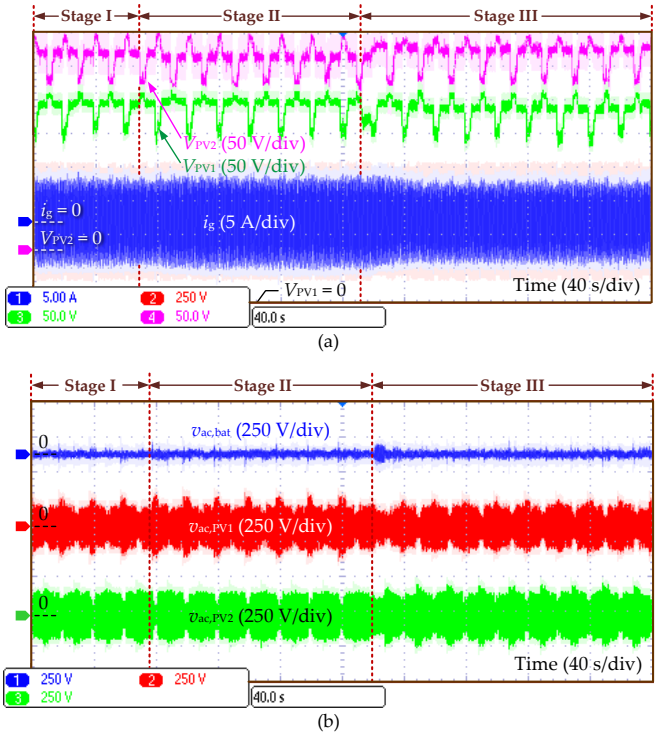

Fig. 5.22: Voltage and current response of the system in Case 5 of the experimental tests: (a) PV voltages and the grid current, and (b) AC voltages of individual converters. Source: [**J4**].

5.4. Summary

In this chapter, FAPC strategies (including the PRRC, PLC, and PRC) have been developed for grid-connected series-PV-battery systems. With the proposed strategies, individual converters are coordinatively controlled to fulfil the PRRC, PLC and PRC

requirements, while the power curtailment is assigned to individual converters considering a variety of constraints, including the available power of PV converters, battery charging/discharging power limits and SoC conditions, and the total power constraints from the upper grid layer control. With the proposed control strategy, the safe operation of the battery converter, load power balancing among PV converters, and high utilization of PV power can all be achieved.

The proposed PRRC and PLC strategies are mainly achieved by 1) modifying the MPPT control, 2) a hysteresis-based battery power control, and 3) the coordinated power curtailment of PV converters. The implementation of the proposed PRC is more complex, as it also requires the estimation of the available power of each PV converter. More specifically, when one PV converter is estimating its available power, all other converters should be coordinatively controlled to assist this converter observing its available power. The operation of each PV converter is divided into three stages: 1) the available power estimation stage (MPPT mode), 2) the power limiting stage to achieve the power reserve, and 3) the coordinatively controlled stage to assist the available power estimation of other PV converters. The implementation of the proposed PRRC, PLC and PRC strategies will not burden the LBC, as only a few control signals and variables are required, and all of them are of slow dynamics. Experimental results have validated the effectiveness of the proposed FAPC strategies.

Related Publications

J4. **Y. Pan**, A. Sangwongwanich, Y. Yang, X. Liu, M. Liserre, and F. Blaabjerg, "Flexible active power control of distributed photovoltaic systems with integrated battery using series converter configurations," *IEEE J. Emerg. Sel. Topi. Power Electron*., DOI: 10.1109/JESTPE.2021.3134203. Status: Early Access.

C6. **Y. Pan,** A. Sangwongwanich, Y. Yang, and F. Blaabjerg, "Flexible power control of distributed grid-connected series-photovoltaic-battery systems," in *Proc. IEEE APEC*, 2021, pp. 68-75.

Chapter 6.
Conclusion

6.1. Summary

This Ph.D. project was focused on advancing prior-art control schemes for better integration of distributed PV panels and batteries into distribution systems using series configurations. Challenging control issues for series-PV-battery systems, and the limitations of prior-art methods have been discussed, and solutions have been proposed to overcome these limitations. This Ph.D. thesis is summarized as follows:

In *Chapter 1*, conventional converter configurations to integrate distributed PV and battery units have been reviewed, as well as their advantages and limitations. Then, series topologies have been introduced, which can be promising for future PV-battery systems. To extend the application of series configurations, many efforts have been made to improve the performance of the output voltage/current/power, reduce the cost, and simplify the control of series systems. These efforts include developing appropriate modulation methods, power control methods, and distributed/decentralized control schemes. However, as most of them are not specifically developed for distributed PV-battery applications, they are not suitable for series-PV-battery systems. In addition, several essential issues remain unaddressed in series-PV-battery systems, such as interharmonics, overmodulation of individual converters, and the flexible active power control (FAPC) functions, further limiting the application of series-PV-battery systems. Thus, to tackle these issues and overcome the limitations in prior-art research, solutions have been developed in the following four chapters.

As for the modulation for series-PV-battery systems, the variable angle phase-shifting (VAPS) PWM method based on mathematical searching algorithms has been firstly introduced in *Chapter 2*. The VAPS PWM method aims at minimizing the high-frequency harmonics when the outputs of individual converters are nonidentical, being one of the most suitable modulation methods for distributed series-PV-battery systems. However, it generally takes hundreds of milliseconds with a common standard digital signal processor (DSP) to calculate the optimal carrier phase-shifting (PS) angles for the VAPS PWM method. During the period when the optimal angles are not calculated, the total harmonic distortion (THD) performance of the system can be degraded. Thus, to improve the optimization speed, a hardware-based approach for the VAPS PWM method has been proposed, where a few calculation units are implemented in field programmable gate arrays (FPGAs). By doing so, multiple computations can be executed in parallel, and the dynamic performance of the VAPS PWM method can be significantly improved, being dozens of times faster than the

DSP-based method. The proposed computation-efficient VAPS PWM method can also be easily applied to series systems with more cascaded converters.

In *Chapter 3*, the interharmonic issue in cascaded H-bridge (CHB) PV converters has been discussed, which occurs due to the in-phase MPPT perturbation of individual converters. To mitigate interharmonics, a phase-shifting MPPT (PS-MPPT) scheme has been proposed, which adjusts the phase-angles of the DC-side oscillations for individual converters in a way to counteract with each other. With this approach, interharmonics due to the in-phase MPPT control can be fully eliminated for CHB PV converters with an even cascaded number. To further suppress interharmonics from CHB PV converters with an odd cascaded number, a hybrid PS-MPPT method has been proposed, where the PS-MPPT and the random sampling-rate MPPT methods are simultaneously applied to different converter cells. The interharmonic suppression performance of the random sampling-rate MPPT method has also been investigated and being another cost-effective solution to mitigate interharmonics. The above methods are all based on the modification of conventional MPPT algorithms, avoiding the equipment of additional energy storage units to mitigate interharmonics. Considering that the PS-MPPT and the random sampling-rate MPPT methods are either compromised in the dynamic and steady-state interharmonic suppression performance, respectively, a hardware-based approach − the "interharmonic filter" has been proposed. With an additional converter only with capacitors on its DC link, interharmonics from CHB PV converters due to the MPPT perturbation can be completely mitigated. In practice, the interharmonic filter can also be selected among the PV converter cells, avoiding further costs of the additional converter.

Although various distributed/decentralized control schemes have been developed for series systems, they are either highly dependent on the real-time communication, or only suitable for limited operation conditions (e.g., equal power sharing with identical power factors among all converters). In addition, the reactive power sharing among all converters and the anti-overmodulation (AOM) of individual converters have rarely been studied. Thus, a distributed control architecture has been developed for islanding series-PV-battery systems in *Chapter 4*, which is less-dependent on communication. The proposed control scheme includes the *PQ* decoupling control of each PV converter, droop control of the battery converter, a reactive power distribution strategy with low communication requirements, and the AOM control for all converters. With the *PQ* decoupling control, individual converters can be self-synchronized with the series system using only local measurements, regardless of their power factor (PF) conditions. The battery converter compensates for the difference between the PV power generation and the load power following the desired droop curves, enabling the system to regulate the voltage and frequency of the islanding grid. Reactive power is shared by all converters in a way to balance their loadings, alleviating the overmodulation and overloading risks of certain converters. Two AOM control loops have been designed for individual PV and battery converters, achieved by curtailing a part of PV power. The proposed distributed control scheme can be achieved with low communication requirements, through which only a few variables and control signals with low band-width should be transmitted.

Based on the distributed control architecture for series-PV-battery systems in *Chapter 4*, flexible active power control (FAPC) strategies have been further developed in *Chapter 5*, including the power ramp-rate control (PRRC), power limiting control (PLC), and power reserve control (PRC) strategies. Different from prior-art FAPC strategies which are mainly focused on single-inverter systems, in the proposed strategies, multiple converters are coordinatively controlled considering a variety of constraints. These constraints include the battery charging/discharging power limits and SoC conditions, the available PV power of each converter, total PRRC, PLC and PRC constraints, and the requirements for estimating the available PV power. With the above, the FAPC constraints can be maintained, while the curtailed/reserved power of the system is properly distributed among all converters, ensuring a balanced power sharing performance, and reducing the overmodulation/overloading risks of certain converters.

6.2. Main Contributions

The main contributions of this Ph.D. project can be summarized as:

- **Computation-efficient VAPS PWM method**

  A computation-efficient VAPS PWM method has been developed and verified experimentally in this Ph.D. study. With the parallel computing in FPGAs, the optimization of the conventional DSP-based VAPS PWM method can be improved dozens of times faster, and significantly improves the response speed of VAPS PWM methods.

- **Interharmonic mitigation for CHB PV converters**

  A PS-MPPT scheme has been proposed to mitigate interharmonics from CHB PV converters induced by the in-phase MPPT perturbations of individual converter cells, achieved by synchronizing and phase-shifting the DC-side oscillations of all PV converters. Based on the PS-MPPT method, the following methods have been further developed and investigated:

  1) The hybrid PS-MPPT method to further suppress interharmonics from CHB PV converters with an odd cascaded number.

  2) The random sampling-rate MPPT method for CHB PV converters to suppress interharmonics in dynamic conditions (e.g., under varying solar irradiance).

  3) A "interharmonic filter" approach to compensate interharmonics regardless of the MPPT conditions (i.e., DC-side oscillation conditions) of all PV converters.

  The effectiveness of all these methods has been validated by either simulations or experimental results.

- **Distributed control method for islanded series-PV-battery systems with low communication requirements**

  A distributed control scheme for islanded series-PV-battery systems have been proposed to achieve 1) self-synchronization of individual converters, 2) regulating the frequency and voltage of the islanding grid, 3) apparent power balancing among all converters, and 4) AOM control for all converters. Correspondingly, the following methods have been developed:

  1) *PQ* decoupling control for individual converters and droop control for a battery converter
  2) Two reactive power distribution strategies
  3) AOM control for PV and battery converters based on the coordinated PV power curtailment

  Experiments have been conducted for validating the effectiveness of the proposed control, which can be achieved with very low communication requirements. In addition, a small signal model of the series-PV-battery system under the proposed control has also been developed to analyze the stability performance and help tuning the parameters of the control loops.

- **FAPC methods for grid-connected series-PV-battery systems**

  As FAPC functions are becoming mandatory for PV systems, FAPC strategies for series-PV-battery systems have also been developed during the Ph.D. study, including the PRRC, PLC, and PRC. The above strategies are achieved through a coordinative control of all converters, where the curtailed power is shared among them considering 1) the battery charging/discharging limits and SoC limits, 2) the available PV power of each converter, 3) the total PRRC, PLC and PRC constraints, and 4) the requirements to estimate the available power of individual converters. The effectiveness of all these proposed FAPC strategies have been experimentally verified.

6.3. Future Research Perspectives

Control-related issues for series-PV-battery systems have been addressed in this Ph.D. project in terms of the modulation, interharmonic mitigation, distributed control, and the flexible power control of the system. However, many issues remain to be resolved, as listed in the following:

- Although the optimization speed of the VAPS PWM method can be accelerated by the proposed FPGA-based approach, it is still limited by available hardware resources, e.g., FPGA size and communication bus width. According to the experimental results, the THD of the output multilevel voltage can still be degraded for a short period (less than one fundamental cycle) using the

proposed computation-efficient VAPS PWM method. Due to this, the output AC filters should still be overdesigned to improve the output harmonic performance. Thus, in the future, more efforts can be made to accelerate the optimization speed, including 1) employing a wider parallel bus, 2) incorporating all the PSO algorithm in FPGAs, and 3) optimizing the circuit layout in FPGAs. By doing so, the reduction of the AC filter size can be possible due to the bandwidth extension of the VAPS PWM methods.

- Regarding the distributed control and FAPC of series-PV-battery systems, only the control of short time scales (millisecond to minute levels) has been studied and experimentally verified. Control and planning issues of longer time scales have not been investigated:

  1) In the proposed strategies, the system follows the power scheduling commands from the grid control layer, but how to determine these commands has not been discussed (the interaction with the grid control layer).

  2) The battery SoC condition is simply considered as one control constraint in the proposed strategies. Nevertheless, how the operation of the system with the FAPC affects the battery SoC and state-of-health (SoH) has not been investigated.

  3) Batteries are used to solve the conflicts between maintaining the total power constraint and maximizing PV power yield. However, how to maximize the total benefits by allocating batteries with appropriate capacity remain undiscussed.

  4) As individual converters are usually unevenly loaded, they will have different aging profiles, which can affect the reliability performance of the entire system. However, the reliability assessment, and power routing strategies to enhance the reliability of the entire system have not been studied.

  Thus, it calls for further studies on the system behavior under longer time scales (hour / day / month levels), which include: 1) mission profile analysis of both PV and battery converters, 2) reliability assessment of the entire system, 3) developing appropriate strategies to interact with the grid control layer, 4) proposing design criteria for determining the battery capacity to maximize the benefits, and 5) developing power routing strategies to enhance the reliability of the entire system.

- In the proposed distributed control scheme, individual converters can be self-synchronized with others. However, as the self-synchronization is based on a power measurement, it is challenging to synchronize all converters during the start-up, when the line current is not established. On the other hand, it is also not suitable to rely on the communication for the start-up, as individual converters may not start simultaneously due to the communication delay. In the experimental tests of this Ph.D. project, all converters have been synchronized

with a common start-up signal during the start-up for simplification. Thus, how to synchronize individual converters during the start-up process, and then to develop appropriate start-up strategies for series systems are needed.

- Due to the removal of the DC/DC boost conversion stage, one advantage of single-stage series configurations is the improved efficiency. Nevertheless, the efficiency of the series system has not been studied in this project. As the employment of the VAPS PWM method may improve the efficiency of the entire system, it could be interesting to evaluate the converter efficiency under the proposed VAPS PWM method (including both the conventional DSP-based and the FPGA-based methods). Moreover, the reactive power can also be distributed among all converters to optimize the overall efficiency of the system. These topics are expected to be studied in the future.
- Compared with conventional parallel structures, series systems have limited fault-tolerant capability, as the malfunctions of any converter cells will affect the operation of the entire system. Although the fault-tolerant control methods against the semiconductor fault have been studied previously for series-converter systems, they have not been systematically evaluated for series-PV-battery systems. In fact, fault tolerant control issues in series-PV-battery systems are more complex. For instance, when PV panels are plugged into the DC rails, the criteria for identifying the fault (e.g., through analyzing the operating waveforms of the line current) can be different from previous studies, where only ideal DC sources or only capacitors have been considered in the DC side. Moreover, the MPPT operation of PV converters will also be affected under semiconductor faults. Therefore, the fault tolerant control of series-PV-battery systems requires further investigation.
- Only single-phase systems have been considered in this Ph.D. project. It can be interesting to extend the proposed methods to three-phase systems, where the conditions can be more complex. To list a few:

  1) The optimization of the high-frequency harmonics in three-phase line voltages (inter-phase voltages) can be more complex than the optimization of the phase voltage in single-phase systems.

  2) Configurations of series-PV-battery systems can be more flexible in three-phase systems, bring more complexities in developing appropriate control strategies (e.g., a lumped three-phase inverter can be employed to integrate the battery, while PV panels are still interfaced to individual H-bridge converters).

  3) Three-phase power quality issues are more complex than single-phase systems (e.g., three-phase unbalance of the grid voltage and PV power generation, three-phase short-circuit faults).

Bibliography

References

[1] F. Blaabjerg, Y. Yang, D. Yang, and X. Wang. "Distributed power-generation systems and protection," *Proc. IEEE*, vol. 105, no. 7, pp. 1311–1331, July. 2017.

[2] H. E. Murdock, D. Gibb, T. Andre, J. L. Sawin, A. Brown, L. Ranalder, U. Collier, C. Dent, B. Epp, C. H. Kumar, et al., *Renewables 2021: Global Status Report*, REN21 Secretariat, Paris, France, Rep. REN21.2021, 2021. [Online]. Available: https://www.ren21.net/.

[3] IEA and PVPS, "Trends in photovoltaic applications: Task 1 strategic PV analysis and outreach," Surv. Rep. IEA-PVPS T1-41, 2021. [Online]. Available: https://iea-pvps.org/.

[4] ISE Fraunhofer, "Photovoltaics report," Fraunhofer ISE, Freiburg, Germany, 2021. [Online]. Available: https://www.ise.fraunhofer.de/.

[5] N. Dodd, N. Espinosa, P. Van Tichelen, K. Peeters, and A. Soares, ''Preparatory study for solar photovoltaic modules, inverters and systems,'' Publ. Office Eur. Union, Luxembourg, Tech. Rep. EUR 30468 EN, 2020.

[6] Y. Yang, K. A. Kim, F. Blaabjerg, and A. Sangwongwanich, *Advances in Grid-Connected Photovoltaic Power Conversion Systems*, Publisher: Woodhead Publishing, 2018.

[7] K. Alluhaybi, I. Batarseh, and H. Hu, "Comprehensive review and comparison of single-phase grid-tied photovoltaic microinverters," *IEEE J. Emerg. Sel. Top. Power Electron*, vol. 8, no. 2, pp. 1310-1329, Jun. 2020.

[8] X. Zhang, T. Zhao, W. Mao, D. Tan, and L. Chang, "Multilevel inverters for grid-connected photovoltaic applications: Examining emerging trends," *IEEE Power Electron. Mag*., vol. 5, no. 4, pp. 32-41, Dec. 2018.

[9] S. B. Kjaer, J. K. Pedersen, and F. Blaabjerg. "A review of single-phase grid-connected inverters for photovoltaic modules," *IEEE Trans. Ind. Appl*., vol. 41, no. 5, pp. 1292–1306, Sep.-Oct. 2005.

[10] H. Mahmood, D. Michaelson, and J. Jiang, "Strategies for independent deployment and autonomous control of PV and battery units in islanded microgrids," *IEEE J. Emerg. Sel. Top. Power Electron*., vo. 3, no. 2, pp.742-755, Sep. 2015.

[11] A. K. Bhattacharjee, N. Kutkut, and I. Batarseh, "Review of multiport converters for solar and energy storage integration," *IEEE Trans. Power Electron*., vol. 34, no. 2, pp. 1431-1445, Feb. 2019.

[12] L. Maharjan, T. Yamagishi, H. Akagi, and J. Asakura, "Fault-tolerant operation of a battery-energy-storage system based on a multilevel cascade PWM converter with star configuration," *IEEE Trans. Power Electron*., vol. 25, no. 9, pp. 2386-2396, Sept. 2010.

[13] N. Li, F. Gao, T. Hao, Z. Ma, and C. Zhang, "SOH balancing control method for the MMC battery energy storage system," *IEEE Trans. Ind. Electron*., vol. 65, no. 8, pp. 6581-6591, Aug. 2018.

[14] B. Xu, H. Tu, Y. Du, H. Yu, H. Liang, and S. Lukic, "A distributed control architecture for cascaded H-bridge converter with integrated battery energy storage," *IEEE Trans. Ind. Appl*., vol. 57, no. 1, pp. 845-856, Jan.-Feb. 2021.

[15] W. Jiang, S. Xue, L. Zhang, W. Xu, K. Yu, W. Chen, and L. Zhang, "Flexible power distribution control in an asymmetrical-cascaded-multilevel-converter-based hybrid energy storage system," *IEEE Trans. Ind. Electron*., vol. 65, no. 8, pp. 6150-6159, Aug. 2018.

[16] E. Wesoff, "Batteries under solar modules just like microinverters and optimizers," *PV Mag*., Feb. 2020.

[17] W. Liang, Y. Liu, and J. Peng, "A day and night operational quasi-Z source multilevel grid-tied PV power system to achieve active and reactive power control," *IEEE Trans. Power Electron*., vol. 36, no. 1, pp. 474-492, Jan. 2021.

[18] H. Wu, L. Zhu, F. Yang, T. Mu, and H. Ge, "Dual-DC-port asymmetrical multilevel inverters with reduced conversion stages and enhanced conversion efficiency," *IEEE Trans. Ind. Electron*., vol. 64, no. 3, pp. 2081-2091, Mar. 2017.

[19] J. Zeng, T. Kim, and V. Winstead, "A soft-switched four-port DC-DC converter for renewable energy integration," in *Proc. IEEE ECCE*, Sep. 2018, pp. 5851–5856.

[20] X. Zhang, M. Wang, T. Zhao, W. Mao, Y. Hu, and R. Cao, "Topological comparison and analysis of medium-voltage and high-power direct-linked PV inverter," *CES Trans. Elect. Mach. Syst*., vol. 3, no. 4, pp. 327–334, Dec. 2019.

[21] E. Villanueva, P. Correa, J. Rodríguez and M. Pacas, "Control of a single-phase cascaded H-bridge multilevel inverter for grid-connected photovoltaic systems," *IEEE Trans. Ind. Electron*., vol. 56, no. 11, pp. 4399-4406, Nov. 2009.

[22] L. Liu, H. Li, Y. Xue, and W. Liu, "Decoupled active and reactive power control for large-scale grid-connected photovoltaic systems using cascaded modular multilevel converters," *IEEE Trans. Power Electron*., vol. 30, no. 1, pp. 176-187, Jan. 2015.

[23] B. Xiao, L. Hang, J. Mei, C. Riley, L. M. Tolbert, and B. Ozpineci, "Modular cascaded H-bridge multi-level PV inverter with distributed MPPT for grid-connected applications," *IEEE Trans. Ind. Appl*., vol. 51, no. 2, pp. 1722–1732, Mar.-Apr. 2015.

[24] H. Jafarian, S. Bhowmik, and B. Parkhideh. "Hybrid current-/voltage-mode control scheme for distributed AC-stacked PV inverter with low-bandwidth communication requirements," *IEEE Trans. Ind. Electron*., vol. 65, no. 1, pp. 321-330, Jan. 2018.

[25] Y. Yu, G. Konstantinou, B. Hredzak, and V.G. Agelidis, "Power balance of cascaded H-bridge multilevel converters for large scale photovoltaic integration," *IEEE Trans. Power Electron*., vol. 31, no. 1, pp. 292-303, Jan. 2016.

[26] C. Wang, K. Zhang, J. Xiong, Y. Xue, and W. Liu, "A coordinated compensation strategy for module mismatch of CHB-PV systems based on improved LS-PWM and reactive power injection," *IEEE Trans. Ind. Electron*., vol. 66, no. 4, pp. 2825-2836, Apr. 2019.

[27] F. Lu, B. Choi, and D. Maksimovic, "Autonomous power-source regulation in series-connected low-voltage microinverters," *IEEE J. Emerg. Sel. Top. Power Electron*., vol. 8, no. 2, pp. 1442-1453, Jun. 2020.

[28] J. He, Y. Li, B. Liang, and C. Wang, "Inverse power factor droop control for decentralized power sharing in series-connected-microconverters-based islanding microgrids," *IEEE Tran. Ind. Electron*., vol. 64, no. 9, pp. 7444-7454, Sept. 2017.

[29] X. Hou, Y. Sun, H. Han, Z. Liu, W. Yuan, and M. Su, "A fully decentralized control of grid-connected cascaded inverters," *IEEE Tran. Sustain. Energy*, vol. 10, no. 1, pp. 315-317, Jan. 2019.

[30] P.-H. Wu, Y.-C. Su, J.-L. Shie, and P.-T. Cheng, "A distributed control technique for the multilevel cascaded converter," *IEEE Trans. Ind. Appl*., vol. 55, no. 2, pp. 1649-1657, Mar.-Apr. 2019.

[31] L. Liu, H. Li, Y. Xue, and W. Liu, "Reactive power compensation and optimization strategy for grid-interactive cascaded photovoltaic systems," *IEEE Trans. Power Electron*., vol. 30, no. 1, pp. 188-202, Jan. 2015.

[32] M. Miranbeigi and H. Iman-Eini, "Hybrid modulation technique for grid-connected cascaded photovoltaic systems," *IEEE Trans. Ind. Electron*., vol. 63, no. 12, pp. 7843-7853, Dec. 2016.

[33] T. Zhao, X. Zhang, W. Mao, F. Wang, J. Xu, Y. Gu, and X. Wang., "An optimized third harmonic compensation strategy for single-phase cascaded H-bridge photovoltaic inverter," *IEEE Trans. Ind. Electron*., vol. 65, no. 11, pp. 8635-8645, Nov. 2018.

[34] Y. Yu, G. Konstantinou, B. Hredzak, and V. G. Agelidis, "Operation of cascaded H-bridge multilevel converters for large-scale photovoltaic power plants under bridge failures," *IEEE Trans. Ind. Electron*., vol. 62, no. 11, pp. 7228-7236, Nov. 2015.

[35] S. Kim, J. Lee, and K. Lee, "A modified level-shifted PWM strategy for fault-tolerant cascaded multilevel inverters with improved power distribution," *IEEE Trans. Ind. Electron*., vol. 63, no. 11, pp. 7264-7274, Nov. 2016.

[36] J. He, Y. W. Li, C. Wang, Y. Pan, C. Zhang, and X. Xing, "Hybrid microgrid with parallel and series connected micro-converters," *IEEE Trans. Power Electron*., vol. 33, no. 6, pp. 4817-4831, Jun. 2018.

[37] Y. Pan, C. Zhang, S. Yuan, A. Chen, and J. He, "A decentralized control method for series connected PV battery hybrid microgrid," in *Proc. ITEC Asia-Pacific*, Aug. 2017, pp. 1-6.

[38] Q. Zhang and K. Sun, "A flexible power control for PV-battery-hybrid system using cascaded H-bridge converters," *IEEE J. Emerg. Sel. Top. Power Electron*., vol. 7, no. 4, pp. 2184-2195, Dec. 2019.

[39] L. Liu, H. Li, Z. Wu, and Y. Zhou, "A cascaded photovoltaic system integrating segmented energy storages with self-regulating power allocation control and wide range reactive power compensation," *IEEE Trans. on Power Electron*., vol. 26, no. 12, pp. 3545-3559, Dec. 2011.

[40] N. Kim and B. Parkhideh, "Control and operating range analysis of an AC-stacked PV inverter architecture integrated with a battery," *IEEE Trans. Power Electron*., vol. 33, no. 12, pp. 10032-10037, Dec. 2018.

[41] H. Liao, X. Zhang, and X. Hou, "A decentralized control of series-connected PV-ES inverters with MPPT and virtual inertia functionality," in *Proc. IEEE APEC Expo*., Mar. 2020, pp. 3221-3224.

[42] S. Das, I. U. Nutkani, and C. Teixeira, "Autonomous power management of series-parallel hybrid microgrid," in *Proc. IEEE ICPES*, 2019, pp. 1-6.

[43] B. P. McGrath and D. G. Holmes, "Multicarrier PWM strategies for multilevel inverters," *IEEE Trans. Ind. Electron*., vol. 49, no. 4, pp. 858-867, Aug. 2002.

[44] Y. Li, Y. Wang, and B. Q. Li, "Generalized theory of phase-shifted carrier PWM for cascaded H-bridge converters and modular multilevel converters," *IEEE J. Emerg. Sel. Top. Power Electron*., vol. 4, no. 2, pp. 589-605, Jun. 2016.

[45] P. Sochor and H. Akagi, "Theoretical and experimental comparison between phase-shifted PWM and level-shifted PWM in a modular multilevel SDBC inverter for utility-scale photovoltaic applications," *IEEE Trans. Ind. Appl*., vol. 53, no. 5, pp. 4695-4707, Sept.-Oct. 2017.

[46] M. Angulo, P. Lezana, S. Kouro, J. Rodriguez, and B. Wu, "Level-shifted PWM for cascaded multilevel inverters with even power distribution," in *Proc. IEEE PESC*, 2007, pp. 2373-2378.

[47] J. Chavarria, D. Biel, F. Guinjoan, C. Meza, and J. J. Negroni, "Energy-balance control of PV cascaded multilevel grid-connected inverters under level-shifted

and phase-shifted PWMs," *IEEE Trans. Ind. Electron*., vol. 60, no. 1, pp. 98-111, Jan. 2013.

[48] J. I. Leon, S. Vazquez, A. J. Watson, L. G. Franquelo, P. W. Wheeler, and J. M. Carrasco, "Feed-forward space vector modulation for single-phase multilevel cascaded converters with any DC voltage ratio," *IEEE Trans. Ind. Electron*., vol. 56, no. 2, pp. 315-325, Feb. 2009.

[49] Y. M. Park, J. Y. Yoo, and S. B. Lee. "Practical implementation of PWM synchronization and phase-shift method for cascaded H-bridge multilevel inverters based on a standard serial communication protocol," *IEEE Trans. Ind. Appl*., vol. 44, no. 2, pp. 634-643, Mar.-Apr. 2008.

[50] L. Du and J. He, "A simple autonomous phase-shifting PWM approach for series-connected multi-converter harmonic mitigation," *IEEE Trans. Power Electron*., vol. 34, no. 12, pp. 11516-11520, Dec. 2019.

[51] J. He, X. Liu, M. Lei, and C. Wang, "A broad frequency range harmonic reduction for cascaded-power-cell-based islanded microgrid with lumped PCC filter," *IEEE Trans. Power Electron*., vol. 35, no. 9, pp. 9251-9266, Sept. 2020.

[52] A. Marquez, J. I. Leon, S. Vazquez, R. Portillo, L. G. Franquelo, E. Freire, and S. Kouro, "Variable-angle phase-shifted PWM for multilevel three-cell cascaded H-bridge converters," *IEEE Trans. Ind. Electron*., vol. 64, no. 5, pp. 3619-3628, May 2017.

[53] V. G. Monopoli, Y. Ko, G. Buticchi, and M. Liserre, "Performance comparison of variable-angle phase-shifting carrier PWM techniques," *IEEE Trans. Ind. Electron*., vol. 65, no. 7, pp. 5272-5281, July 2018.

[54] A. M. Alcaide, J. I. Leon, R. Portillo, J. Yin, W. Luo, S. Vazquez, S. Kouro, and L. G. Franquelo, "Variable-angle PS-PWM technique for multilevel cascaded H-bridge converters with large number of power cells," *IEEE Trans. Ind. Electron*., vol. 68, no. 8, pp. 6773-6783, Aug. 2021.

[55] P. Liu and S. Duan, "Derivation of the generalized phase-shifted angles by using phasor diagrams for the CHB converter with unbalanced DC voltage sources," *IEEE Trans. Ind. Electron*., vol. 68, no. 12, pp. 12002-12009, Dec. 2021.

[56] A. Marquez, J. I. Leon, V. G. Monopoli, S. Vazquez, M. Liserre, and L. G. Franquelo, "Generalized harmonic control for CHB converters with unbalanced cells operation," *IEEE Trans. Ind. Electron*., vol. 67, no. 11, pp. 9039-9047, Nov. 2020.

[57] T. Xu and F. Gao, "Global Synchronous Pulse Width Modulation of Distributed Inverters," *IEEE Trans. Power Electron*., vol. 31, no. 9, pp. 6237-6253, Sept. 2016.

[58] A. Sangwongwanich, Y. Yang, D. Sera, H. Soltani, and F. Blaabjerg, "Analysis and modeling of interharmonics from grid-connected photovoltaic systems," *IEEE Trans. Power Electron*., vol. 33, no. 10, pp. 8353-8364, Oct. 2018.

[59] R. Langella, A. Testa, J. Meyer, F. Mller, R. Stiegler, and S. Z. Djokic, "Experimental-based evaluation of PV inverter harmonic and interharmonic distortion due to different operating conditions," *IEEE Trans. Instrum. Meas*., vol. 65, no. 10, pp. 2221-2233, Oct. 2016.

[60] V. Ravindran, S. K. Rönnberg, and M. H. J. Bollen, "Interharmonics in PV systems: a review of analysis and estimation methods; considerations for selection of an apt method," *IET Renew. Power Gener*., vol. 13, no. 12, pp. 2023-2032, Sept. 2019.

[61] V. Ravindran, T. Busatto, S. K. Ronnberg, J. Meyer, and M. Bollen, "Time-varying interharmonics in different types of grid-tied PV inverter systems," *IEEE Trans. Power Del*., vol. 35, no. 2, pp. 483-496, April 2020.

[62] *IEEE Standard for Interconnection and Interoperability of Distributed Energy Resources with Associated Electric Power Systems Interfaces*, IEEE Standard 1547-2018, Apr. 2018.

[63] *Grid code compliance assessment methods for grid connection of wind and PV power plants*, Ed. 1, IEC/TS 63102, 2016.

[64] A. Sangwongwanich and F. Blaabjerg, "Mitigation of interharmonics in PV systems with maximum power point tracking modification," *IEEE Trans. Power Electron*., vol. 34, no. 9, pp. 8279-8282, Sept. 2019.

[65] A. Sangwongwanich, Y. Yang, D. Sera, and F. Blaabjerg, "Interharmonics from grid-connected PV systems: mechanism and mitigation," in *Proc. IEEE IFEEC-ECCE Asia*, Jun. 2017, pp. 722–727.

[66] L. Zhang, K. Sun, Y. W. Li, X. Lu, and J. Zhao, "A distributed power control of series-connected module-integrated inverters for PV grid-tied applications," *IEEE Trans. Power Electron*., vol. 33, no. 9, pp. 7698-7707, Sept. 2018.

[67] Y. Sun, G. Shi, X. Li, W. Yuan, M. Su, H. Han, and X. Hou, "An f-P/Q droop control in cascaded-type microgrid," *IEEE Trans. Power Syst*., vol. 33, no. 1, pp. 1136-1138, Jan. 2018.

[68] Y. Sun, L. Li, G. Shi, X. Hou, and M. Su, "Power factor angle droop control−a general decentralized control of cascaded inverters," *IEEE Trans. Power Del*., vol. 36, no. 1, pp. 465-468, Feb. 2021.

[69] X. Hou, Y. Sun, H. Han, Z. Liu, M. Su, B. Wang, and X. Zhang, "A general decentralized control scheme for medium-/high-voltage cascaded STATCOM," *IEEE Trans. Power Syst*., vol. 33, no. 6, pp. 7296-7300, Nov. 2018.

[70] L. Li, Y. Sun, H. Han, G. Shi, M. Su, and M. Zheng, "A decentralized control for cascaded inverters in grid-connected applications," *IEEE Trans. Ind. Electron*., vol. 67, no. 9, pp. 8064-8071, Sept. 2020.

[71] H. Jafarian, R. Cox, J. H. Enslin, S. Bhowmik and B. Parkhideh, "Decentralized active and reactive power control for an AC-stacked PV inverter with single member phase compensation," *IEEE Trans. Ind. Appl*., vol. 54, no. 1, pp. 345-355, Jan.-Feb. 2018.

[72] H. D. Tafti, A. Sangwongwanich, Y. Yang, J. Pou, G. Konstantinou, and F. Blaabjerg, "An adaptive control scheme for flexible power point tracking in photovoltaic systems," *IEEE Trans. Power Electron*., vol. 34, no. 6, pp. 5451-5463, Jun. 2019.

[73] A. Sangwongwanich, Y. Yang, F. Blaabjerg, and H. Wang, "Benchmarking of constant power generation strategies for single-phase grid-connected photovoltaic systems," *IEEE Trans. Ind. Appl*., vol. 54, no. 1, pp. 447-457, Jan.-Feb. 2018.

[74] H. D. Tafti, G. Konstantinou, J. E. Fletcher, G. G. Farivar, S. Ceballos, J. Pou, and C. D. Townsend, "Flexible power point tracking in cascaded H-bridge converter-based photovoltaic systems," in *Proc. IEEE IECON*., Oct. 2020, pp. 1826-1830.

[75] H. D. Tafti, A. I. Maswood, G. Konstantinou, C. D. Townsend, P. Acuna, and J. Pou, "Flexible control of photovoltaic grid-connected cascaded H-bridge converters during unbalanced voltage sags," *IEEE Trans. Ind. Electron*., vol. 65, no. 8, pp. 6229-6238, Aug. 2018.

[76] European Network of Transmission System Operators for Electricity, "Network code for requirements for grid connection applicable to all generators," Tech. Rep, Apr. 2016.

[77] E. Troester, "New German grid codes for connecting PV systems to the medium voltage power grid," in *Proc. 2nd Int. Workshop Concentrating Photovoltaic Power Plants: Opt., Design, Prod., Grid Connection*, 2009.

[78] Energinet.dk, "Technical regulation 3.2.2 for PV power plants with a power output above 11 kW," Tech. Rep. Doc. 14/17997-39, 2016.

[79] O. Erdinc and M. Uzunoglu, "Optimum design of hybrid renewable energy systems: Overview of different approaches," *Renew. Sustain. Energy Rev*., vol. 16, pp. 1412–1425, Apr. 2012.

[80] *IEEE Draft Guide for Array and Battery Sizing in Stand-Alone Photovoltaic (PV) Systems*, IEEE P1562/D1.1, Mar. 2018.

[81] L. Xu, X. Ruan, C. Mao, B. Zhang, and Y. Luo, "An improved optimal sizing method for wind-solar-battery hybrid power system," *IEEE Trans. Sustain. Energy*, vol. 4, no. 3, pp. 774–785, Jul. 2013.

[82] I. Pawel, "The cost of storage—How to calculate the levelized cost of stored energy (LCOE) and applications to renewable energy generation," *Energy Procedia*, vol. 46, pp. 68–77, 2014.

[83] Y. Yu, G. Konstantinou, B. Hredzak, and V. G. Agelidis, "Power balance of cascaded H-bridge multilevel converters for large-scale photovoltaic integration," *IEEE Trans. Power Electron*., vol. 31, no. 1, pp. 292-303, Jan. 2016.

[84] M. Wang, X. Zhang, T. Zhao, F. Zhuang, F. Wang, N. Qian, and S. Yang, "Module power balance control strategy for three-phase cascaded H-bridge PV inverter under unbalanced grid voltage condition," *IEEE J. Emerg. Sel. Top. Power Electron*., vol. 9, no. 5, pp. 5657-5671, Oct. 2021.

[85] S. Rivera, B. Wu, S. Kouro, H. Wang, and D. Zhang, "Cascaded H-bridge multilevel converter topology and three-phase balance control for large scale photovoltaic systems," in *Proc. IEEE PEDG*, 2012, pp. 690-697.

[86] Y. -C. Su and P. -T. Cheng, "Development of a hybrid cascaded converter based STATCOM with reduced switching losses and improved fault ride through capability," *IEEE Trans. Ind. Appl*., vol. 57, no. 3, pp. 3087-3096, May-Jun. 2021.

[87] R. R. Karasani, V. B. Borghate, P. M. Meshram, H. M. Suryawanshi, and S. Sabyasachi, "A three-phase hybrid cascaded modular multilevel inverter for renewable energy environment," *IEEE Trans. Power Electron*., vol. 32, no. 2, pp. 1070-1087, Feb. 2017.

[88] A. Bani-Ahmad and C. A. Ooi, "Optimal cell utilization for improved power rating and reliability in a grid-scale three-phase battery energy storage system using hybrid modular multilevel converter topology without redundant cells," *IEEE J. Emerg. Sel. Top. Power Electron*., vol. 9, no. 2, pp. 1780-1794, Apr. 2021.

[89] D. Holmes and T. Lipo, *Pulse Width Modulation for Power Converters: Principles and Practice*. New York, NY, USA: Wiley, 2003.

[90] E. Uz-Logoglu, O. Salor, and M. Ermis, "Online characterization of interharmonics and harmonics of AC electric arc furnaces by multiple synchronous reference frame analysis," *IEEE Trans. Ind. Appl*., vol. 52, no. 3, pp. 2673-2683, May-Jun. 2016.

[91] S. Wu and Z. Liu, "Low-frequency stability analysis of vehicle-grid system with active power filter based on dq-frame impedance," *IEEE Trans. Power Electron*., vol. 36, no. 8, pp. 9027-9040, Aug. 2021.

[92] E. Uz-Logoglu, O. Salor, and M. Ermis, "Real-time detection of interharmonics and harmonics of AC electric arc furnaces on GPU framework," *IEEE Trans. Ind. Appl*., vol. 55, no. 6, pp. 6613-6623, Nov.-Dec. 2019.

[93] S. Das, I. U. Nutkani, and C. Teixeira, "Decentralised master slave control for series cascaded islanded AC microgrid," *IEEE Trans. Ind. Electron*., vol. 69, no. 6, pp. 5942-5951, Jun. 2022.

[94] J. He, Y. Liu, and Y. Wang, "Cascaded droop and inverse droop regulation for two-layer coordinated power flow control in series-connected power cells," *IEEE Trans. Ind. Electron*., vol. 68, no. 8, pp. 6939-6951, Aug. 2021.

[95] J. He, X. Liu, C. Mu, and C. Wang, "Hierarchical control of series-connected string converter-based islanded electrical power system," *IEEE Trans. Power Electron*., vol. 35, no. 1, pp. 359-372, Jan. 2020.

[96] H. Han, Y. Zhu, G. Shi, M. Su, and Y. Sun, "A local-distributed and global-decentralized SoC balancing method for hybrid series-parallel energy storage system," *IEEE Syst. J*., DOI: 10.1109/JSYST.2021.3068167.

[97] Z. Li, Z. Cheng, J. Si, S. Zhang, L. Dong, S. Li, and Y. Gao, "Adaptive power point tracking control of PV system for primary frequency regulation of ac microgrid with high PV integration," *IEEE Trans. Power Syst*., vol. 36, no. 4, pp. 3129-3141, Jul. 2021.

[98] A. Sangwongwanich, Y. Yang, and F. Blaabjerg, "A sensorless power reserve control strategy for two-stage grid-connected PV systems," *IEEE Trans. Power Electron*., vol. 32, no. 11, pp. 8559-8569, Nov. 2017.

[99] X. Li, H. Wen, Y. Zhu, L. Jiang, Y. Hu and W. Xiao, "A novel sensorless photovoltaic power reserve control with simple real-time MPP estimation," *IEEE Trans. Power Electron.*, vol. 34, no. 8, pp. 7521-7531, Aug. 2019.

[100] E. I. Batzelis, S. A. Papathanassiou and B. C. Pal, "PV system control to provide active power reserves under partial shading conditions," *IEEE Trans. Power Electron.*, vol. 33, no. 11, pp. 9163-9175, Nov. 2018.

[101] Y. Ko, M. Andresen, G. Buticchi, and M. Liserre, "Power routing for cascaded H-bridge converters," *IEEE Trans. Power Electron.*, vol. 32, no. 12, pp. 9435-9446, Dec. 2017.

[102] X. Zhang, Y. Hu, W. Mao, T. Zhao, M. Wang, F. Liu, and R. Cao, "A grid-supporting strategy for cascaded H-bridge PV converter using VSG algorithm with modular active power reserve," *IEEE Trans. Ind. Electron*., vol. 68, no. 1, pp. 186-197, Jan. 2021.

[103] L. Maharjan, S. Inoue, H. Akagi, and J. Asakura, "State-of-charge (SOC)-balancing control of a battery energy storage system based on a cascade PWM converter," *IEEE Trans. Power Electron*., vol. 24, no. 6, pp. 1628-1636, Jun. 2009.

ISSN (online): 2446-1636
ISBN (online): 978-87-7573-935-6

AALBORG UNIVERSITY PRESS